INCLUSIVE DISTRIBUTIONS OF DIFFRACTIVELY PRODUCED NEUTRAL KAONS, LAMBDAS, AND ANTILAMBDAS, AND UPPER LIMITS ON Λ_c^+ PRODUCTION IN HIGH ENERGY γ p INTERACTIONS

by

Sampa Bhadra

B.S., University of Calcutta, 1975

M.S., University of Colorado, 1980

A thesis submitted to the
Faculty of the Graduate School of the
University of Colorado in partial fulfillment
of the requirements for the degree of
Doctor of Philosophy
Department of Physics
1984

AAC8054

This thesis for the Doctor of Philosophy degree by

Sampa Bhadra

has been approved for the

Department of

Physics

by

Uriel Nauenberg

Uriel Nauenberg

Thomas A. DeGrand

Date Dec 9, 1984

Bhadra, Sampa (Ph.D., Physics)

Inclusive Distributions of Diffractively Produced Neutral Kaons, Lambdas and Antilambdas, and Upper Limits on Λ_c^+ Production in High Energy γ p Interactions

Thesis supervised by Professor Uriel Nauenberg

Abstract

We have used a large acceptance spectrometer in a tagged photon beam to study the interactions of real photons with protons in a hydrogen target. In particular, this thesis presents distributions of neutral kaons, lambdas, and antilambdas from diffractive dissociation where the kinematic regions of the target and projectile fragments are clearly distinguished by using events with clean recoiling protons.

If factorisation is valid, then one can separate the γ p -> X p interaction into p -> p + P , and γ + P -> X, where P is the exchange process responsible for the interaction of the photon and proton. If we now investigate the regions of large positive and negative Feynman X_f in the centre-of-mass of X, we will have information on both the photon and P fragmentation, respectively. Comparing the X_f distribution to predictions from various counting rule models allows us to investigate the constituents of P.

A relevant parameter for such an interaction is the energy scale set by the mass of X (M_X). We demonstrate that the yield of the neutral strange particles per hadronic event depends only on M_X and not on the incident energy of the photon. When the M_X distribution from this experiment is compared to the centre-of-mass dependence of neutral strange particle production in e^+e^- experiments, a remarkable similarity is observed. We have also shown that the average transverse momentum increases with the energy M_X, as has been observed in other experiments.

This data extends the neutral strange particle production rate measurements to higher overall centre-of-mass energies than previous photoproduction experiments. Comparison to pion-induced reactions supports the hypothesis that the photon behaves primarily as a hadron.

Finally, we have set upper limits on the Λ_c^+ cross section times the branching ratio for decay modes leading to neutral strange particles for a diffractive dissociation process.

Acknowledgments

I take this opportunity to thank the entire collaboration who made this experiment possible. They are the following:

D. Bartlett, S. Bhadra, A Duncan, J. Elliott, U. Nauenberg.

(University of Colorado, Boulder, U.S.A.)

P. Estabrooks, J. Pinfiold

(Carleton University, Ottowa, Canada)

M. Losty

(National Research Council of Canada)

G. Luste, J. F. Martin, G. Hartner, D. Gingrich, C. Zorn, J. Spalding, K. Shahbazian, J. Stacey, D. Blodgett, B. Sheperd, S. Bracker, R. Kumar.

(University of Toronto, Toronto, Canada)

M. Witherell, R. Morrison, D. Summers, U. Joshi, S. Yellin, B. Denby, A. Lu, V. Bharadwaj, D. Caldwell, A. Eisner, R. Kennett.

(University of California, Santa Barbara, U.S.A.)

G. Kalbfleisch, M. Robertson

(University of Oklahoma, Norman, U.S.A.)

L. Chen, M. Streetman, B. Schmidke, M. Sokoloff, J. Bronstein, C. Daum, T. Nash, D. Bintinger, P. Mantsch, K. Sliwa, J. Appel, J. Biel, S. Willis, K. Stanfield.

(Fermi National Accelerator Laboratory, U.S.A.)

Though many have contributed towards the completion of this thesis, I would like to personally acknowledge those who have provided a little more input than others. I take this opportunity to give thanks:

to my advisor Uriel Nauenberg for his patience, support and encouragement throughout these years. I thank him for his ability to listen, his personal concern and for allowing me to develop my independence. I have benefited greatly under his guidance.

to Jim Randa, Jim Elliott, Alan Duncan - it is impossible to thank them enough for their invaluable assistance over the long and seemingly endless years, Many thanks for their friendship, stimulating discussions, advice, care, and moral support. They were a pleasure to work with, and without them, this task would have been much harder.

to Bill Schmidke and Mike Sokoloff, for invaluable discussions, friendship and strong moral support throughout.

to David Bintinger, Penny Estabrooks, Jeff Spalding, Mike Witherell, Gerd Hartner and Kris Sliwa for many useful discussions and personal concern.

to John Martin, David Bintinger, Tom Nash, Penny Estabrooks and Steve Bracker for their immense efforts in starting up the experiment, and their constant vigilance through many a gloomy night.

to Tom DeGrand, who provided advice, answers and support when I invaded his space at odd hours.

to John Cumalat, whose enthusiasm for physics was fresh and stimulating.

to Kathy Oliver, Linda Frueh, Margaret Kneebone and Evelyn Jones, for their moral support and friendship, with a special thanks to Kathy and Margaret for help in editing the thesis.

to my friends in the department (such as Paul, Ray, Steve(s), Jean, Sharon) who made life bearable during the interminable last push.

to Ma Bell, who allowed me to reach out and touch someone.

Last, but certainly not least, to John Martin, whose lack of patience finally induced me to finish. For bearing with my many moods and tolerating my (occasional) insanity, on him I bestow sainthood.

I dedicate this thesis to my parents. Ultimately, it is they who have made this contribution possible.

CONTENTS

CHAPTER

FIGURES

FIGURE

CHAPTER I

INTRODUCTION AND THEORY

For many years physicists have used collision methods to understand the nature of matter. Increasing the force of collision allows us to probe deeper into the internal structure of the target. Rutherford's experiment of bombarding α particles on gold foil led to the discovery that the atom had substructure. Since Rutherford's time we have developed the capability of increasing the energy of the projectile to much higher levels. Collision of electrons on protons showed the unexpected result of even smaller structure within protons. This observation gave rise to a long progression of theories, models, and experiments based on the hypothesis that the observed hadronic spectra and their kinematic distributions can be explained if the hadrons are postulated to be composed of subcomponents called quarks and gluons. The theory of the strong interactions obeyed by the quarks and gluons is known as Quantum Chromodynamics (QCD).

Photons have also featured prominently in experiments as physicists first tried to resolve the dual (wave vs. corpuscular) nature of photons. Since then photons have been used in high energy experiments both as a probe of the target as well as a candidate for the study of its structure. This thesis presents inclusive distributions of neutral strange particles produced as the fragments of photons interacting with protons in a hydrogen target. Let us examine why we have chosen to conduct a photoproduction experiment.

One may use the photon to create or probe matter, as is done in e^+e^- and deep-inelastic muon scattering experiments, where the photon may be highly virtual (i.e. carrying a four momentum $|Q^2| >> 0$) and the coupling to the quark-antiquark pair is point-like. The photon is then acting as if structureless, and the coupling to the quark pair is calculable. This is the case when the interaction is "hard", i.e., there is a large Q^2 transfer occurring between the initial particles. This is analogous to saying that the transverse momentum P_t of the observed particles with respect to the beam direction is large. The observables of these interactions, such as the total cross section, fragmentation region distribution etc. can be calculated by perturbative QCD. However, in order to understand the structure of the photons themselves, we have to deal with real photons. The process in this instance is no longer point-like, because the photon now has a form or internal structure, just as the target. A large beam energy does not guarantee a large momentum transfer, and there is also a "soft" component. Our experiment is not in the region of high P_t (average $P_t \approx 400$ MeV/c), and the process is not calculable by perturbative methods. Recent years have seen the birth of many models trying to predict the behaviour of fragments (of both the projectile and the target) in the "soft" low P_t region. Comparison of our data with the models is a step towards testing the validity of the model(s).

The similarity of the behaviour of the total cross-section for photo-induced and hadro-induced reactions[1] indicates that the photon has characteristic behaviour in common with hadrons - more specifically, a vector meson which has the same quantum numbers as the photon.

At high energies the elastic scattering of hadrons is diffractive in nature, and characterised by an exponential t dependence (for small t) where t is the invariant four momentum transfer between the beam and the target. The photoproduction of ρ^0 from $\gamma\ p \rightarrow \rho^0\ p$ interaction also shows this behaviour. It has been observed that the γp cross section $\sigma(\gamma p)$ is similar to the sum of $\sigma(\pi^+ p)$ and $\sigma(\pi^- p)$, scaled down to take into account the electromagnetic fine structure constant ($\alpha \approx 1/137$) that occurs at any photon vertex. What is more encouraging for the argument that the photon is hadronlike in its behaviour is that the curves $d\sigma/dt$ for the t dependence can be also be fit to a form expressed as the sum of the $d\sigma/dt$ for $\pi^+ p$ and $\pi^- p$ interactions, again scaled properly. Since the slope of the $d\sigma/dt$ exponential dependence measures the projectile's effective size, this would indicate that the diffraction radius for γp and πp interactions are approximately the same.

The model of Vector Meson Dominance, constructed to explain soft photoinduced scattering processes, incorporates this observation,[2] asserting that the photon couples to a vector meson (ρ,ω,ϕ..) which has the quantum numbers $J^{PC} = 1^{--}$. This vector meson couples to the nucleon to form the observed secondaries. The strength of the coupling of the real photon to the vector mesons can be obtained from the measured coupling (= F_1) of the virtual photons to the vector mesons in e^+e^- experiments,[3] and a supression factor (= F_2) for transition to a real photon. The contribution to the cross section for vector mesons decreases as the vector meson mass increases because

a.) F_1 is inversely proportional to the mass of the vector meson and,

b.) the supression factor F_2 increases with the mass.

This concept of the hadronic behaviour of the photon is certainly not obvious intuitively, and hence it is intriguing. For example, one may ask if this behaviour holds true even for very high energies. What are the processes that occur between the incoming photon and the final hadronic states? What is the mechanism of the coupling of the photon to the target particle? In this thesis we try to address the question of strange meson and baryon production from the photon fragmentation process.

The discovery of the charmed quark (from ψ production) leads naturally to the enquiry into the charm content of the photon. The ψ particle, which is composed of a charm-anticharm pair of quarks, is also a vector meson with the quantum numbers of the photon, and should couple to the photon as the ρ,ω etc. This does indeed occur and various experiments have established the magnitude of this coupling. One has only to look at the fraction of the total cross section of charmed particles from photons, and compare this to hadroproduction experiments, to realise that the photon cannot be acting as merely as a ρ or ω or ϕ meson. We observe that

$$\frac{\sigma\ (\gamma p \to \text{charm}\ )}{\sigma\ (\gamma p \to \text{hadron})} \approx 1\% \quad \text{vs.} \quad \frac{\sigma(\pi p \to \text{charm})}{\sigma(\pi p \to \text{hadron})} \approx .1\%$$

Thus photoproduction of charmed states seems to be enhanced compared to hadroproduction. On the other hand, photoproduction of charmed states via a virtual photon (as in e^+e^- experiments) and via a real photon have important similarities such as the good signal to noise ratio in both cases.

Let us look at an inelastic process A+B -> D+E (fig 1.1), because at high energies the inelastic processes dominate. High energy hadron production is characterised by the following properties:[4]

1.) The average multiplicity of the secondary particles increases as the log(s) where s is the center-of-mass energy.

2.) The transverse component of the momentum (P_t) is limited relative to the incident beam direction i.e. $< P_t >$ is of the order 400 MeV/c. Hence, low P_t production is predominant.

3.) The longitudinal component of the momentum $P_{\parallel}$ can be expressed as $P_{\parallel}/P_{max} \equiv X_f$ (Feynman X_f). The distribution of particles in X_f is seen to be independent of the collision energy (scaling). This distribution is roughly exponential, showing that low $P_{\parallel}$ processes dominate.

4.) Small X_f corresponds to the region C (the central region) where the production of secondary hadrons is found to be independent of the nature of the incoming beam (A) or the target (B). Hence, the characteristics of these secondaries are common for all processes.

5.) Regions D and E include the diffractive component[5], and since diffraction is a coherent process, it is more directly involved with the actual structure of the projectile or target.

A separation in X_f between D and E provides us with a kinematic region where we may clearly distinguish between the fragments of the photon and the proton. In this experiment we are interested in looking only at the fragments of the photon, and the exchange particle " P ", via the process shown in fig. 1.2 . This is the process of diffractive dissociation where the particle A (the proton) remains intact or in an excited state, and the particle B (the photon) fragments after interacting with the mediator "P" of the collision. The state X has the additive quantum numbers of the photon and the state P has the quantum numbers of the vacuum, as no quantum numbers have been exchanged. We look at the process of diffractive dissociation[5] by studying events that clearly show an unfragmented recoiling proton.

Most models for the photon interaction require the photon to appear as a quark-antiquark pair via some model dependent mechanism, after which they materialise into the observed hadronic spectra. There are several candidate models to construct the mechanism of the "dressing", i.e. hadronising, process of the quark-antiquark pair from the photon in the "soft" regime.

Recent studies[6] have shown many common aspects of both low P_t and high P_t events, namely in the shape of the longitudinal and transverse momentum, as well as in the multiplicity of the events. This is perhaps not a mere coincidence. The pions produced in soft hadronic experiments in the region of the fragmentation of the nucleon seem to reflect the valence quark distribution, and this same behaviour is seen in deep inelastic lepton and e^+e^- experiments. This leads one to hope that perhaps the parton structure that is responsible for the hard processes may be responsible for the interactions in soft processes also. We discuss briefly several models[7-14] for the hadronization of the quarks, and where applicable, will compare the predictions of the model with our data.

We shall be studying the basic process of the interaction $\gamma\ p \to X\ p$ in two centre-of-mass frames. One is the overall centre-of-mass of the photon-proton system, and the other is the subprocess photon-P system, where we have factorised[11] the basic interaction into $p \to p + P$, and $P + \gamma \to X$. Here X is called the forward mass. The forward centre-of-mass is obtained by boosting the photon to the centre-of-mass of the system X. The Feynman X_f of a particle in the overall and forward centre-of-mass systems shall be known as X_{of}, and X_{ff} respectively. In fig. 1.3 and fig. 1.4 we show pictorially the definitions of the overall and forward centre-of-mass frames respectively.

In the region of large positive X_f, we expect to observe only the fragments of the photon. In the overall center-of-mass, the region of negative X_{of} (less than -.05) cannot be seen by our detector for reasons to be described below. The events of X_{of} greater than -.05 are redistributed into the forward X_{ff}. Again, the region of large + X_{ff} reflects the photon fragmentation - except now we also have the region of the P fragmentation in the negative X_{ff} region. Hence, we have a tool to study the nature of the exchange mechanism.

The production of a meson (for example) from a valence quark of the photon may proceed via different processes depending on the model. We give several examples to give a flavour of the existing models.

1.) We show in fig. 1.5 the process of quark fragmentation where the the quark "fragments" into the observed meson by gluon bremmstrahlung, and the gluon then forms a non-valence quark-antiquark pair. It can be seen from the momentum labels of the diagram that the momentum of the observed hadron is always less than the momentum of the incoming quark. At high X_f of the meson, this process is supressed as the probability for the meson to be carrying a large fraction of the quark momentum is low. This fragmentation model is believed to be the mechanism for hadronization in e^+e^- and deep inelastic scattering experiments.

2.) However, it has been argued by Das and Hwa[7] that the above fragmentation process contributes to only ≈ 1% of the single meson production in the low P_t, high X_f region. This has led to the recombination model, and in fig. 1.6 we give an example of meson production.

Here it is assumed that the fast hadron production is initiated by a fast quark, which is most probably a valence quark of the incoming photon. The recombination at high X_f occurs only with an antiquark (from the sea or one excited by a gluon) that is moving in the same direction as the incoming quark. Hence the momentum of the meson is higher than the initial quark, and the meson production amplitude is sensitive to the probability of finding a quark-antiquark pair with the right quantum numbers. Obviously this process cannot be found in e^+e^- experiments where the beams are formed initially as quarks and antiquarks moving in opposite directions.

The lowest order Feynman diagram of the fragmentation model has been shown as it will be used in the discussion of the parametrization of the observed X_f spectra.

Several models have been constructed to test the mechanism of the interaction of the photon with the proton. The model of one gluon exchange, as shown in fig. 1.7a, has been used in an attempt to explain the production of hadrons, and charmed particles in particular. However, it has been argued[5] that the one gluon exchange will not give rise to a large X_f or kinematic gap in particle production between the photon and proton fragmentation regions. The two gluon exchange process[12-13], shown in fig 1.7b, is calculable perturbatively, but its contribution in soft processes is very small. The result of the collision of the quark-antiquark pair with the gluons are two quark jets which should be clearly distinguishable at high energies.

Gunion[6] has attempted to model low P_t interactions by arguing that, even though such processes are not well understood, the underlying principle is the interaction between quarks and gluons. The modelling of the low P_t behaviour is constrained by known results in high P_t processes. As an extension of this, we consider the model of DeGrand and Randa[11] for the relevant diffractive dissociation process.

According to them, γ p interactions may be described by a factorising scheme, where the process is initiated and mediated primarily through multiple gluon exchange (fig 1.7c). The amplitude of the process γ p -> p X contains a term for the amplitude of the process γ P -> X. This γ P amplitude is dependent on the momentum transfer in the γ p process. However, this t dependence is weak, and the factorising can be taken to be exact.

Attempts have been made to parameterise the X_f dependence of the cross section to available photon, hadron, lepton induced and e^+e^- data in order to understand the dynamics of the partons inside any particle. The behaviour of the differential cross section $d\sigma/dX_f$ is proportional to $(1-X_f)^D/X_f$, where X_f is the fractional momentum carried by the leading quark, and the power D is determined from dimensional quark counting. Counting rules are model dependent; in the model of Gunion the fast fragments from the gluon exchange mechanism are postulated from QCD diagrams where the quark-antiquark pair is produced as if point-like.

The counting rules are obtained from the expression

$X_f \, d\sigma/dX_f \propto (1-X_f)^D$

where $D = 2\, n_b + n_p - 1$,

n_b = the number of bound state spectators ,

n_p = the number of perturbative i.e. point-like spectators in the emmision.

Taking the example of the prediction for the leading contribution to the cross section, we have the Feynman diagram for the production of a meson in fig. 1.8a.

In this case

$$D = 0 + 2 - 1 = 1 , \qquad n_b=0,\ n_p=2. \qquad (1.1)$$

Hence $X_f \, d\sigma/dX_f \propto (1-X_f)^1$

Similarly, from fig. 1.8b for baryon production at the high X_f region in the overall center of mass, we have

$$D = 0 + 3 - 1 = 2 , \qquad n_b=0,\ n_p=3. \qquad (1.2)$$

Hence $X_f \, d\sigma/dX_f \propto (1-X_f)^2$

Now we come to the interesting γ P subprocess. If the region of X_f -> +1 corresponds to photon fragmentation, the results of eqn. (1.1) and eqn. (1.2) for the meson and baryon production should still be valid. But now we are in a position to inspect the P components in the negative X_{ff} region. If P has a two gluon component, then, using the counting rules described previously, the diagrams in figs. 1. 9a and fig 1. 9b may be responsible for its hadronization into a K_s^0 and Λ, respectively, in the high negative X_{ff} region.

We obtain $n_b = 0$ and $n_p = 2$ for the meson production via two gluon exchange, and hence D =1. For baryons, $n_b = 0$ and $n_p = 3$ giving D = 2.

A three gluon component, on the other hand, would give rise to the diagrams in fig 1.10a and fig 1.10b, again for a K_s^0 and Λ respectively. We obtain $n_b = 1$ and $n_p = 2$ for the meson case, whence D = 3. For the case of the baryon, $n_b = 0$ and $n_p = 3$ giving D = 2.

It should be noted that the predictions for the counting rules have been made ignoring spin correlations at the vertices. However, the model has been fairly successful at comparing the predictions with various hadronic experiments[6]. In this thesis we we have obtained values of the dimension D at large X_f for comparison with theoretical predictions.

We have noted the strong possibility of a similarity between e^+e^- interactions and the factorised γ P interaction. We investigate this by looking at the yield per hadronic event of the neutral kaons, lambdas, and antilambdas in the comparable frames. We also compare the yield to other pion-induced and photo-induced interactions in terms of the available energy E_{avail}, which is defined as being the overall center-of-mass energy $\sqrt{s}$ minus the mass of the incoming particles. For our experiment this would be $\sqrt{s} - m_p$. This variable is independent of the nature of the projectile or the target, and hence is convenient for comparison with other hadron experiments.

Finally, we have also searched for a signal of the lowest lying charmed baryon Λ_c^+ decaying into the $\overline{K^0}p$ and $\Lambda\pi^+$ modes. However, as we have been unsuccesful in obtaining a significant signal, we have set upper limits (to 90% confidence level) on the production cross-section in γ p diffractive dissociation.

CHAPTER II

INTRODUCTION TO THE EXPERIMENT

The tagged photon experiment (proposal E-516) was carried out at the Fermi National Accelerator Laboratory. The beam line of the accelerator has been presented in great detail in previous theses[16] from this experiment. An overview is given below.

750 KeV protons from a Cockcroft - Walton accelerator are injected into a linear accelerator. These travel down a straight vaccuum tube through a chain of radio frequency cavities which provide oscillating electric fields, the relative phases of which are arranged to allow the particles to accelerate continuously to 200 MeV. These protons are then injected into the 8 GeV synchrotron from which they are injected into the main ring for the final acceleration to 400 GeV.

The beam extracted from the main ring is split into the three experimental areas, as shown in the fig. 2.1 . The proton area beam is further subdivided into the P-East, P-Centre, and P-West areas. The tagged photon experiment has been conducted in the P-East area.

400 GeV protons at the rate of 5 x 10^{12} per machine pulse are directed onto a 30 centimetres long Beryllium target, producing various neutral and charged particles, such as charged and neutral pions, gammas, neutrons, K_L, etc. The charged particles are swept out by magnets. The beam then consists primarily of neutral kaons, neutrons, and pions. The neutral pions (π^0) decay immediately into a pair of photons, as this is an electromagnetic interaction and the life time $\approx 10^{-16}$ sec. These photons then convert to an e^+e^- pair in .32 centimetres of lead.

A system of dipole deflection magnets and quadrupole magnets (whose function is to focus in the vertical and horizontal direction in sequence) selects electrons of the desired momentum range with an acceptance of ± 2%. The electron beam is tuned to 170 GeV and is a steeply falling function of energy, reflecting the π^0 production spectrum from the Beryllium target. The flux at this energy is $\approx 7 \times 10^7$ electrons per pulse, with negligible contamination. Fig. 2.2 shows the approximate electron yield as a function of incident electron energy. This electron beam passes through a .28 cm. copper radiator producing bremstrahlung photons along the beam direction. The electrons are bent into the tagging system for energy measurement, from which the photon(s) is (are) tagged i.e. the photon energy is known. In fig. 2.3 we show the spectrum of the interacting photons. Non-interacting electrons are swept into the electron dump (see fig. 2.4).

The primary object of the experiment is to study the interaction of the bremsstrahlung photons on a liquid hydrogen target.

THE TAGGING SYSTEM

The tagging system for the energy measurement of the deflected electron is an ensemble of 13 lead glass blocks and 13 scintillator strip hodoscopes. Lead block L1 detects electrons that either do not interact or radiate less than 45 % of their energy. The lead blocks L2 - L12 are arranged in vertical strips. L13 is perpendicular to the beam direction to gain adeqate acceptance of the widely separated low energy electrons. A 1/2 inch strip of lead is used to initiate showers in order to insure shower maximum to occur within the block (and hence give better energy resolution). The lead glass blocks are damaged by constant irradiation and are cleared weekly with an ultraviolet lamp. The hodoscopes, in coincidence with the lead glass blocks, provide a fast beam signal for the experimental trigger i.e., the photon is tagged.

DETECTOR LAYOUT AND DESCRIPTION

The aim of the experiment is to extract diffractive events enriched with charm.

A layout of the spectrometer is shown in fig. 2.5 . The hydrogen target is enclosed by the recoil detector. The latter is used for identifying a recoil proton in order to flag a diffractive event of the type γ p -> p X. It is aided in its selection by a trigger processor. An electromagnetic shower counter (the C-counter) identifies multiple bremsstrahlung events and events where the photons do not interact. Four drift chamber assemblies (D1, D2, D3, D4) are employed for position determination of charged tracks. The momenta of charged tracks are determined by their bend in a magnetic field provided by two magnets M1 and M2, each with a mean transverse momentum (P_t) impulse of 150 MeV/c. M1 is between the target and D2, with D1 actually inside the aperture of M1. M2 is placed between D2 and D3. Particle identification for pions, kaons and protons is done with two Cherenkov counters, C1 and C2. A segmented liquid ionization counter (SLIC) and an "outrigger" provide electromagnetic particle detection. The latter is used for high P_t photons from π^0 decays, which may not reach the downstream SLIC. The hadrometer detects neutral hadrons. A steel wall follows to stop particles except muons. These muons are detected by a final array of scintillation hodoscopes.

We now describe the apparatus in detail.

THE TARGET

The target is liquid hydrogen contained in a mylar vessel of length 150 cm. and 1 inch radius. A mylar and foam vacuum system encloses this for insulation and safety. The vacuum system, the pressure in the target, and the hydrogen level are monitored from the counting room. The X and Y distributions of the primary vertex in the target reflect the beam envelope, as shown in figs. 2.6 and 2.7 respectively. The mean of these distributions are .05 and -.82 cms. respectively. The Z position of the primary vertex is shown in fig. 2.8 . The enhancement towards the downstream end (higher Z) is partly due to secondary interactions, and partly from trigger biases. The length of the target is chosen to be a compromise between large hadronic event rate and low secondary interactions.

THE RECOIL DETECTOR

Due to the nature of this experiment, namely the study of charm photoproduction, we would like to select high mass diffractive events. The recoil detector, in conjunction with the trigger processor, performs this task at a rate that is compatible with Camac read-in time.

A radial profile of the detector is shown in fig. 2.9 . Recoil protons in the range $-.06 < t(\mathrm{GeV}/c)^2 < -1.4$ are accepted in the detector where t is defined by

$$t = (P_i - P_f)^2 = 2\, M_p{}^2 - 2\, E_f\, M_p \qquad (2.1)$$

where $P_i = (E_i,\overline{P}_i)$ = Four momentum of the target proton

$P_f = (E_f,\overline{P}_f)$ = Four momentum of the recoiling proton

M_p = Mass of the proton

The recoil detector consists of three cylindrical proportional wire chambers and four scintillator layers surrounding the liquid hydrogen target. Each proportional wire chamber has a central anode (wires stretched longitudinally parallel to the beam) placed in between an inner aluminized mylar cathode and an outer cathode of copper wire hoops. The calorimeter portion of the recoil detector consists of 15 sectors or wedges, with a gap at the bottom for the support system (see fig. 2.9). The two inner layers of plastic scintillator are relatively thin to minimize nuclear interactions of the proton. The outer two layers of liquid scintillator are thick to help pion/proton separation from dE/dX information to large values of t.

To obtain the forward mass the following formula is used:

$$\begin{aligned} M_x{}^2 &= (P_\gamma + P_i - P_f)^2 \\ &= 2\ m_p{}^2 + 2\ E_\gamma\ (\ m_p - E_f + \overline{P}_f \cos\Theta\ ) - 2\ m_p\ E_f \end{aligned} \tag{2.2}$$

where E_γ = the incident photon energy and

Θ = the recoil angle with respect to the incident photon.

The recoil angle is obtained from the PWC readout cathodes. This is then matched to the proper sector where energy has been deposited in the scintillator layers. End to-end-timing information at the A layer is provided by time of arrival of the signal at the phototubes placed at the two ends of the layer. The Z position is obtained from the timing difference (end-to-end timing), and is used in the matching process for comparison with the projected Z position from tracks found in the chambers. The energy of the recoiling particle is determined from the energy deposited in the scintillator layers. Comparing this to the Bethe-Bloch predictions for energy loss of a particle in traversing a medium one obtains the probability that the track is a proton or a pion. If the particle stops in the A (first) layer this energy information is not enough to indentify the particle and must be supplemented by time-of-flight information (TOF).

From the above information we can calculate the forward mass. This is done on-line by the trigger processor, the details of which will be given in Chapter III.

CALIBRATION FOR THE RECOIL DETECTOR

The recoil detector is calibrated[17] using data events with a single PWC track and a single active scintillator. The two parameters for the end-to-end timing are obtained from a fit to straight line using the Z position of the track in the cathode. The time-of-flight calibration for the A layer is done from the recoil trajectory and the energy measurement (corrected for energy loss due to ionization in the path) and compared to the beam tag as the reference. The trigger processor expects the ADC's to have the same gains in all the 15 sectors; hence they are adjusted and calibrated periodically to maintain the expected value. The calibration is done from comparisons of energy loss measured versus energy loss predicted from the Bethe - Bloch equation. An adjustment is made for protons that stop in the A layer. A laser signal on each phototube is used to maintain the voltage required in the tube for the proper gain. This is then compared to the gain from the off-line reconstruction for absolute gain evaluation.

THE DRIFT CHAMBERS

Drift chambers are used to record the passage of charged particles and measure their position with respect to a set of parallel anode wires. The chamber is filled with a gas which ionizes when the charged particle passes through it. The ionization electrons drift towards the anode in a relatively uniform field provided by strategically placed cathode wires. In the high field gradient near the thin anode wire, an avalanche occurs, and the resultant amplification of the signal depends on the composition of the gas and the voltage difference between the anode and cathode. Drift chamber measurements allow the reconstruction of particle trajectories, and if two sets of chambers are placed on both sides of a magnet, we can evaluate momenta from a knowledge of the field strength. Reconstruction takes place in a plane perpendicular to the wire direction. In order to resolve the " left - right ambiguity" (it is not known from which side of the wire the signal arrives), and ensure complete three dimensional reconstruction of multitrack events, three non parellel sets of wires (or views) are required. In this experiment the arrangement chosen (see fig. 2.10) is as follows :

1. D1

This consists of two assemblies. The U and the V view are at $+20.5^0$ and -20.5^0 with respect to the set of vertical wires of the X view. The fourth view (X') consists of a set of 36 wires in the central region parallel to the X view but offset by half a wire spacing in X. It aids in tracking complicated central tracks in D1. The cell size for this chamber is .16 inch for the U,V views, and .18 inch for the X, X' views. The resolution of the chamber is approximately 330 microns.

2. D2

This module, upstream of the second magnet, contains three (UXV) assemblies with the field wires stretched vertically. The cell transverse dimension is .33 inch for the U and V planes and .37 inch for the X plane. The resolution here is approximately 320 microns.

3. D3

This is identical in concept to D2, except the cell size is .56 inch in the X view, and .62 inch for the U,V views. The resolution here is roughly 300 microns.

4. D4

This is a single module X U V assembly with the field shaping taking place by a sheet of aluminium (cathode) held at ground and the anode held at high voltage. The resolution is about 700 microns, and the wire spacing is 1.1 inches for the X view, and 1.2 inches for the U,V views.

All four chambers are gas tight and contain a mixture of 50% argon and 50% ethane at .1 inch of water pressure. The signals on the anode wires are amplified and discriminated, and the resulting signal acts as the START to a channel of Le Croy 2270 TDC's (time-to-digital converter). The STOP is provided by the TAG.H trigger (a TAG with a hadronic interaction - this is described in CHAPTER III). This digitised time is part of the event record.

CALIBRATION OF THE DRIFT CHAMBERS

Drift chamber calibration involves not only chamber alignment but also techniques to ensure that the TDC information is formatted correctly. Calibration for position is provided, with the magnets turned off, by the copious flux of muons through the Tagged Photon facility. The relative timing differences between different wires in a particular plane, and the overall normalisation for different planes will be dealt with in the reconstruction section of Chapter IV.

THE CHERENKOV COUNTERS

When a particle traverses a medium faster than the velocity of light in that medium then Cherenkov light is emitted at angle Θ_C with respect to the line of flight of the particle. From fig. 2.11 we obtain,

$$\cos\Theta_c = 1/\beta n \qquad (2.1)$$

where n = refractive index of the medium

Θ = the angle of light emission with respect to the particle trajectory.

Particle identification is important to an experiment whose primary motivation is charm production ($D^{\pm}$, or Λ_c) and ultimately strangeness detection from the weak decay of the charmed quark. The strange quark may dress itself as a charged kaon (e.g. from a D), or a Λ (e.g. from the charmed baryon Λ_c) which then decays to a proton and a pion. As such,(π,K,p) separation is preferable whenever possible. It is not necessary to find the actual velocity; establishing that the velocity is above a certain threshold is sufficient. We have chosen to use two gas threshold Cerenkov counters for our experiment.

The number of photons per cm. of path of the particle is given by

$$\frac{dN_p}{dl} = \frac{2\sin^2\Theta_c}{137} \frac{d\lambda}{\lambda^2} \text{ photons/cm.} \qquad (2.2\ )$$

This converts to the number of photoelectrons produced by the phototube as:

$$\frac{dN_{p.e.}}{dl} = N_0 \sin^2\Theta_c \qquad (2.3)$$

where N_0 is a number determined by the efficiency of the light collection system, the conversion efficiency of the photocathode, which varies as the wavelength of the incident photon spectrum, and the collection efficiency of the first dynode.

The problem of most Cherenkov counters is the low light level encountered. One must try to maximize the collection of the photons. This is done by means of an arrangement of mirrors and a focussing device known as a Winston cone. The latter is very effective in increasing the angular acceptance of the incident light cone. The Winston cone has the feature that light within some angle Θ_{max} with respect to the axis of the cone will be reflected onto the back surface via one or multiple reflections, the angle Θ_{max} depending on the front and back apertures of the cone.

RCA 8854 phototubes, with a 5" diameter, are chosen for their high gain at the first dynode, and high quantum efficiency ($\approx$ 27% at 400 nm.). The response curve of the efficiency for various wavelengths is shown in fig (2.12). For our system of effective phototube aperture (which determines the back aperture of the Winston cone), and the diameter of the front face of the Winston cone (= 15 "), Θ_{max} is $\simeq 18^0$.

From eqn(2.3) it is seen that the Cherenkov light output is inversely to the wavelength. Hence the number of photoelectrons in the ultraviolet range will be higher than, for example, the green. Unfortunately, the quantum efficiency of the phototube is fairly low at very high U.V. frequencies, as can be seen from the response curve. The quantum efficiency provided by the maufacturer does not reflect the collection efficiency of the first dynode, and this can be as low as 50 %. We have coated the face of the phototube with a wave shifter material (P-terphenyl) to improve the performance of the phototube at lower wavelengths.

The Winston cone is glued with epoxy to an aluminium adapter which also houses a quartz window. The purpose of the window is to keep the helium in the C2 gas mixture out of the phototubes, as helium slowly poisons the photubes. At the same time a quartz (suprasil) window allows wavelengths greater than 1600 A^0 to reach the phototube. The arrangement is repeated in C1. A lucite collar presses the quartz against an O-ring to form a gas tight seal. There are light fibres and plastic tubes (for gas circulation) that feed in through the lucite collar. The whole system is held in place by an aluminium frame. Fig 2.13 shows a schematic arrangement. Fig. 2.14 and fig. 2.15 show the schematic diagrams of C1 and C2, respectively.

The mirrors are held in place by a network of strings to minimise multiple scattering of the passing tracks. The nozzle part of C1 is painted black on the inside to reduce light signals from stray particles, background light from mirror reflections, etc. C1 is partly in the magnetic field of M2, and the phototubes are placed as far from the field as possible. The focussing in this case is handled by reflection off of two mirror planes. Horizontal shield planes of mylar in C2 contain the radiation from e^+e^- pairs associated with our photon beam. Furthermore, the mirrors in the upper and lower half in C2 (see table 2.2 for an idea of the segmentation of the mirrors) are separated by 3 cm. to reduce light from the pairs.

Cherenkov counters are most useful as threshold counters. The number of photons per unit length is seen to be proportional to $\sin^2\Theta$. Choosing the right composition of gas inside the Cerenkov counter such that the number of photons from pions is non-zero , while being zero from kaons, is the key to separation of the pions from kaons in the desired momentum range. The use of two Cherenkov counters further enables us to separate kaons from protons in a particular momentum range. This is done by an on-off procedure i.e. whether a track gives light on a mirror in one Cherenkov counter, both counters, or none.

For this experiment the gas mixture in C1 is chosen to be pure dry nitrogen ($n = 1+2.7 \times 10^{-4}$) and the mixture in C2 nitrogen and helium in the ratio by volume of 22:78, ($n = 1+1.2 \times 10^{-4}$).

Let Z = Length of the counter

$X_1(X_2)$ = Half of the length of the x coordinate of the upstream (downstream) face of the Cherenkov counter

$Y_1(Y_2)$ = Half of the length of the y coordinate of the upstream (downstream) face of the Cherenkov counter

P_{th} = Threshold momentum for a particle type

P.E. = The average number of photoelectrons.

Below is given a summary of the characteristics of the counters:

Table 2.1

COUNTER	Z	X_1	X_2	Y_1	Y_2	P_{th}			P.E.
	(metres)					pion	kaon	proton	
							(GeV/c)		
C_1	3.7	1.4	2.5	.64	.14	5.7	20.2	38.3	6.2
C_2	6.6	2.1	4.3	1.25	2.5	10.5	37.1	70.6	6.4

Also shown is a graphic view of the mirror layout (mirror size not to scale) in both C1 and C2, with the photoelectron yield for tracks of large momentum, all the light of the track being shed on one particular mirror. The differences in yield reflect the variation in efficiencies and gains and the angular distribution of Cherenkov light.

Table 2.2

C1

3.4	8.5		12.9		6.6
1.8	7.0	10.3	8.6	8.4	4.1
3.9	5.1	7.5	5.7	6.4	3.1
4.0	5.8		4.4		6.3

Table 2.3

C2

4.2	5.2		9.3		2.8
5.0	9.9	7.1	9.3	6.3	6.9
6.2	3.7	8.2	3.1	8.0	7.7
7.7	6.2		5.1		6.9

CALIBRATION OF THE CHERENKOV COUNTERS

There are several components to the calibration and routine checking procedure of the Cherenkov counters.

The number of photons generated per track is clearly seen to be dependent on the refractive index of the gas, and hence the composition. The main concern is with C2 as there is a mixture of nitrogen and helium. This is monitored on a daily basis by a gas chromatograph which enables one to obtain the percentage of the gasses in the mixture. However this method lacks in accuracy and it serves merely to note and correct any sudden changes in the percentages of the gas mixture. So this information is supplemented by threshold information from reconstructed pions, where we see from eqn (2.1) for $\Theta_c = 0$,

$$n = 1/\beta, \text{ where } \beta = \frac{E_{th}}{P_{th}} = \frac{1}{P_{th}} \sqrt{(P_{th} + m_\pi^2)} \ .$$

Thus, a plot of the number of photons as a function of momentum of the pion will show a rise above zero at a certain momentum for each counter, and the refractive index can be accurately measured from the threshold momentum. A representative plot of the number of photoelectrons measured versus predicted is shown in fig. 2.16 .

The Winston cone and mirrors are both aligned by a laser beam aimed from the centre of the target. The mirror/cone arrangement is adjusted such that the cone face is nearly at the focal length of the mirror. The mirror corner positions are obtained from an optical survey.

The ADC output from the phototubes has to be converted into meaningful pulse height values. Laser light passes through a transmission wheel with neutral density filters, to send low intensity light into the photutubes via light fibres. Low light levels enable one to observe single photoelectron peaks where the ADC response is fairly linear. The gain of the phototube in counts per photoelectron is given by the pedestal subtracted ADC value at the single photoelecton peak. The average response of the system is 15 ADC counts per photoelectron. During normal data running, the pulse height in terms of photoelectrons corresponds to the pedestal subtracted ADC value divided by the gain. Let this be denoted by N_{obs} per cell. This is compared to the number of photoelectrons predicted (N_{pred}) for a reconstructed pion with known momentum and hence a known β. This provides us with the efficiency (ε) of each cell where N_{obs} is equal to $\varepsilon \cdot N_{pred}$. This efficiency is the result of the inefficiencies from the mirror reflectivity, the Winston cone reflectivity, light losses in Winston cone acceptance, the response of the photocathode, and the electronics.

THE MAGNETS

The spectrometer uses two magnets, each of integrated field of 5 Kg-metres and mean P_t deflection of 150 MeV/c. The field shape of the magnets is measured using Zip-Track[18], which is a computer aided device to map the field in X, Y, and Z. This map is then used to find the coefficients of a polynomial fit that represents the measured B field. Finally, the reconstruction program uses this information in its iterative procedure to find the momentum, slopes and intercepts of charged track candidates.

THE C COUNTER

The central C counter, located downstream of D4, is a 20 radiation length tungsten lucite calorimeter used for the detection and energy measurement of non-interacting beam photons. In addition there are two side counters, C-East and C-West, for detecting showers from photons which convert in the target and have some lateral spread from the magnetic bend. This is crucial for estimating the photon spectrum as well as the energy of the interacting photon(s) in case of multiple bremstrahlung. As such, this device is also used for the calibration of the tagging system lead glass blocks. The number of radiation lengths is sufficient to prevent contamination of the SLIC by shower spillage. LE-CROY 2249 ADCs digitise the anode pulse on the phototubes, and this information is written on to tape.

THE SLIC (SEGMENTED LIQUID IONIZATION COUNTER)

The SLIC, shown in fig. 2.17, is a segmented calorimeter for the detection of showers from electromagnetic particles such as electrons, positrons, photons, etc. Neutral hadrons such as neutrons also start showering in the SLIC and hence it has to be used in conjunction with the hadron calorimeter (hadrometer). The hadrometer identifies neutral hadrons after "subtracting out" the energy deposit of observed showers from charged particles.

The SLIC has 60 layers (20 radiation lengths) of lead-liquid scintillators, 20 layers per view Y (horizontal), U (+20.5 degrees with respect to the vertical) and V (-20.5 degrees with respect to the vertical). Each layer is segmented into 1.25 inch strip hodoscopes by aluminium corrugations. These segments are teflon coated so that the light is fairly well contained by total internal reflection. The light at the end of the layers is collected and wave shifted (to reduce loss of light by reabsorption) for each of the 20 layers per view. Light is channelled via wave shifter bars to phototubes. These tubes are held at 45 degrees to the wavebar for maximum transmission efficiency. The anode signals provide a pulse height proportional to the shower energy deposit and the sum of the dynode signals are a component to the hadronic (H part of the TAG•H) trigger. Digitised anode signals are written to tape for further analysis.

THE OUTRIGGER

The purpose of the outrigger (fig. 2.18), also an electromagnetic calorimeter, is to provide information on large angle (greater than 40 mr.) electromagnetic particles which may have missed the SLIC. The outrigger has an upper and a lower module, each module consisting of 16 layers (18 radiation lengths) of lead plastic. The segmentation here, in contrast to the SLIC, is done in alternate layers of X and Y. The phototubes, which are in the magnetic field fringe of M2, are shielded by steel casings and conetic shielding. Again, wave shifter bars ensure minimal loss of energy from reabsorption of the scintillation light. As with the SLIC, the summed dynode signals provide a component to the hadronic trigger.

THE HADROMETER

The most important function of the hadrometer is the measurement of total energy of a hadronic event for use in a fast trigger (see chapter III). The energy resolution (74%/√ E) of our hadrometer (fig. 2.19) is poor. However it can be used to identify neutral hadrons in the anaylsis. The information on charged hadrons (obtained in conjuction with drift chamber information) is used to obtain the energy deposit of neutral hadrons by subtracting the charged energy deposit from the total observed value. The identified neutral hadrons are used by the SLIC to help in distinguishing the neutrals from photons.

The hadrometer is segmented into identical front and back halves. Each half consists of 18 layers, each layer being of 1 inch wide steel and 3/8 inch wide acrylic scintillator. Segmentation of the scintillator occurs in X and Y ,there being 33 vertical strips in X, and 19 horizontal strips in Y. The 19 horizontal strips are actually divided into two at the centre, thus totalling 38 strips. A channel is defined as 9 segments and the light is guided by lucite strips to a phototube. The summed dynode signals are used as a component of the hadronic part of the TAG•H trigger, to be described later. The digitised anode signals are written to tape.

THE MUON COUNTER

Muons traverse another 6 interaction lengths of steel which stops most of the remaining hadrons. There follows an arrangement of hodoscopes for detection of the muons by showering in scintillators. The muon information is subsequently used in the J/ψ analysis for its $\mu^+\mu^-$ decay mode.

CHAPTER III

TRIGGERS

A trigger is determined by the type of information one wishes to extract from a particular interaction. In this experiment there are two different levels of triggers[19-20]. We define them as the low and the high level trigger.

First we discuss the low level trigger. The fast low level trigger starts the digitisation of the information from the drift chambers and the calorimeters. Low level triggers are non-beam associated and beam associated.

Non-beam associated triggers are scheduled by the Black-Box which is a device for ordering the test pulse generation and the firing of the lasers. It is manipulated by manual switches and/or by software. These triggers include the laser for the recoil detector, the laser for the downstream calorimeters and Cherenkov counters, a test pulser for the pedestal check and drift chamber calibration strobes.

Beam associated triggers will be discussed in some detail. They are the following:

TAG•H : This is the primary low level trigger of this experiment. The TAG requires a bremmstrahlung photon to be tagged by the measurement of the secondary electron in the tagging system. The H part of the trigger is the hadronic component that was mentioned in connection with the calorimeter descriptions of chapter II. This will be described in more detail.

The prime requirement of the hadronic trigger is that the hadronic energy E_{had} be greater than some fraction X (< 1) of the incident photon energy. At very low values of X the measurement of the E_{had} is contaminated by the large electromagnetic cross section. At high values of X the hadronic efficiency becomes poor due to the energy resolution of the SLIC and the hadrometer. The value of X actually chosen is .4 - this provides 97 % efficiency for hadronic events, with a small contamination from pairs.

Thus we have $E_{had} > .4 \times (E_e - E_{e'})$

where E_e = energy of incident electron (170 Gev)

$E_{e'}$ = energy of the electron entering the tagging system

E_{had} = energy in the SLIC outside the pair plane
+ energy in the Outrigger
+ 5 x the energy in the hadrometer

E_{had} is determined from the dynode signals of the outrigger, SLIC, and the hadrometer. The factor of 5 is used to boost the detected hadronic energy for those events on the low energy tail of the hadrometer resolution.

This trigger is prescaled before being written to tape.

PAIR: Pair production of the photons. These events are used for SLIC calibration.

GAMMA: Presence of non-interacting photons (detected by the C counter). This trigger is used to calibrate the tagging system, and is also pre-scaled.

DIMUON: This trigger has been set to study the J/ψ decaying into the $\mu^+\mu^-$ mode.

These triggers are in coincidence with the Beam Gate and are only vetoed by the Experiment BUSY (signifying that an event is being read into CAMAC) or the trigger processor BUSY (which implies that the processor is trying to make a decision on the RECOIL trigger). A low level trigger is passed onto the high level stage for a decision on whether to record the data.

A high level trigger is the main event selection trigger and results in flagging the computer as being busy (COMPUTER BUSY), causing data to be read by the computer from the appropriate CAMAC modules. Subsequently, a CLEAR is generated which clears all CAMAC modules to prepare for the next event. There are 13 high level triggers :

1.) The four low level triggers (TAG•H, e+e−, GAMMA, and the non-beam test) which are passed as candidates for a high level trigger.

2.) Five are reserved for the user.

3.) Four recoil triggers passed on by the trigger processor.

The recoil triggers are the main triggers for diffractive event selection and are explained below, including the role played by the trigger processor.

THE TRIGGER PROCESOR AND THE RECOIL TRIGGER

The trigger processor[20] of E-516 is one of the first of its kind to be used in a high energy experiment. It selects diffractive events with forward mass between 2 - 11 Gev/c^2 in typically 10 microseconds. The TAG.H rate is 1500 - 2000 per second including the pair contamination. Read-in time for the CAMAC system is 3 milliseconds per event. Thus for 30 % dead time the number of events that can be read in is only 100 events/second. This is where the selection criteria of high mass diffractive trigger is necessary to reduce the TAG.H rate to 100 events per second.

Information from the recoil detector is passed to the processor which then processes it in several steps.

1.) The anode readout supplies the azimuthal angle information of a charged track. Cathode hits are scanned, with the most upstream hits being considered first. The processor then computes the centroid and width of the cluster of hits.

2.) The " track finder " loops through all possible track combinations from PWC cathode information and stores the slope and vertex position of each track into two data stacks. It starts processing when at least one centroid from each chamber had arrived.

3.) The main loop of the processor starts with the first entry into the stack and matches the track to scintillator sectors.

4.) The sector matching is a loop by itself. This is determined from comparing the position of the projection of the track into the A layer and matching it with the end-to-end (E-E-T) timing, within resolution. If there is no match this track is called a NO-MATCH.

5.) The tracks are flagged as electrons, charged pions or protons according to the energy deposit in the scintillators.

6.) The charged tracks at the most upstream vertex are counted and if one of the tracks at this vertex is likely or definitely a proton, it is noted.

7.) There is also a loop that cycles through all the 15 sectors to look for neutrals.

8.) The forward mass is calculated from the photon energy, the recoiling proton energy, and the recoil angle. Thus, when all the tracks have been processed by the main loop, the scalar information, the neutral information, and the missing mass are used for a triggering decision.

The average time for steps 1-6 is of the order of 10 microseconds.

The final recoil diffractive trigger is a single identified proton at the most upstream vertex, no neutrals (to decrease contamination from N* decays into $p\pi^0\pi^0$, $p\pi^0$ etc), and no more than two NO-MATCHes and backward tracks. To avoid complicated events, those with more than 8 tracks in the recoil detector are rejected.

Thus, the recoil bit is set according to the following four categories:

1.) RECOIL 1 $0 < M_x(GeV/c^2) < 25$ (prescaled by 29)

2.) RECOIL 2 $2 < M_x$ $GeV/c^2) < 5.5$

3.) RECOIL 3 $5.5 < M_x(GeV/c^2) < 11$

4.) RECOIL 4 Greater than 2 recoil charged tracks at the primary vertex.

These triggers form the major fraction of the events written to tape.

CHAPTER IV

RECONSTRUCTION

Reconstruction is the tedious process of assimilating the information of TDC's and ADC's into a format that can be understood and used by the person performing the analysis. In this thesis the reconstruction procedures discussed will be related to the drift chamber and the Cherenkov counter, with an extension on the selection criteria of Vees (neutral kaons, lambdas, and antilambdas).

DRIFT CHAMBER RECONSTRUCTION

The TDC's essentially output time information for a particular wire per assembly per drift chamber with the correlation:

$$T = T_0 + G \times TDC$$

T = Time in nanoseconds
T_0 = Time at some reference point
G = Gain of the TDC in nanosecond/count
TDC = TDC count

There are two T_0's one has to contend with for the drift chamber assemblies. One is the relative T_0 which is a measure of the difference in timing for different wires in the same plane. The other is the absolute T_0 which is an overall correction for the relative differences in time for different assemblies.

The position information is obtained by the equation x=vt, where v is the drift velocity, which is a function of the field surrounding the sense wire. The drift velocity has been obtained by elaborate calibration procedures described in great detail in all previous theses from this experiment. Hence it will not be elaborated upon here.

The drift chamber analyst has at his disposal the hit distribution of the wires in the different assemblies from which he can form likely candidates for charged tracks by matching segments in each chamber to form a complete track.

The procedure is to look at U V X triplet of hits in the three assemblies of D3, and search for a segment of the trajectory which projects back to the target in the y (non-bend) view. Acceptance criteria is imposed e.g. the number of hits found in D3 must be at least 7, the maximum possible being 9.

This segment is then matched with a compatible prediction from the projection of the D3 segment into D2 in the non-bend y view. A consistency check is performed to ensure that the x value of the D2-D3 segment is consistent with that of a track coming from the target. The magnetic field of M2 between these two chambers is of course taken into account.

These candidate segments are matched to ones in D1 and D4 to form a complete track for those that traverse all four drift chambers. These are the tracks that have the best momentum resolution. We are left with the search for segments that do not fit into any of the above mentioned categories. At first, we search for D1-D2 tracks. An attempt is made to connect unmatched D2 line segments (with at least three hits associated with it) to a D1 segment.

The segments in D3 that have no corresponding match in D2 are the starting point for a D3-D4 track search. Again by segment matching, with cuts on the minimum number of hits associated with it, we obtain strong candidates for D3-D4 tracks.

Now we are in a position to search for D1-only segments, looking away from the high-rate and cluttered central region of the chamber. Candidate segments are stored if there are at least five hits associated with it and the momentum of the track segment is greater than 200 MeV/c.

Finally, up to 20 of the best of all tracks (within quality criteria) are stored in the track array. The primary vertex is found from all the tracks except D3-D4 tracks. An iterative fit is performed from the final list of tracks for a charged track in a magnetic field. The five parameters of the fit are the inverse of the momentum, x and y intercepts, and x and y slopes of the track. These parameters are also stored in the track array.

A bit is also set which categorises the track according to the chamber it intercepts e.g. bit 1 is set if the track made it through D1, bit 2 is set for D2 etc. The table below shows this.

Chamber	Bit No.	Category
D1	1	1= 2^0
D2	2	2= 2^1
D3	3	4= 2^2
D4	4	8= 2^3

Thus, a D1-D2-D3-D4 track is labelled as

$$\text{JCATSG} = 1 + 2 + 4 + 8 = 15.$$

Also stored are the number of degrees of freedom of each track where :

D.O.F. = Number of hits for the track
- the five parameters of the fitting equation

Needless to say, the person analysing the data may impose further cleanliness cuts to enhance a particular type of signal and weed out the background.

A further note may be added on the problem of detector dead-time associated with high rates in the central region of the drift chambers. If we plot the $x - y$ position of the reconstructed tracks at any z position, we see a "hole" i.e. depletion of intersection points in the central region. The region of the "hole" is mostly in $-8 < x < 8$ cm and $-.8 < y < 1.2$ cm. This effect has been studied, and the conclusion is that when the event rate is high, the drift chamber is saturated in the region of largest track density, and the recovery is not complete in time for the next spill. Hence, the chamber becomes inefficient. This effect is simulated in the Monte Carlo and will be discussed in Chapter V.

CHERENKOV RECONSTRUCTION

The threshold information of the counters (namely the on-off behaviour described in chapter II), is a good starting point, but not entirely sufficient to extract the complete information on particle identification. There were two different approaches towards estimating the probability of a track being of a certain type (e,μ,π,K,p) by combining physics intuition with known inefficiencies of phototubes and reflecting surfaces. The particular method used in this thesis will be discussed in some detail.

The type of particles under consideration are electrons(1), muons(2), pions(3), kaons(4), and protons(5). The numbers 1-5 shall henceforth refer to the particle type. The muons are identified via the muon counter, and the electrons are identified using both the Cherenkov counter and the SLIC. So the main task lies in distinguishing pions, kaons, and protons.

Let us isolate a relatively unambiguous set of tracks which are within the fiducial volume of the Cherenkov counter and which are not in the pair plane of C_2. A set is a track or a group of tracks such that the cone of Cherenkov light for each track points to mirrors which do not share light from other sets.

Let the pulse height analysis for each cell give us a measured number (N_{obs}) of photoelectrons. The task is to obtain the probability of the track being of the mass hypothesis i for N_{obs}.

The angle of the Cherenkov light Θ_c is known from the refractive index of the medium (n) and the β (=P/E =v/c) of the track, where $\cos \Theta_c = 1/(\beta n)$. This allows us to project the cone of light onto the mirror plane, thereby establishing the fraction (F) of light actually intersecting the mirror. The track length inside the Cherenkov counter is divided into 12 and 10 segments in C1 and C2 respectively, and the mean number of photons from each segment computed assuming a particular mass hypothesis. The sum over all segments weighted properly by F will be the predicted number of photons for a mass hypothesis i. Let $N_m(i)$ be the mean number of photons obtained by the above procedure for a mass hypothesis i.

The first step is to smear the prediction N_m by a Gaussian (G) to account for the varying collection efficiency of each cell (defined by a single mirror or a cluster of mirrors focussing to a single phototube). The width of the Gaussian is proportional to N_m, where N_m is the mean of the Poisson distribution (P) for photon generation and photostatistics.

Thus, the probability that N photons will be incident on the photocathode is given by

$$P_i(N) = P \times G = C\int dN' \frac{(N')^{N'}}{N!} e^{-.5 \frac{(N'-N_m)^2}{\sigma^2}}$$

This $P_i(N)$ is a discrete distribution. To account for the response of the photomultiplier tube and the electronics associated with the cell, this discrete distribution is further smeared by a Gaussian to represent the ADC output. The result is the probability $P(i,N_{obs})$.

$$P(i,N_{obs}) = \Sigma\, C'\, P(N)\, e^{-.5 \frac{(N - N_{obs})^2}{\sigma_N^2}}$$

This is the probability of observing N_{obs} photoelectrons with a mass hypothesis i.

We invert this to obtain the probability $Q(i,N_{obs})$ of the track being of the mass hypothesis i for a given N_{obs}.

Hence, we can write, $Q\,(i,N_{obs}) = A(i) \times P\,(N_{obs},i)$ where A(i) are the apriori or consistency probabilities of the mass hypothesis i. The A(i) are initially given some nominal value from the particle yield expected from an interaction of this nature, and then iterated to converge to the values used in the data analysis.

These probabilities $Q(i,N_{obs})$ are denoted henceforth as Prob(track number, mass hypothesis).

We use this probability method to compute the joint probability. For example, we ask what is the probability of the two candidate tracks in a lambda search to be really part of the lambda. Here it is the Cherenkov identification of the proton that discards much of the background.

Let us label the proton as i and the pion candidate track as j. Then we can define a joint probability of the combination as

PROBLA = Prob(proton) x Prob(pion) where all labels have been defined in the text.

As the proton cannot be distinguished by mere on-off procedure in the Cherenkov counter below a momentum of 21 Gev/c (kaon threshold in C1), and as the window for muon and pion separation is very small, we can further define the following:

Prob(proton) = Prob(i,5) (momentum of i>21 Gev/c)

= Prob(i,4)+Prob(i,5) (momentum of i<21 Gev/c)

Prob(pion) = Prob(j,2)+Prob(j,3)

Similarly, we can define the joint probability of the two pion candidates for K_s^0 as

PROBKS = Prob(pion^1) x Prob(pion^2)

In figs 4.1a, 4.1b, 4.1c we show the variation of the ratio of the signal to background for neutral kaons, lambdas, and antilambdas. Also shown on the same plots is the relative loss of signal and background with increasing harshness of the cut in probability.

RECONSTRUCTION OF VEES

This section deals with the process of extracting particles such as Ks^0, Λ, or Ξ (sometimes referred to as Vees) which decay weakly and hence have a long lifetime. The latter implies that the decay point may be distinguished and separated from the primary interaction point. One may of course do the obvious and compute the invariant mass of all oppositely charged tracks assigning each a mass of the pion, for the case of the K_s^0. This leads to an enhancement in the K_s^0 region of .4977 GeV/c^2, as shown in fig. 4.2. The same process may be applied to the case of a lambda (or antilambda), where the faster track is assigned a proton mass, and the slower one a pion mass. This is shown in fig. 4.4 for lambdas, and fig. 4.6 for antilambdas.

The Vees obtained by this method also contain an enormous background (ratio of signal to background is .11 for K_s^0's and .07 for Λ's for a Cherenkov probability greater than .1) and hence some characteristic properties of Vees are applied to decrease some of the background. After imposing the Vee selection routine, the ratio of signal to background becomes .57 for K_s^0's and .32 for Λ's, again with the same Cherenkov probability cut. Unfortunately, this is at the expense of the signal. Fig. 4.3 shows the invariant mass of the K_s^0 after the Vee selection routine. The lambdas and antilambdas obtained from the Vee routine are shown in figs. 4.5 and 4.7 respectively. The solid curve shows a fit to a quadratic background and a Gaussian signal.

The procedure to select a clean sample of Vees is to first obtain all the tracks that belong to the primary vertex, and from the remaining sample of tracks, select the candidates for the secondary vee vertex. We group all the tracks in the recoil detector into bunches depending on the resolution of the z position of the tracks at the target. For the ideal case of a clean diffractive proton, there would be only one charged track at the most upstream vertex, and any other vertex is labelled as a secondary vertex. Using the first candidate vertex, all the other recoil and forward system charged tracks are processed to see if any, all, or none of them appear to come from the candidate vertex, using the known errors on the momentum and position of the drift chamber tracks. A decision is made on whether this candidate vertex passes acceptability criteria. If not, the next downstream vertex is similarly appraised. If no suitable vertex can be found, this event is rejected. So, if there is a primary vertex, then we have a list of tracks which have an acceptable chi-square contribution to the primary vertex.

We are left with a list of tracks which do not apparently come from the primary vertex. These are paired (taking oppositely charged candidates) and the distance of closest approach between these tracks (DITT) is required to be less than 10 cm, as a first pass. Should the tracks pass this criteria, then the distance of closest approach (DITV) between the resultant momentum vector of the candidate Vee and the primary vertex is computed. This cut is fairly loose and set to 10 cm. So as not to deplete the cascade or charged hyperon particles, which would have a double vertex (Ξ decays to a $\Lambda + \pi$, and the Λ then decays to a $p + \pi$), up to three tracks are allowed to be pointing to the same secondary vertex. Finally, as Vee vertices cannot physically be upstream of the primary vertex, only those downstream of the primary vertex are accepted. The last cut actually is responsible for a loss of nearly 40% of the Vee candidates.

As an exercise we have estimated the improvement in signal to background by successively decreasing DITT and DITV, and noting the loss in signal and background separately. The figs. 4.8 - 4.11 show this improvement for the best case when both tracks are category 15 (JCATS = 30) and the worst case when both tracks are category 3 (JCATS = 6).

For the inclusive studies of the K_s^0's and Λ's, the Vees found by the method outlined in this section will not be used, as the number of Vees are depleted, for reasons mentioned previously. For the latter part of the analysis where we estimate the upper limit on the cross section of production of the charmed baryon Λ_c, we use the cleaner sample as we have to try to extract the small (if any) signal from a large background.

CHAPTER V

MONTE CARLO TECHNIQUES

Simulation of the data to as high a degree as possible is important in understanding the inefficiencies of the detector and the sources of the loss. Starting from a basic dynamic model for the generation of the event one then introduces the geometrical limits of the apparatus, and the resolution of the data from relevant studies. The CERN GEANT package was adapted for the specifications of the E-516 detector. We will briefly cover the event generation technique, and then the detector limitations introduced from known sources of inefficiences.

The transverse momentum (P_t) limited phase space generator of Carey and Drijard[21] is used, as limited transverse momentum is a characteristic of high energy interactions. The phase space term is an integral over a term function $F(\rho)$ which contains information of the production amplitude as well as experimental biases, where ρ itself is a function of the four momenta of the particle. We may divide the 3-momentum into longitudinal (l) or transverse (t) parts as

$$p = p_l + p_t$$

The $F(\rho)$ can be decomposed into transverse and longitudinal parts, the latter being a function of both p_l and p_t.

$$\text{Thus, } F(\rho) = F_l \times F_t$$

$$= F_l(\{ p^l \},\{ p^t \}) \times F_t(\{ p^t \})$$

The transverse momentum p_t dependence is much stronger in F_t than in F_l. If we assume that the transverse amplitude can be written as a product over single particle amplitudes, we may write

$$F(\{ p_i{}^t \}) = \prod_{i=1}^{n} f(\{ p_i{}^t \})$$

the index running over the produced particles.

In the method of Drijard and Carey, the transverse components are first evaluated with a given distribution, (exponential in our case), followed by the longitudinal amplitude. The latter depends upon the transverse amplitude, and hence the order. A change of variables is made such that all variables range from 0 to 1 for compatible use with random number generation. Energy and momentum conservation leads to some event rejection, and we are left with a new set of generated transverse momenta .

The electron beam of 170 GeV interacts with a Copper radiator of 18% radiation length and up to four bremstrahlung photons are allowed for the event. If any of the photons interact in the hydrogen target, then the photon-proton interaction has a forward mass associated with it (M_x). The t distribution is generated as e^{-bt}, as is observed for diffractive dissociation events. b is the slope of the exponential behaviour of the cross section $d\sigma/dt$ and decreases from 6 to 3 as the forward mass increases from 2 GeV/c^2 to 11 GeV/c^2. As defined before, t is the four momentum transfer to the recoiling proton, and is given by

$$\begin{aligned} t &= (P_i - P_f)^2 \\ &= 2m_p\,(m_p - E_p) \qquad (5.1) \end{aligned}$$

m_p = mass of the proton

E_p = energy of the recoiling proton

P_i = four momentum of the target proton

P_f = four momentum of the recoiling proton

The t distribution is observed to flatten as M_x increases, and this behaviour is included in the generation by varying the slope parameter. With this information (i.e. the energy available for the generated particles), the multiplicity is generated from the KNO distribution[22] as the predictions from such a distribution are in good agreement with data from e^+e^- and hadron collision experiments.

The production of the particles is such that strangeness and baryon number are conserved. Also, the average number of positively charged, negatively charged, and neutral particles are equal. One K_s^0, one charged kaon, and the balance a mixture of charged and neutral pions, would be one example of K_s^0 production. For lambdas, - one lambda, one antilambda, and a mixture of charged and neutral pions would be one possibility of production. The multiplicity and the total available energy (M_x), along with the masses of the particles produced in the reaction are the input to the P_t limited generator described above. The output are the four momenta of the produced secondary particles. This is processed by GEANT (a standard CERN Monte Carlo package) for digitisation of the intersection points of the charged tracks with the drift chamber planes. Subsequently this is converted to TDC counts to simulate the data, feeding in the known resolution of the chamber. As mentioned in chapter IV, the inefficiency in the central region of the drift chambers is also simulated. The size of the inefficient region is shown for D2 (module 1) in fig. 5.1. This inefficiency is simulated by a function F expressed as a product of two Gaussians, one in x, and one in y:

$$F = e^{-\frac{(x)^2}{81}} \; e^{-\frac{(y - .8)^2}{.9}}$$

D_2 is the chamber where hits are deleted, as this is one of the central chambers. Hence, if the random number is less than F, the hit in D_2 is kept. The comparison of efficiencies in the x view (fig. 5.2) and the y view (fig. 5.3) shows the agreement to be reasonable, at best.

The charged tracks are tested for Cherenkov emission in the Cherenkov counters, and where applicable, the average photoelectron values are noted.

The first pass of the data simulation processes these events as if they are data hits on the chambers and outputs the track information in an array identical to the data format. The second pass then uses the ADC information and the reflectivity of the mirrors, and inefficiencies of the phototube, to output the Cherenkov probabilitites in a manner similar to the treatment of the data.

This is then available to the user for further analysis.

We go one step further and simulate the t distribution of the recoiling proton.

The recoil detector can only detect and identify protons in the t range of -.06 (GeV/c) (i.e. it must have at least 50 MeV of kinetic energy) to -1.4 (GeV/c) . Protons with t outside these limits are rejected. In fig. 5.4 we show the angular acceptance of the proton as a function of t. As can be seen, the recoil detector cannot accept protons below 20 . For the Monte Carlo simulation protons in the lower boundary of t - curve are accepted.

From fig. 5.5 we can obtain the fiducial acceptance of the recoil proton in terms of theta, and a recoiling proton outside the lower boundary is rejected. This leaves us with a sample of recoil protons simulating the t distribution of the data, the comparison being shown in fig. 5.6 . Also shown in fig. 5.8 is its comparison with the original uncorrected t distribution of the recoil proton. The difference, which reflects the theta efficiency, is 85%.

In fig. 5.7 we compare the multiplicity of M.C. reconstructed tracks with data tracks for K_s events, and the match is excellent.

We now approach the problem of simulating the forward mass spectrum. The forward mass distribution at low masses is not the same for the Vee events as it is for general hadronic events. This is primarily because of the small phase space available for the Vee formation at low masses. There is also a falloff of the mass curve at higher masses and hence we need a term that corrects for this effect.

To a first approximation, we have used a mass dependence of the form

$$\frac{d\sigma}{dM_x^2} = a + \frac{b}{M_x^2}$$

However this is only correct far away from phase space limits. Hence we include a phase space contribution factor where the dependence of the density of states on the forward mass is taken into account.

The phase space factor is given by :

$$\rho = \frac{d^3P_\rho}{2\ E_\rho} = \frac{P_\rho^{\ 2}\ dP_\rho\ d\Omega_\rho}{2\ E_\rho}$$

In the centre of mass of the γ p system,

$E_p + E_X = W$ (the centre-of-mass energy) (a)

$P_p = P_X$ (b)

Squaring a.) and rearranging, we have

$$E_p = \frac{W^2 + m_p{}^2 - M_x{}^2}{2W}$$

Also, from $E_p{}^2 = P_p{}^2 + m_p{}^2$, we have $E_p dE_p = P_p dP_p$

Therefore, $\rho \propto P \dfrac{dM_x{}^2}{2W}$

Hence,

$$P_p{}^2 = (E_p{}^2 - m_p{}^2) = \left(\frac{W^2 + m_p{}^2 - M_x{}^2}{2W}\right)^2 - m_p{}^2$$

Thus,

$$\frac{d\sigma}{dM_x{}^2} = \left\{a + \frac{b}{M_x{}^2}\right\} \times \frac{P_p}{2W}$$

$$= \left\{ a + \frac{b}{M_x{}^2}\right\} \frac{1}{2W} \left\{\left(\frac{W^2 + m_p{}^2 - M_x{}^2}{2W}\right)^2 - m_p{}^2\right\}$$

The values of a and b that fit the data very well are :

$a = 1.$ $b = 2$ for $K_s{}^0$

$a = 1.$ $b = .5$ for $\Lambda, \overline{\Lambda}$

The result of each new term added to the original flat $M_x{}^2$ distribution is shown in fig. 5.9 .

We also show in figs. 5.10 and 5.11 the comparisons of $K_s{}^0$ and Λ data events with Monte Carlo reconstructed events i.e. analysed as if they were data events, to take into account biases of programming etc.

EFFICIENCIES FOR KSHORTS / LAMBDAS / ANTILAMBDAS

The efficiencies tabulated indicate the losses due to the following geometrical cuts:

1.) Let i and j be the track labels of the two tracks of the Vee. The tracks i and j must have entered the second drift chamber. This gives the geometrical acceptance as the track has a reported momentum only after this chamber.

2.) At this point we only keep tracks whose parent Vee has decayed before the first magnet. This gives a measure of the reconstructability of the Vees i.e. the remaining sample is reconstructable.

3.) The tracks are then matched by an algorithm which matches generated M.C. tracks with reconstructed M.C. tracks. This is done by comparing the

$$(\quad P_x) /p_x \; + (\quad P_y) /p_y \; + (\quad P_z) /p_z \quad)$$

and making an appropriate cut at .15, as shown in fig 5.12. Multiple tracks which fall into this cut are then treated separately to obtain the best match.

P_x= p_x (x component of M.C. track)

- P_X (x component of reconstructed M.C. track)

P_y= p_y (y component of the M.C. track)

- P_Y (y component of reconstructed M.C. track)

P_z= p_z (z component of the M.C.track)

- P_Z (z component of reconstructed M.C. track)

This step is a measure of the reconstruction efficiency.

4.) The mass of the i+j track using the reconstructed momentum variables is then required to be within 3 of the measured values obtained from data. For the K_s 's this corresponds to

M(i+j) = .497   .021 GeV/c , and for the lambda/antilambda sample M(i+j) = 1.115   .009 GeV/c .

5.) Cherenkov probability cuts are applied to the M.C. tracks as if they were data tracks. The Cherenkov cut on the Vees is the same as used in the data, namely: the product probability of the two tracks must be greater than .1 for K_s^0 and .12 for lambdas and antilambdas. Comparisons of Cherenkov probabilities from Monte Carlo and data for neutral kaons, lambdas and antilambdas are shown in figs. 5.13 - 5.15. The comparison for the lambdas and the antilambdas is very good. The neutral kaon comparison is only reasonable, but the fraction of events lost for K_s 's with a probability cut of .1 is less than 2%, and hence this discrepency is not important.

6.) Finally, M.C. events are used to obtain the efficiency of the curve (quadratic background plus a Gaussian for the signal region) used to fit the mass distribution. This includes the efficiency of the HBOOK (CERN histogramming package) fitting routine itself.

The tabulated results in tables 5.1 - 5.6 are the efficiencies after steps 1 - 5. We give below an idea of the average fraction of events kept for Monte Carlo K_s and   sample in steps 1 - 6.

Step	Fraction of events kept from total	
	K_s^0	Λ
1- 6	.32±.04	.42±.04

The efficiency curves for steps 1-5 are plotted in figs. 5.16 - 5.24. The errror bars are a representation of the magnitude of the statistical errors.

The resolution on the momentum of the tracks is dependent on the quality of the track - category 3 tracks have a larger error on the momentum than category 15 tracks. Fig 5.25 shows the momentum resolution as obtained from the Monte Carlo. Alongside in fig 5.26 is the resolution $\Delta M_X/M_X$ of the forward mass M_X.

Table 5.1

Efficiencies as a function of Forward Mass M_X

All tagging energies

Mx GeV/c ^{2}	K_s^0	Λ	Anti Λ
2- 4	.48±.01	.35±.01	.35±.01
4- 6	.46±.01	.48±.01	.48±.01
6- 8	.40±.01	.51±.01	.52±.01
8-10	.39±.02	.51±.01	.50±.01
10-12	.33±.03	.45±.03	.47±.03

Table 5.2

Efficiencies as a function of Z

All tagging energies

Z	K_s^0	Λ	Anti Λ
.05-.1	.55±.01	.56±.02	.57±02
.1-.2	.56±.01	.53±.01	.53±.02
.2-.3	.46±.01	.41±.01	.40±.01
.3-.5	.33±.01	.28±.01	.29±.01
.5-.7	.22±.02	.21±.03	.23±.03

Table 5.3

Efficiencies as a function of E_{avail}

E GeV	K_s^0	Λ	Anti Λ
8-10	.49±.02	.52±.02	.53±.02
10-12	.48±.01	.49±.02	.50±.02
12-14	.43±.01	.43±.01	.43±.01
14-16	.40±.01	.37±.01	.37±.01

Table 5.4

Efficiencies as a function of P_t^2 in the lab

All tagging energies

P_t^2 $(GeV/c)^2$	K_s^0	Λ	Anti Λ
0.-.1	.44±.01	.42±.01	.42±.01
.1-.2	.45±.01	.4±.01	.48±.01
.2-.3	.45±.01	.50±.01	.50±.01
.3-.5	.44±.02	.48±.02	.50±.02
.5-.7	.41±.02	.49±.03	.50±.03
.7-1.	.38±.03	.42±.03	.48±.03

Table 5.5

Efficiencies as a function of Feynman X

in the Overall C.M.

X_{of}	K_s^0	Λ	Anti Λ
(-.05)- (+.05)	.47±.01	.59±.02	.60±.02
(+.05)- (+.1)	.53±.01	.55±.01	.55±.01
(+.1) - (+.2)	.53±.01	.45±.01	.44±.01
(+.2) - (+.3)	.43±.01	.35±.01	.34±.01
(+.3) - (+.4)	.35±.01	.27±.01	.28±.01
(+.4) - (+.5)	.28±.02	.23±.02	.22±.02
(+.5) - (+.7)	.23±.02	.17±.02	.20±.02
(+.7) - (+.9)	.20±.03	.15±.07	.22±.07

Table 5.6

Efficiencies as a function of Feynman X

in the Forward C.M.

X_{ff}	K_s^0	Λ	Anti Λ
(-.7) - (-.5)	.16±01	.46±.03	.46±.03
(-.5) - (-.3)	.26±.01	.52±.02	.52±.02
(-.3) - (-.2)	.36±.01	.53±.01	.53±.01
(-.2) - (-.1)	.48±.01	.49±.01	.51±.01
(-.1)- (-.05)	.57±.01	.46±.01	.46±.01
(-.05)- (+.05)	.59±.01	.45±.01	.43±.01
(+.05)- (+.1)	.56±.01	.37±.01	.37±.01
(+.1) - (+.2)	.48±.01	.35±.01	.34±.01
(+.2) - (+.3)	.39±.01	.31±.02	.30±.02
(+.3) - (+.5)	.28±.02	.24±.03	.22±.03
(+.5) - (+.7)	.22±.03	.18±.04	.18±.04

CHAPTER VI

CALIBRATION CHECK OF THE RECOIL DETECTOR

This experiment is unique in its triggering on the forward mass M_X defined in chapter II. The number of $K_s{}^0$s, lambdas, and antilambdas per hadronic event in the rest frame of M_X is one of the tests of the similarity of the dynamics with e^+e^- annihilations. However, for this comparison to be meaningful, we must be sure that we have selected an event where the recoiling proton is the only recoiling particle, as otherwise the M_X for the event will not be correct. Also we will have no clear evidence that we have a diffractive process. In this chapter we will discuss the steps we have taken to check that the recoil detector is properly calibrated, as the accuracy of the mass calculation depends upon it. Then in Chapter VII we will state how we have corrected or estimated the errors associated with the determination of M_X.

The mass of the forward system, M_X, can be calculated for the reaction $\gamma\ p \rightarrow X\ p$ from the forward mass formula (eqn. 2.2) knowing the angle theta Θ and the four momentum $(E_f, P_f)$of the recoiling proton. We may also obtain information about the recoil detector by selecting events where we completely know the forward system X . We have done this by studying exclusive modes $\gamma p \rightarrow X[p]$, where the system X (= ρ or ρ') consists only of charged pions in the forward spectrometer. The recoil detector has only one detected charged track and it is an identified proton. However, there may be neutrals or undetected charged tracks.

A relatively clean way to look at the recoil detector is to select a sample of events where one can safely assume that the forward system is very well known and the event is energy balanced i.e. contained. Rho's (ρ (770)) lend themselves to such a project very easily as there is a fairly large sample in the Recoil 1 trigger and the signal is very clean. A clean ρ event is defined as having only two charged tracks in the forward system and only one recoil proton in the recoil detector.

One method of checking the calibration of the recoil detector is by plotting the difference of the square of the mass (ΔM^2) of X as obtained from the forward system, minus the mass calculated using the recoil proton variables. If the system is well contained i.e. no particles have been missed, then the difference ΔM^2 should be centered on zero. However, we observe a deviation from zero, and this chapter deals with the steps we have taken to centre the mass difference. The following cuts have been enforced to obtain a clean ρ sample for the interaction $\gamma p \rightarrow \rho\ p$.

1.) There is only one charged track in the recoil detector and it is clearly identified as a proton.

2.) There must be no energy deposit reported in the SLIC or the hadrometer, to eliminate any π^0 decay modes.

3.) The energy difference between the forward and recoiling system with the incident photon and target proton must be less than a low factor i.e. ($E_\gamma + m_p \approx E_f + E_X$ within resolution). This is chosen to be .3 E_γ.

4.) There are only two charged tracks of opposite sign in the forward dectector.

At this point there exists a system $\gamma\ p \rightarrow [p] + X$ where [p] refers to the proton and any associated neutral tracks in the recoil detector.

Let M_F denote the invariant mass of the forward system, as opposed to M_X, which will refer to the mass of the forward system calculated from the recoil proton variables.

In order to have candidates for $\gamma\ p \rightarrow p\ \rho$ (ρ=Rho),further cuts are imposed.

5.) The two tracks are given pion masses and the mass of this two pronged system ($M_\rho = M_F$ here) is required to be less than 1.2 GeV/c^2.

6.) The Θ of the recoil proton from data minus that predicted from the forward system from eqn.(6.1) is shown for the $\pi^+\pi^-$ system in fig. 6.1. The difference is demanded to be within ±.1 radian.

7.) The transverse momentum of the recoil proton balances that of the two pion system within 20 MeV/c. The difference in the transverse momentum is shown in fig. 6.2 .

8.) The azimuthal angle phi of the recoil proton balances the phi of the Rho candidate to within .25 radian. The difference in the phi angles of the Rho candidate and the proton is shown in fig. 6.3.

The invariant mass of the clean two track system ater cuts 1-8 is shown in fig. 6.4 for recoil 1 events - most of the enhancement in the .8 GeV/c region is mostly due to the sample.

We now have a relatively clean Rho ( ) sample. The corrections applied to centre the mass square difference are as follows:

a.) The difference M partly due to improper calibration in the position of the central PWC of the recoil detector, and shows up as an offset in the angle difference between the off-line reported value, and the value predicted from the clean forward system. The predicted value of theta can be written as:

$$\cos \quad (\text{predicted}) = \frac{M \quad - 2\,(m_p + E\ )(m_p - E\ )}{2\,E\ \ P_f} \tag{6.1}$$

where P = four momentum of the photon

P = four momentum of the two pion ( ) system

M = invariant mass of the two forward tracks.

An adjustment (= +.0022 radian) in the obtained from off-line analysis centers the offset in the angle difference .

The correction in translates into a shift = z (obtained from simple geometry) of the central PWC. This must be a constant, and hence, in the analysis, the correction to the angle is done in terms of the z obtained from the Rho study.

b.) The mass square offset is also due to an error in the kinetic energy measurement of the recoil proton. A calculation is performed to evaluate the kinetic energy predicted for the proton, again using only the known clean forward system. It can be recalled that

$$t = (P_i - P_f)^2 = (P_\gamma - P_\rho)^2$$

The left hand side we have already reduced in eqn (2.1) in terms of E_f, where E_f is the energy of the recoiling system. Substituting $E_f = E_{K.E} + M_p$, we can write the kinetic energy calculated from the forward system as :

$$E_{K.E.} \text{ (calculated)} = \frac{2\, E_\gamma\, (E_\rho + P_z) - M_\rho^2}{2\, m_p} \qquad (6.2)$$

where P_z is the z momentum component of the Rho candidate, and E_ρ is its energy.

A 6% correction to the kinetic energy of the recoil proton and the above mentioned theta correction centers the mass square difference very well, as shown in fig. 6.6a . Fig. 6.6b shows this difference for the subsample when there are no neutrals in the recoil detector.

As a separate check on the ΔM^2, a sample of four pronged events are selected - two of positive charge and two of negative charge. These are given pion masses and again, we demand that these be the only tracks in the forward system and the recoil system be energy balanced. This leads to fig. 6.5 , where we observe an enhancement in the 1.6 GeV/c^2 region, some fraction of which are presumably ρ' (1600) candidates. The number of entries in the ρ' plot is less than the Rho by nearly a factor of 10.

The mass squared difference for the ρ' is shown in figs. 6.7a and 6.7b (no neutrals in the recoil detector) . The agreement is again very good, within statistics, for the corrections in K.E. and Θ mentioned.

Hence these corrections to the recoil proton variables are used in all subsequent analysis. The corrected forward mass for all recoil 2 and 3 events is shown in fig. 6.8 .

CHAPTER VII

STUDY OF BIASES IN THE MASS CALCULATION

We now investigate the sources of biases in the mass calculation from the recoil variables.

a.) Some fraction of the events are such that the recoiling proton does not have enough kinetic energy to enter or be detected by the recoil detector. But a proton from a secondary interaction in the target may be within the right acceptance criteria and hence is labelled as a primary recoiling proton, provided that the mass calculated using this proton passes the trigger requirements. The wrong vertex will give rise to a miscalculated mass.

A simple way to estimate the magnitude of this effect is to find the fraction of events that have only two identified recoil proton tracks versus only one charged recoiling proton. This fraction is .032 for our data sample. The case of the single detected proton has to be further corrected as the efficiency for a proton to enter the detector (from kinetic energy limitations) is only .8 (e^{-bt}=.8). Hence, .032 is modified to .032 + .032 x .2 = .038. Thus, we estimate our bias for selecting a recoiling proton that is actually from a secondary interaction to be ≈ 4%.

with and without neutrals in the recoil detector. Fig 7.1b shows the same for a clean ρ sample i.e. the sample A. We show that we are only reducing the event sample. Subtracting fig. 7.1b from fig. 7.1a leaves us with events where the recoil proton does not balance the transverse momentum or the azimuthal angle of the forward ρ system i.e sample B. This is shown in fig. 7.1c . Thus, fig. 7.1c shows that the fraction of miscalculated events in the high mass tail (> 1.8 GeV/c^2) decreases by ≈ 62%, whereas the signal decreases by ≈ 50 %. This seems to imply that demanding NRCLNU be zero i.e. no neutrals in the recoil detector, does not seem to be very advantageous i.e. there seems to be background noise triggering the neutral flag a large fraction of the time. We will confirm this from the Vee data as we present the number of Vees per hadronic event with and without neutrals.

We can use the following table to draw some conclusions:

Table 7.1

	NRCLNU=all	NRCLNU = 0	NRCLNU ≠ 0
N	1113	582	531
A	788	437	351
B	325	145	180

1.) For the subsample A, 44% (= 351/788) have the recoil neutral flag (NRCLNU) on, even though the event is contained.

2.) If the ρ is produced with a P* , then 34% (=180/531) are recognised by the NRCLNU ≠ 0 cut.

3.) For the sample A, 71 % (=788/1113) look like ρ P events, and 29% look like ρ production along with a P*.

We may try the same type of analysis for the " ρ' " system.

Table 7.2

	NRCLNU=all	NRCLNU = 0	NRCLNU ≠ 0
N'	167	83	85
A'	100	56	44
B'	67	26	41

1.) The loss of real signal in a well contained event with the NRCLNU=0 cut is ≈ 44% (= 44/100) , as in the ρ events.

2.) Also, 60% (=100/167) of the clean ρ' events of the A' are labelled as clean events, as opposed to 71% (=788/1113) from the ρ sample.

The statistical errors associated with these numbers are also large, but the ρ and ρ' seem to behave similarly.

We will further estimate the contamination in each mass bin by Monte Carlo techniques.

Referring once more to our ρ analysis, let us select the events that are only balanced in energy, and not in Φ, Θ, or P_t, as in the data analysis we will not be dealing with perfectly balanced events. Also, we demand that the invariant mass of the forward system be within 0 ‑ 2 GeV/c^2.The mapping of these events into the recoil mass calculated by the recoil proton variables (M_x) in 2 GeV/c^2 bins is as follows:

Table 7.3

GeV/c^2 ->	0-2	2-4	4-6	6-8	8-10	10-12
NRCLNU = all	84%	6 %	5 %	3 %	1%	1%
NRCLNU = 0	87%	6 %	3 %	2 %	1%	1%

This shows us that 84% of the events in the 0-2 GeV/c^2 range lie in the 0-2 GeV/c^2 range of the calculated mass M_x. We use this information in the Monte Carlo procedure.

We have simulated the recoil detector with a very simple Monte Carlo procedure. The γ p interaction is allowed to proceed via p X for 70% of the events, and via P* X for the remainder, as this is the approximate rate observed in the ρ analysis. The P* itself was allowed to decay into the two predominant neutral decay modes in the fraction[23] p π^0 (= 60%) and p π^0 π^0 (= 40%).

The mass distribution is flat in M_x^2 and ranges from 0 to 10 GeV/c^2. The slope of the t distribution is -3.5. Geometrical cuts are imposed on the recoil proton to simulate the boundaries of the detector and the same kinetic energy requirements described in Chapter V are enforced here also. The recoil scintillator is treated as a solid cylinder surrounding the interaction point. The π^0's immediately decay into two photons, and each photon is tested for conversion to an e^+e^- pair inside the scintillator. If the electron (or positron) has sufficient path length in the scintillator to deposit detectable energy, then it is labelled as a neutral, and the event is rejected.

Finally, we are in a position to compare the results of this Monte Carlo to that of the ρ study. If the Monte Carlo simulation is in close approximation to the effects of the real detector, then we should be able to reproduce the results of the 0-2 GeV/c^2 range in table 7.3, and then obtain the effects of the P* contamination in the more interesting higher mass bins.

Let us arbitrarily divide the mass range into 2 GeV/c^2 bins.

Therefore, let x=1 => range of 0-2 GeV/c^2
2 => range of 2-4 "
3 => range of 4-6 "
4 => range of 6-8 "
5 => range of 8-10 "

Let M_{xo} = the number of events observed in each x bin

and M_{xr} = the number of events generated (i.e. real) in bin x.

From the results of the Monte Carlo studies, we can construct a matrix correlating the generated events with the observed events as follows:

$M_{1o} = .87\ M_{1r}$

$M_{2o} = .89\ M_{2r} + .02\ M_{1r}$

$M_{3o} = .93\ M_{3r} + .03\ M_{2r} + .03\ M_{1r}$

$M_{4o} = .97\ M_{4r} + .04\ M_{3r} + .04\ M_{2r} + .04 M_{1r}$

$M_{5o} = .99\ M_{5r} + .03\ M_{4r} + .025 M_{3r} + .025 M_{2r} + .03\ M_{1r}$

This matrix can be used to estimate the contamination from lower masses into each higher mass range.

Let us take the total hadronic events and the total efficiency corrected K_s^0 events per 2 GeV/c^2 mass separation in the data. We can now estimate the "real" spectrum from the observed spectrum. We do so by approximating the M_{1o} as 2- 4 GeV, and carrying out the matrix calculation from there.

This yields the following table:

		Mx 2 -4	4 - 6	6 - 8	8 - 10
K_s^0	Observed	23274	31452	34940	20933
	"Real"	26751	34737	35586	17577
All	Observed	376222	394249	373324	212406
	"Real"	432439	433258	373498	167484

However we are interested in the ratio R of the number of K_s^0's per hadronic event observed versus the true ratio.

	Mx 2 - 4	4 - 6	6 - 8	8 - 10
R(Observed)	.062	.079	.094	.098
R ("Real")	.062	.080	.095	.104

Thus we conclude, from this method, that in the highest mass bin used 8-10 Gev/c^2 in the data analysis, the error in the ratio is 6%.

CHAPTER VIII

DATA ANALYSIS AND RESULTS

Event Selection

This chapter deals with the final event selection, and the results obtained from the data.

The following cuts are used to extract the events analysed:

1.) We demand that the trigger be an event trigger and Recoil 2 or 3 (as defined in chapter III), to obtain diffractive events in the forward mass range of 2-11 GeV/c^2. The number of hadronic events we have is 3.47×10^6.

2.) The number of charged particles detected in the recoil detector is required to be one, and this track has to be consistent with being a proton, or likely to be a proton. This cut reduces the sample to 1.47×10^6.

3.) The kinetic energy and angle of the proton is corrected for the calibration error discussed in Chapter VI.

4.) The mass of the K_s^0, Λ or $\bar{\Lambda}$ candidate is obtained from all two track combinations of oppositely charged tracks.

The cuts on the forward system are dependent on the quality of tracks. It was observed that the resolution of K_s^0, lambdas, and antilambdas is worse if both tracks are category 3 (i.e. D1-D2 only) than if they are both category 15 (i.e. D1-D2-D3-D4). Since

resolution is not of prime concern for this part of the analysis, tracks of all categories are kept. The number of K_s^0's, lambdas or antilambdas for a particular inclusive variable is obtained by a fit to a second order polynomial plus a Gaussian centered on the mass of the Vee.

5.) A joint Cherenkov probability is formed (as has been discussed in Chapter V) for the two tracks in the Vee, and the probability is required to be greater than .1 for the K_s^0 candidate, and .12 for the lambda or antilambda candidate. Plots are shown in figs. 5.13, 5.14, 5.15 for the comparison of the Monte Carlo predictions and the background subtracted data for the joint probability of K_s^0, lambdas, and antilambdas.

The Vees are corrected for branching fractions to the observed charged mode. The branching ratio[23] is .686 for $K_s^0 \rightarrow \pi^+ \pi^-$, and .642 for $\Lambda \rightarrow p \pi^-$.

The cross section (σ) of any process can be written in terms of the luminosity (L) and the number of events (N) in the process. The luminosity is defined as the the product of the number of incident photons and the number of scattering centers in the hydrogen target. We can write :

$$\sigma = N/L$$

The luminosity for the data sample we have used for the present analysis is 421 inverse nanobarns. The number N is obtained from the number N_{obs} observed in the particular channel for a certain inclusive variable. This $N_{obs} \pm \Delta N_{obs}$ is obtained from the fit mentioned earlier, and then corrected for the detection efficiency and the efficiency of the fitting curve. Let ε_{det} be the total efficiency for obtaining N events for a particular variable (recall the efficiency determination from chapter V). This is the correction we have to use for each event bin by bin for each variable under consideration.

$$\text{Then, } N \pm \Delta N = \frac{N_{obs} \pm \Delta N_{obs}}{\varepsilon_{det} \pm \Delta\varepsilon_{det}}$$

The other inefficiency one has to consider is that of the trigger Recoil 2 + 3. Below is a list of the factors that contribute to the overall inefficiency of this trigger:

1.) Efficiency of the TAG•H trigger	.95 ± .01
2.) PWC efficiency	.76 ± .02
3.) ϕ angular acceptance in the recoil detector	.92 ± .01
4.) Efficiency for off-line end-end-timing	.98 ± .05
5.) Efficiency of the neutral veto	.74 ± .05
6.) Efficiency for the recoiling proton to enter the recoil detector	.84 ± .01
7.) Θ acceptance	.87 ± .03
8.) Efficiency for reconstruction of the kinetic energy of the recoil proton	.76 ± .04
9.) Efficiency of the trigger processor	.46 ± .03

Hence, the total efficiency associated with the trigger ε_{trig} is .11 ± .01 .

The cross section in its final form in terms of the available numbers (disregarding systematic errors) is

$$\sigma = \frac{N_{obs} \pm \Delta N_{obs}}{L \times (\epsilon_{det} \pm \Delta\epsilon_{det}) \times (\epsilon_{trig} \pm \Delta\epsilon_{trig})}$$

We shall deal with each inclusive variable separately and draw conclusions.

It is pointed out that any cross sections we quote are for the type $\gamma\ p \rightarrow p\ X$, i.e. a diffractive dissociation process with a recoil proton being observed. Hence, comparison with other experiments must be made keeping this in mind.

Data on inclusive distributions

A.) Yield of neutral strange particles per hadronic event as a function of the available energy

The energy available for the production of secondary particles can be written in terms of the centre-of-mass energy, from which the mass of the incident particles are subtracted e.g. for our experiment

$E_{avail} = \sqrt{s} - m_p$, m_p being the mass of the proton.

This quantity is convenient for comparison with other experiments, and the number of Vees per event normalised to the total hadronic rate is shown in table 8.1

$$\text{Define N1(2 or 3)} = \frac{\text{Number of } K^0 \text{ (} \Lambda \text{ or } \bar{\Lambda} \text{)}}{\text{Number of hadronic events}} \text{ per } E_{avail} \text{ bin.}$$

Table 8.1

E(avail) GeV	N1	N2	N3
8 - 10	.13 ± .02	.009 ± .002	.008 ± .003
10 - 12	.15 ± .02	.012 ± .002	.010 ± .001
12 - 14	.16 ± .02	.013 ± .001	.012 ± .002
14 - 16	.19 ± .02	.024 ± .003	.017 ± .002

These numbers are plotted in figure 8.1a. Also shown in figs. 8.1b (K_s^0's) and 8.1c (for lambdas and antilambdas) are data from other hadro and photoproduction experiments. What is evident is that the inclusive cross section is definitely similar to hadroproduction experiments[25-29] implying that the photon is behaving partly as a meson. Note that this is consistent with the results of a lower energy photoproduction[24]. The e^+e^- data [29-32] is also plotted, and the discrepency indicates that this variable is not appropriate for comparison with hadroproduction or photo-production experiments where there is a recoiling system. As we show in the next section, in the proper energy variable, this discrepancy is greatly reduced. This is partly due to the charge coupling of the photon to the strange quarks (recall the photon couples to u : s in the ratio of 4 : 1) . From the predictions of the Lund model[14] of the hadronisation process, the production of the strange quark from the sea is supressed by 60% compared to the lighter quarks. The observed spectra of the strange particles should be a combined effect. We observe a supression of the kaon relative to the pion of nearly a factor of 10.

The difference in the yields of neutral strange mesons and baryons indicates the relative probability of coupling to a single quark versus the coupling to another diquark. The Lund model also predicts the probability of diquark to quark production to be .065 from fits to e^+e^- and proton-antiproton data. In the E_{avail} range of 10 - 12 GeV, we see that the ratio of lambda to kaon is .07, in good agreement with the model.

B.) Yield of neutral strange particles per hadronic event as a function of the forward mass

From the overall centre-of-mass frame, we can now look at the yield per hadronic event of the Vees in the P γ process, obtained from the factorisation of the γ p process. Recall that P is the exchange system mediating the interaction between the photon and the proton. The interaction here is similar to the e^+e^- experiments except that the quark-antiquark pair from the real photon has a coupling to the proton also. If we take vector meson dominance to be an adequate model for the hadronisation of the real photons, we may expect the strangeness content of the two interactions to be different. Hence, it is interesting to compare the two processes or production of particles by real and virtual photons.

We look at the cleanest sample of events we can obtain (in terms of the recoil detector) by requiring that there be no neutrals (NRCLNU=0) detected in the recoil system. We obtain the corrected number of neutral kaons, lambdas, and antilambdas per hadronic event as a function of the forward mass with no neutrals in the recoil detector. We present our result in table 8.2 and fig. 8.2 . We show as well data from e^+e^- annihilation. The agreement is very good, within the large errors in the e^+e^- data.

If scaling or factorisation is valid, then the relevant energy scale in the γ P system should be the forward mass and not the incident photon energy. We investigate this effect by dividing our photon energy into three regions : 40 - 75, 75 - 110, and 110 - 170 GeV.

The fractional yield (i.e the number of Vees per hadronic event) surviving in the case when there are no detected neutrals in the recoil detector(NRCLNU = 0) is 33% of those when no demands are made on the number of neutrals (NRCLNU = all). We estimated in Chapter VI the fractional contamination in the higher mass bins from the spillover of the lower mass bins. We show here that the number of neutral kaons, lambdas, and antilambdas per hadronic event is independant of whether NRCLNU = 0 or all. This will allow us to use a larger sample of events. The yield when there are no restrictions on the number of neutrals in the recoil detector is shown in fig. 8.3 . Table 8.2 shows the comparison for each forward mass region. From fig. 8.2 and fig. 8.3 we see that the agreement between NRCLNU = 0 and NRCLNU = all is very good, again within statistics.

Let us define the yield per hadronic event as:

$$\mathrm{R1(\ 2\ or\ 3)} = \frac{\text{Number of } K_S{}^0 \ (\ \Lambda \text{ or } \bar{\Lambda}\ )}{\text{Number of hadronic events}}$$

Table 8.2

$2 < M_X < 4$ GeV/c^2

	R1	R2	R3
NRCLNU = all	.12 ± .01	-	-
NRCLNU = 0	.13 ± .02	-	-

$4 < M_X < 6$ GeV/c^2

	R1	R2	R3
NRCLNU = all	.16 ± .02	.013 ± .002	.011 ± .001
NRCLNU = 0	.16 ± .02	.011 ± .002	.009 ± .002

$6 < M_X < 8$ GeV/c^2

	R1	R2	R3
NRCLNU = all	.18 ± .02	.016 ± .002	.015 ± .002
NRCLNU = 0	.19 ± .02	.016 ± .002	.018 ± .005

$8 < M_X < 10$ GeV/c^2

	R1	R2	R3
NRCLNU = all	.24 ± .03	.018 ± .002	.018 ± .003
NRCLNU = 0	.21 ± .03	.025 ± .009	.020 ± .005

Having demonstrated that the yield in the enhanced sample shows little contamination in the energy bins (M_X ranging from 2 - 10 GeV/c^2) we are concerned with, we proceed to investigate the energy dependence of the ratio R (the number of Vees per hadronic event) for NRCLNU = all. Below in table 8.3 we tabulate the results.

Table 8.3

$2 < M_X < 4$ Gev/c^2

E(γ) GeV	R1	R2	R3
40< E(γ) < 75	.13 ± .01	.007 ± .003	-
75< E(γ) <110	.13 ± .01	.008 ± .004	-
110<E(γ) <170	.12 ± .01		

$4 < M_X < 6$ GeV/c^2

E(γ) GeV	R1	R2	R3
40< E(γ) < 75	.14 ± .01	.013 ± .003	.014 ± .004
75< E(γ) <110	.16 ± .01	.015 ± .002	.012 ± .002
110<E(γ) <170	.16 ± .01	.016 ± .004	.012 ± .003

$6 < M_X < 8$ GeV/c^2

E(γ) GeV	R1	R2	R3
40< E(γ) < 75	.17 ± .02	.020 ± .001	.013 + .004
75< E(γ) <110	.2 ± .01	.011 ± .002	.012 ± .002
110<E(γ) <170	.17 ± .01	.019 ± .003	.018 ± .003

$8 < M_X < 10$ GeV/c^2

$E(\gamma)$ GeV	R1	R2	R3
$40 < E(\gamma) < 75$	-	-	-
$75 < E(\gamma) < 110$	.23 ± .02	.016 ± .003	.014 ± .004
$110 < E(\gamma) < 170$	.19 ± .01	.021 ± .004	.019 + .004

We show the number of K_S^0 per event per energy division in fig. 8.4, lambdas in fig. 8.5, and antilambdas in fig. 8.6 . Table 8.3 shows that, within errors, the number of Vees per event depends only on the invariant mass of the γ p system (which is a measure of the energy available for the production of particles) and not on the incident photon energy. The similarity of the yield of lambdas and antilambdas indicates we have selected events from a dissociation process. We have thus shown that scaling or factorisation holds in a diffractive dissociation process.

C.) The differential cross section of neutral kaons, lambdas, and antilambdas as a function of its fractional energy in the laboratory.

The fractional energy carried by the particle with respect to the incident photon energy is denoted by Z where

$$Z = E_{Vee}/E_{\gamma}$$

The differential cross section of the Vees in the Z variable is tabulated in table 8.4 . We plot $d\sigma/dZ$ distribution of the K_S^0 , Λ, $\bar{\Lambda}$ (anti Λ) in fig 8.7 . The neutral kaon distribution peaks at .15, similar to the lambdas. Note again that the lambda and the antilambda cross sections are very similar.

Table 8.4

Z	Ks^0 (μb)	Λ (μb)	Anti Λ (μb)
.025 - .05	54.1 ± 8.8		
.05 - .1	23.7 ± 3.5	1.46 ± .27	1.71 ± .38
.1 - .2	12.8 ± 1.9	1.23 ± .15	1.17 ± .14
.2 - .3	6.7 ± 1.0	.78 ± .10	.65 ± .09
.3 - .4	3.0 ± .5	.52 ± .07	.43 ± .07
.4 - .55	2.0 ± .4	.18 ± .03	.14 ± .03
.55 - .7	.6 ± .2	.04 ± .03	.075±.074

D.) The differential cross-section of neutral kaons, lambdas, and antilambdas as a function of Feynman X in the overall centre-of-mass.

The Feynman X in the overall centre-of-mass is defined as

$X_{of} = 2 P_\parallel/\sqrt{s}$,

where $\sqrt{s}$ is the centre-of-mass energy

$P_\parallel$ is the momentum of the particle parallel to the photon - proton axis in the overall frame.

We tabulate the differential cross section for the production of the Vee in the overall centre of mass in table 8.5 .

Table 8.5

$d\sigma / dX_{of}$	Ks^0 μb	Λ μb	Anti Λ μb
-.05 - +.05	6.3 ± .9	.78 ± .12	.75 ± .12
+.05 - +.1	14.4 ± 2.1	.85 ± .13	1.01 ± .16
+.1 - +.15	11.9 ± 2.9	1.01± .14	1.06 ± .15
+.15 - +.2	9.2 ± 1.4	.85 ± .12	.72 ± .09
+.2 - +.3	4.3 ± .6	.57 ± .08	.67 ± .11
+.3 - +.35	3.2 ± .6	.57 ± .09	.37 ± .07
+.35 - +.45	1.9 ± .3	.30 ± .06	.24 ± .07
+.45 - +.6	1.2 ± .2	.11 ± .06	.23 ± .04
+.6 - +.9	.3 ± .1	.08 ± .02	.05 ± .03

We show the behaviour of the differential cross section for the neutral kaons, lambdas, and antilambdas in figs. 8.8, 8.9, 8.10 respectively. It is worth noting that, again, the lambda and the antilambda follow each other closely, within error bars, indicative of a dissociation process: i.e., the strange baryons and antibaryons have the same production mechanism and are produced with equal probability.

Now we make the comparison of the scaled cross section $X_{of} d\sigma/dX_{of}$ to the counting rules of Chapter I in the region of X_{of} greater than .3 . The plots of $X_{of} d\sigma/dX_{of}$ and the fit of the form $A(1-X_{of})^D$ are shown in figs 8.11 (pion), 8.12 (K_s^0)

8.13 (lambda) and 8.14 (antilambda) . Below, we tabulate the value of D obtained from the fit, and compare to the predictions mentioned in chapter I.

Table 8.6

	+ X	D (data)	χ^2/d.o.f.	D^1	D^2
Ks^0	.3 - .9	1.5 ± .4	.25	1	0
Λ	.3 .7	2.0 ± .5	.72	2	1
Anti Λ	.3 .7	2.7 ± .8	.46	2	1

D^1 refers to the counting rule prediction of the fragmentation model of Gunion[6].

D^2 refers to the counting rule prediction from the photon-gluon fusion model[12].

In fig. 8.15, we also plot the ratio of baryons to mesons in terms of the Feynman X_f in the overall centre-of-mass.

As can be seen, the results agree well with the fragmentation model of Gunion but disagree with the photon gluon fusion model. Nevertheless, since the fit is not completely in the large X_f region, the results are not conclusive. Our results (at mean photon energy of 107 GeV) are very similar with that of another photoproduction experiment[24] at 20 GeV photon energy. The counting rules make no assumption on the valence quark flavour, and hence the prediction for the strange meson K_s^0 and the non-strange meson π^+ are the same i.e. D = 1. We show both the

A fit of the form A $(1-X_{ff})^D$ to X_{ff} $d\sigma/dX_{ff}$ for K_s^0s in the region of Feynman X_f greater than .3 is shown in fig. 8.19, and for X_f less than ⁻.3 in fig. 8.20 . The same for the sum of lambdas and antilambdas is shown in fig. 8.21 and fig. 8.22 respectively. The values of D and A in the + X_{ff} and $-X_{ff}$ regions are shown in tables 8.8 and 8.9 respectively :

Table 8.8

	+ X	D (Data)	χ^2/D.O.F	D1	D3
Ks	+.7 -> +.3	1.78 ± .34	.92	1	0
Λ+Anti Λ	+.7 -> +.3	3.04 ± .87	.1	2	1

Table 8.9

	- X	D (Data)	χ^2/D.O.F.	D1*	D2*	D3*
Ks ^{0}	-.7 -> -.3	1.04±.55	2.5	1	3	0
Λ+Anti Λ	-.7 -> -.3	1.97±1.06	.5	2	2	1

D1 refers to the photon fragmentation prediction of DeGrand and Randa[11].

D1* refers to the prediction for the two gluon component of the exchange particle[11].

D2* refers to the prediction the three gluon component of the exchange particle.[11]

D3* refers to the photon-gluon fusion prediction [12].

The predictions for the positive Feynman X region should be the same as for the overall frame, because both must reflect photon fragments. Again, the predictions agree fairly well for K_s^0, but it is unclear how well they match for the strange baryon in the positive X_{ff} region. The negative X_{ff} region seems consistent with the two gluon exchange for the K_s^0, but is consistent with either two or three gluon exchange for the lambdas and antilambdas.

F) The slope of the square of the transverse momentum of the neutral kaons, lambdas, and antilambdas as a function of the forward mass.

The square of the transverse momentum of the Vees are plotted in fig 8.23 in terms of the cross section. There is a kink in the P_t^2 distribution for K_s^0 at around .15 Gev^2/c^2. We have fit the P_t^2 distribution for the region greater than .15 .This effect has been observed in other hadroproduction experiments, and is partly due to the K* spectrum, decaying into K_s^0s of lower P_t. Fits to the form $A\ e^{-B\ P_t^2}$ are shown in table 8.10 .

Table 8.10

	A	B	χ^2/D.O.F.
Ks^0	15.8 ± 2.1	3.7±.3	.1
Λ	.9 ± .1	2.2±.2	4.1
Anti Λ	1.0 ± .1	2.8±.3	11

Note that the average transverse momentum increases (i.e. the slope of the transverse momentum decreases) as the mass of the particle type increases. This has been observed in a π^+p experiment[26].

It is interesting to extend the above observation and study the transverse momentum behaviour in terms of the energy in the forward centre of mass i.e. M_x. We subdivide our data in forward mass bins of 2-4, 4-6, 6-8, 8-10 GeV/c^2. Now we look at the slope of the square of the transverse momentum in these different mass bins. The slope should be proportional to the $\langle P_t^2 \rangle$.

Table 8.11 contains the values for the slope b of the fit to the form A $e^{-bP_t^2}$.

Table 8.11

Slope b of $e^{-bP_t^2}$

Mx	Ks	Λ + Anti Λ
2 - 4	4.8 ± .2	2.7 ± .5
4 - 6	4.2 ± .2	2.6 ± .5
6 - 8	4.3 ± .2	2.4 ± .3
8 -10	3.5 ± .2	2.0 ± .5

We see from table 8.11 and figs. 8.24 and 8.25 that the average slope decreases with increase in the forward mass. This may imply that the hardness of the interaction increases with the available energy. It is known from other experiments[26] that the transverse momentum increases as the absolute value of the increasing contribution from hard and soft gluon emission which increases with the energy scale.

Upper limits on Vee decay modes of the charmed baryon Λ_c

We now come to the last section section of this thesis- namely, setting the 90% confidence level upper limit on the decay modes of the charmed baryon Λ_c, in the absence of a signal. The limits set are on the following modes:

$\Lambda_c^+ \rightarrow K_s^0\ p$ Branching fraction = B1 i.)

$\rightarrow \Lambda\ \pi^+$ Branching fraction = B2 ii.)

In order to obtain the efficiency of the decay modes searched for, we generate Monte Carlo events with one negative and one positive Λ_c. The charged multiplicity is balanced with pions such that the average multiplicity (in accordance with KNO distribution) is six, as observed in our data.

We use the following set of cuts to ensure a clean sample of Vees, and less background. Three charged tracks are involved for the modes i) and ii) and background reduction is crucial. These cuts are applied both to the data and the Monte Carlo reconstructed tracks.

1.) There is only one charged track in the recoil detector and it is identified to be a clean proton.

2.) There are no identified neutrals in the recoil detector.

3.) We use only Recoil 2+3 triggers.

4.) We require that the tagging energy be greater than 45 GeV.

5.) The Vees are obtained from the verticising routine that has been discussed in chapter IV, as this ensures a good signal to background ratio. This is especially important for the lamda/antilambda sample to eliminate a large background.

6.) The degrees of freedom of category 3 tracks is required to be greater than 6 - this is an attempt to obtain a sample of tracks with fairly good momentum resolution.

7.) The Vees are required to be within 3σ of the nominal mass. For the $K_s{}^0$s this implies it to be within 21 MeV/c^2 of the nominal mass of .4977 GeV/c^2, and the lambda/antilambda to be within 10 MeV/c^2 of 1.1156 GeV/c^2.

8.) The chi-square contribution of the proton or pion (i.e. the third track of the Λ_c and not part of the Vee) to the primary vertex is required to be small - the Λ_c lifetime is very small and the proton/pion not belonging to the Vee will not be detected as coming from a secondary vertex within the limits of our resolution.

The probability of the event is defined as follows.

PROBEV

= PROBKS * PROBP (for decay mode i.)

= PROBLA * PROBPI (for decay mode ii.)

PROBKS, PROBLA , and PROBP have been defined in Chapter V.

PROBPI is the probability of the non-Vee pion track (let it be j) which is defined as Prob(j,2)+Prob(j,3)

We shall determine the upper limit of the cross section times the branching into a particlular mode with a confidence level of 90% . In addition to the above cuts, we demand the joint probability of the event (PROBEV) be greater than .1,in a manner similar to the Vee study of chapter IV.

Let A be the total number of Λ_c^+ events in the Monte Carlo sample in the decay mode we are studying. We can also obtain an invariant mass distribution of the Vee and the second particle form this reconstructed Monte Carlo sample in exactly the same manner as we do for the data events. Let B be the number obtained from a fit to this mass distribution, using a second order polynomial plus a Gaussian, for all the cuts discussed above. Then the efficiency of detection when requiring that the probability of the event be greater than .1 is given by

$$\varepsilon_{det} = B/A$$

Shown in plot 8.26 is a plot of the Monte Carlo Λ_c^+ for the decay mode into K_s^0 p. Also shown in plot 8.27 is a plot of the Monte Carlo Λ_c^+ for the decay mode into $\Lambda\ \pi^+$.

The fit gives the standard deviation (Δ) of the Gaussian distribution to be $\approx$ 30 MeV/c^2 for the Monte Carlo events shown in fig 8.26. Let there be N1 events within $\pm 2\Delta$ of the nominal mass of the Λ_c^+ at 2.285 GeV/c^2. Let there be N2 events events in the side bands of $\pm 2\Delta$ (i.e. 2Δ on either side). Then, $M = N1 - N2/2$ is the number of events in this 2Δ mass range. Let N be the error on M, obtained by adding in quadrature the errors in N1 and N2/2.

Then, the cross section times branching fraction for the process

$$\begin{array}{lll} \gamma\ p \to \Lambda_c^+\ p\ X & & \\ & \to (K_s^0\ p\ )\ p\ X & \\ \text{or} & \to (\Lambda\ \pi^+\ )\ \ p\ X & \text{is} \end{array}$$

$$\sigma.B = \frac{M + N \times 1.645}{L \times \varepsilon_{trig} \times \varepsilon_{det} \times .957}$$

The factor of .957 enters as the event sample looked at is only within ± 2Δ, and there is a 4.3% probability of having missed some of the signal in the wings. We use the factor of 1.645 because we are measuring the upper limits on the cross-section to 90% confidence level.

The luminosity of this data sample is 476 inverse nanobarns. The efficiency of the Recoil 2 + 3 trigger is .13 - the t slope of the recoil proton for these high mass events is flatter than for normal events, and the correction for the inefficiency arising form this source is smaller.

Let us look at the $\Lambda_c^+ \to K_s^0$ p mode first.

$\sigma.B1(\gamma\ p \to \Lambda_c^+ p\ X\ )$

$\to \overline{K_0}\ p$ (Branching fraction of $\overline{K_0} \to K_s^0$ is .5)

$\to K_s^0$ (B.F. of $K_s^0 \to \pi^+\pi^-$ is .6861)

$\to \pi^+\ \pi^-$

Fig. 8.28 shows the data events with a $(\pi^+\pi^-)$ p combination and the previously described cuts. The number of background subtracted events in ±2Δ of the Λ_c nominal mass is 1038 - (2002/2) = 37. Hence the net error on the 37 events is 45, as explained before.

The efficiency of detection is .086 including the branching fraction, from the Monte Carlo studies. Hence,

$$\sigma.B1 = \frac{37 \pm 45 \times 1.645}{476 \times .133 \times .086 \times .957 \times .5} < 43 \text{ nbarns.}$$

Now let us look at the $\Lambda_c^+ \to \Lambda\pi^+$ mode. Fig. 8.29 shows the $(p\ \pi^-)\ \pi^+$ combination in the data with the above mentioned cuts. The cross section times the branching fraction is :

$\sigma.B2(\ \gamma\ p \to \Lambda_c^+ p\ X\ )$

$\to \Lambda\ \pi^+$ (Branching fraction of $\Lambda \to p\ \pi^-$ is .642)

$\to p\ \pi^-$

The number of background subtracted events within ±2Δ of the nominal Λ_c mass is 199 - (376/2) = 11. The error on 199 events is 14, and the error on 188 events is 13. The error on the number of events in the central 2Δ region is 19.

The efficiency of detection is .081, from the Monte Carlo studies. Hence,

$$\sigma.B2 = \frac{11 \pm 19 \times 1.645}{476 \times .133 \times .081 \times .954} < 9 \text{ nbarns.}$$

This is to be compared with another photoproduction experiment [33] where the observed cross section for the neutral kaon mode is reported to be 3.1 nanobarns and the upper limit on the production cross section (to 90% confidence level) for the $\Lambda\pi^+$ mode is < .9 nanobarns. Two main differences are that ours is a process with a detected recoiling proton and our overall detection efficiency is less.

CONCLUSIONS

To summarise, we have presented inclusive distributions of neutral kaons, lambdas, and antilambdas in a diffractive dissociation process γ p -> X p at mean photon energy of 107 GeV. We have explicitly shown that the rate of neutral strange particle production in the centre-of-mass of X depends only on the energy scale set by the mass of X and not on the energy of the incident photon. This leads us to believe that for diffractive dissociation, our initial process may be factorised into p->p + P, and γ + P-> X, where P is the exchange process responsible for the interaction of the photon and the proton. The close similarity in the number of lambdas and antilambdas reinforces our belief that we have selected a sample of events that are the fragments of the photon. The dependance of the yield of the neutral mesons and baryons as a function of the energy scale set by the mass of X is remarkably similar to the yield from e^+e^- experiments.

We have investigated the regions of large positive and negative Feynman X_f in the rest frame X_f (called the forward centre-of-mass). The region of large positive X_f reflects the fragments of the photon, whereas the region of large negative X_f reflects the fragments of P. Comparisions have been made of predictions from various models with the shape of the Feynman X_f distributions in the P fragmentation region. We have shown that a two gluon component for P is consistent with our K_s^0 data. The prediction for lambdas is the same for both the two gluon and the three gluon component of P , and our data is consistent with both. Data in the photon fragmentation region agree well with counting rule predictions for lambdas, and only moderately for K_s^0's.

We have shown that the average transverse momentum of the neutral kaons in the forward centre-of-mass is greater than that of the heavier lambda and antilambda. The average transverse momentum of each of the neutral strange particles also increases with increasing mass of X, showing increasing contribution of soft and hard gluon emission.

We have extended the measured yield per hadronic event of the neutral strange particles to higher energies than has been measured before. The rate is very similar to pion induced reactions, supporting the hypothesis that the photon behaves primarily as a hadron.

Finally, we have set upper limits to 90% confidence level on the cross section of diffraction production of Λ_c^+ into the decay modes $\overline{K^0}p$ as < 43 nanobarns, and the decay mode $\Lambda\pi^+$ as < 9 nanobarns.

BIBLIOGRAPHY

1.) W. Kittel, "Proceedings of the Europhysics study conference", Erice, Italy (1981).

2.) J.J. Sakurai, " Properties of the fundamental interactions" Vol9, Part A, p243, (1973).

3.) L. Roudeu, " Photoproduction of heavy flavours (Experimental Review)", invited talk at the 1981 E.P.S. Int. Conference on High Energy Physics, Lisbon.

4.) See e.g. "Introduction to high energy physics " by D. Perkins

5.) J. Randa, " Diffraction - What do we know; what can we learn?" in Proceedings of the 11th. international winter meeting on fundamental physics, ed. A. Ferrando, (Instituto de Estudios Nucleares, Madrid, 1983), p 191-237, 1983.

S.F. King, A. Donnachie and J. Randa, " Diffractive photoproduction of quark -antiquark jets ", Nuclear Physics B167, (1980), 98.

6.) R. Blankenbecler and S.J. Brodsky, " Unified description of inclusive and exclusive reactions at all momentum transfers", Physics Review D10, 2973, (1974).

J.F. Gunion, " Quarks and gluons in low P_t physics", SLAC-PUB-2607, (1980).

J.F. Gunion, " Short distance counting rules for low P_t fragmentation", Physics Letters, 88B, (1977), 150.

J.F. Gunion, " Quark-counting hadron-size effects for total cross sections ", Physical Review D15, 2617, (1977).

7.) K. P. Das and R. Hwa, " Quark antiquark recombination in the fragmentation region ", Phys. Letters, 68B,(1977), 459.

8.) Van Chang and Rudulph C. Hwa, " Inclusive distributions of photoproduced pions in QCD and the recombinations model ", Physics Letters, 85B, (1979), 285.

9.) D. Duke and F. Taylor, " Determination of the sea-quark distributions in the proton by the single-particle inclusive reactions", Phys. Rev. D17,(1978).

10.) W. Ochs, " Hadron fragmentation at high energies and quark constitituents", Nuclear Physics B118,(1977), 397.

11.) T.A. DeGrand and J. Randa, " General Features of High Mass Diffraction ", Physics Letters, 110B,484, (1982).

12.) L.M. Jones and H.W. Wyld Jr., " Production of bound quark-antiquark systems ", Physical Review D17, 2332, (1981).

13.) M. Fontannaz, B. Pire, and D. Schiff, " Inclusive Photoproduction cross sections of charmed mesons and baryons," Zeitschrift fur Physik, Particles and Fields, 11, 211-222 (1981).

14.) C. Peterson, " Baryon and charm production in quark jets and hadron-hadron collisions ", Invited Talk given at the XIII International Symposium on Multiparticle Dynamics, Volendum, the Netherlands, 1982.

15.) W. Hofmann and D. Wegener, " Comparitive study of baryon production in hard and soft processes", Zeitschrift fur Physik, Particles and Fields, 21, 387-390, (1984).

16.) A.L. Duncan" Characteristics of hadronic states observed in High Energy Diffractive Photoproduction in Hydrogen", Ph.D. Thesis, University of Colorado, Boulder, 1982 (unpublished).

B.H. Denby, " Inelastic and Elastic Photoproduction of J/ψ (3097)", Ph.D. Thesis, University of California, Santa Barbara, 1983.

D.J. Summers, " A Study of the Decay $D^0 \rightarrow K^-\pi^+\pi^0$ in High Energy Photoproduction ", Ph.D. Thesis, University of California, Santa Barbara, 1984.

17.) G.F. Hartner et al. " A Recoil Proton Detector Using Cylindrical Proportional Cahmbers and Scintillator Counters", Nuclear Instruments and Methods,<u>216</u>, 113. (1983).

18.) R. Yamada et al. " Fermilab Magnet Mapping system ",Nuclear Instruments and Methods, <u>138</u>, 567, (1976).

19.) T. Nash, " A Pedestrians Guide to E-516 Trigger Systems ", E-516 Internal Memo.

20.) J.F. Martin et al., " Use of ECL-CAMAC Trigger Processor System for Recoil Missing Mass Triggers at the Tagged Photon Spectrometer at Fermilab", Proccedings of the Topical Conference on the Applications of Microprocessors to High Energy Physics Experiments", CERN 81-07, 164, (1981).

21.) D. Carey and D. Drijard, " Monte Carlo Phase Spase with Limited Transverse Transverse Momentum, Journal of Computational Physics, 28, 327,(1978).

22.) Z. Koba et al, Nuclear Physics, B40, 317, (1972).

23.) "Review of Particle Properties ", Reviews of Modern Particles, Vol. 56, No 2, Part II, April 1984.

24.) K. Abe et al., " Inclusive of Production of Neutral Strange Particles at 20 GeV", Physical Review D29, 1877, (1984).

25.) P. H. Stuntebeck et al., " Inclusive Production of K_1, Λ^0, and Λ^0 in 18.5 GeV/c $\pi\pm p$ interactions", Physical Review D9, 608, (1974 .

26.) M. Arneodo at al., " Quark-antiquark Fragmentation into Neutral Strange Particles as Observed in Muon-Proton Interactions at 280 GeV", Physics Letters, 145B,(1984), 156.

27.) F. Barreiro et al., " Inclusive Neutral-Strange-Particle Production in $\pi^- p$ interactions at 15 GeV/c", Physical Review D17, 669, (1978).

28.) D. Bogert et al.," Inclusive Production of Neutral Strange Particles in 250-GeV/c π^-p Interactions", Physical Review D16, 2098, (1977).

29.) D. Ljung et al., " π^-p Interactions at 205 GeV/c: Multiplicities of Charged and Neutral Particles; Production of Neutral Particles", Physical Review D15, 3163, (1977).

30.) R. Brandelik et al., " Charged Pion, Kaon, and Nucleon Production by e^+e^- Annihilation for C.M. Energies Between 3.6 and 5.2 GeV", Nuclear Physics B148, 189, (1979)

31.) V. Luth et al., " K^0 Production in e^+e^- Annihilation ", Physics Letters, 70B,(1977), 120.

32.) Ch. Berger et al., " Inclusive K^0 Production in e^+e^- Annihilation for $9.3 < \sqrt{s} < 31.6$ GeV ", Physics Letters,104B, (1981), 79.

33.) J.J. Russell, " Photoproduction of charmed baryons", Ph.D. Thesis, University of Illinois, 1973.

Appendix A

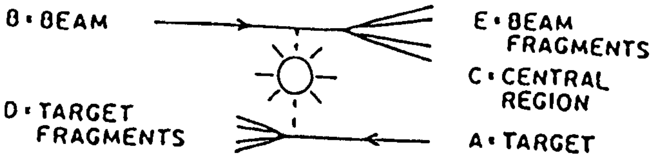

Fig. 1.1 General features of a two-body interaction.

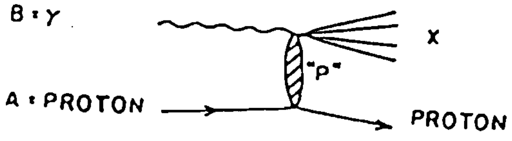

Fig. 1.2 General features of γp interactions.

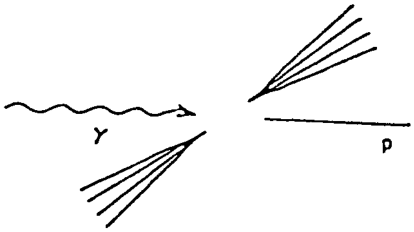

Fig. 1.3 Overall centre of mass.

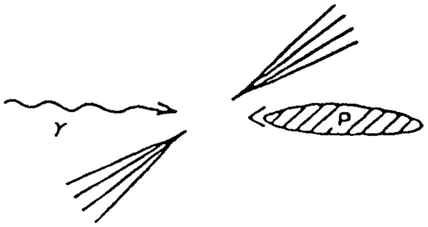

Fig. 1.4 Forward centre of mass.

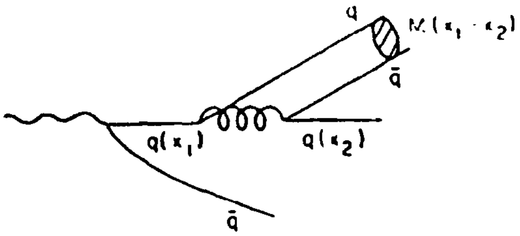

Fig. 1.5 Meson production from quark fragmentation.

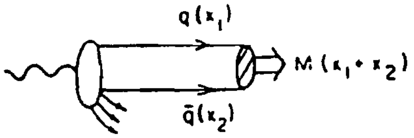

Fig. 1.6 Meson production from quark recombination.

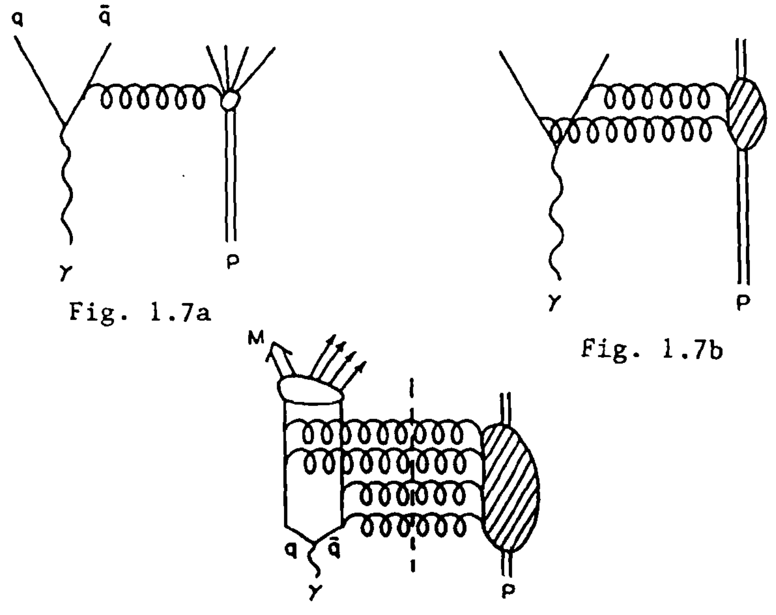

Fig. 1.7a

Fig. 1.7b

Fig. 1.7c

Fig. 1.7 Feynman diagrams for photon-proton interactions

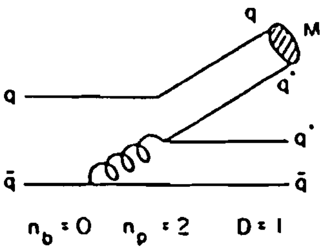

Fig. 1.8a

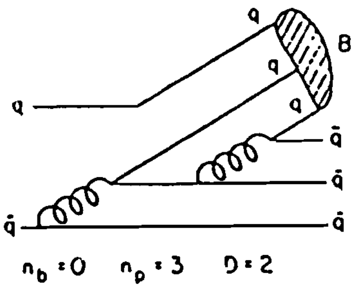

Fig. 1.8b

Fig. 1.8 Meson and baryon production at + X_{of} .

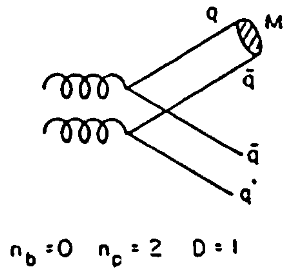

Fig. 1.9a

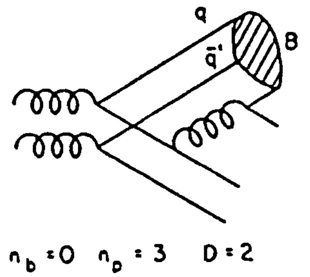

Fig. 1.9b

Fig. 1.9 Meson and baryon production for 2 gluon exchange.

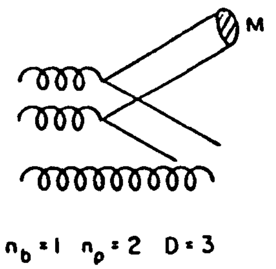

Fig. 1.10a

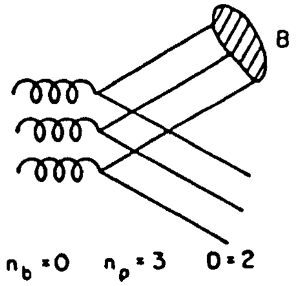

Fig. 1.10b

Fig. 1.10 Meson and baryon production for 3 gluon exchange.

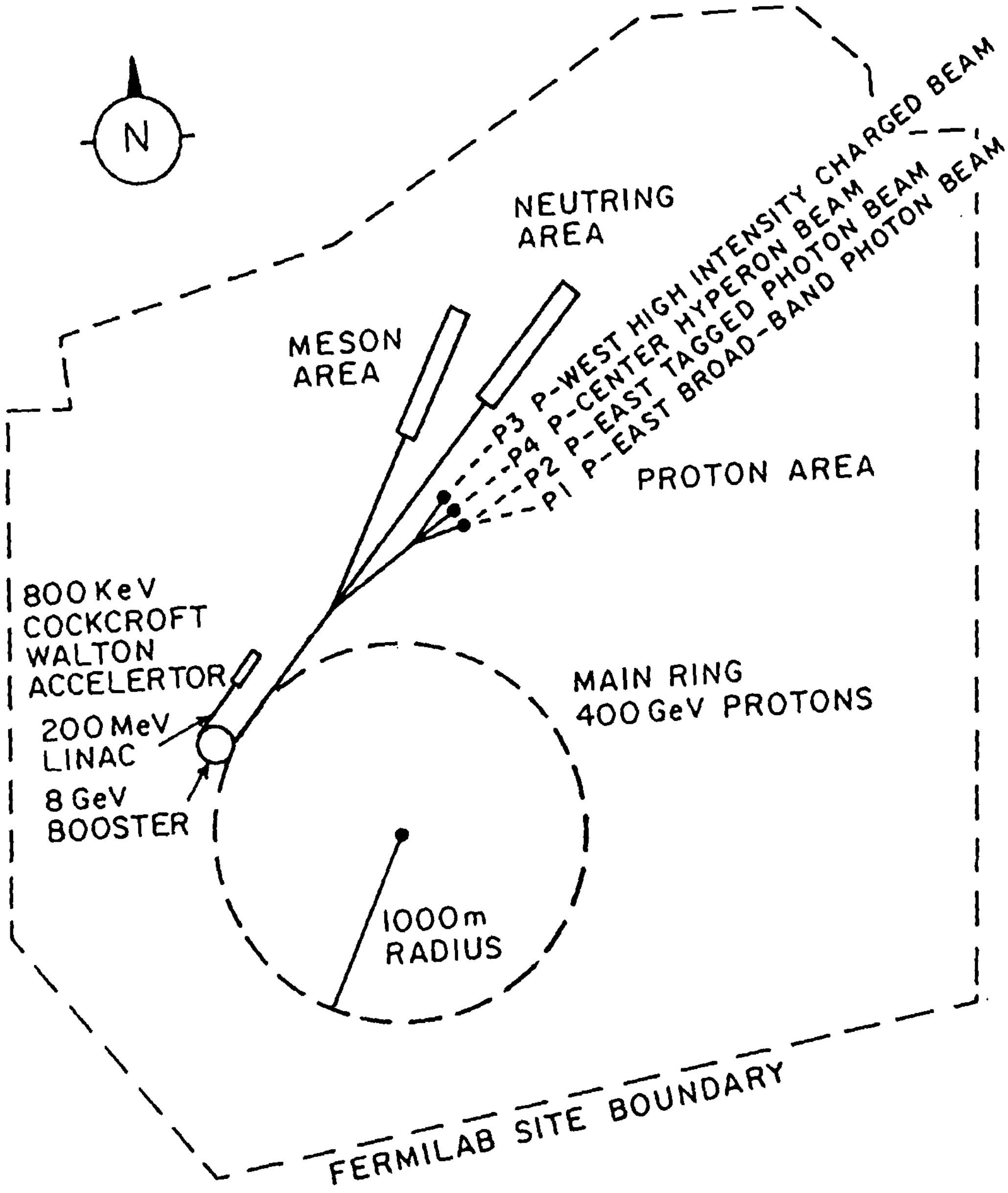

Fig. 2.1 Fermilab beam lines

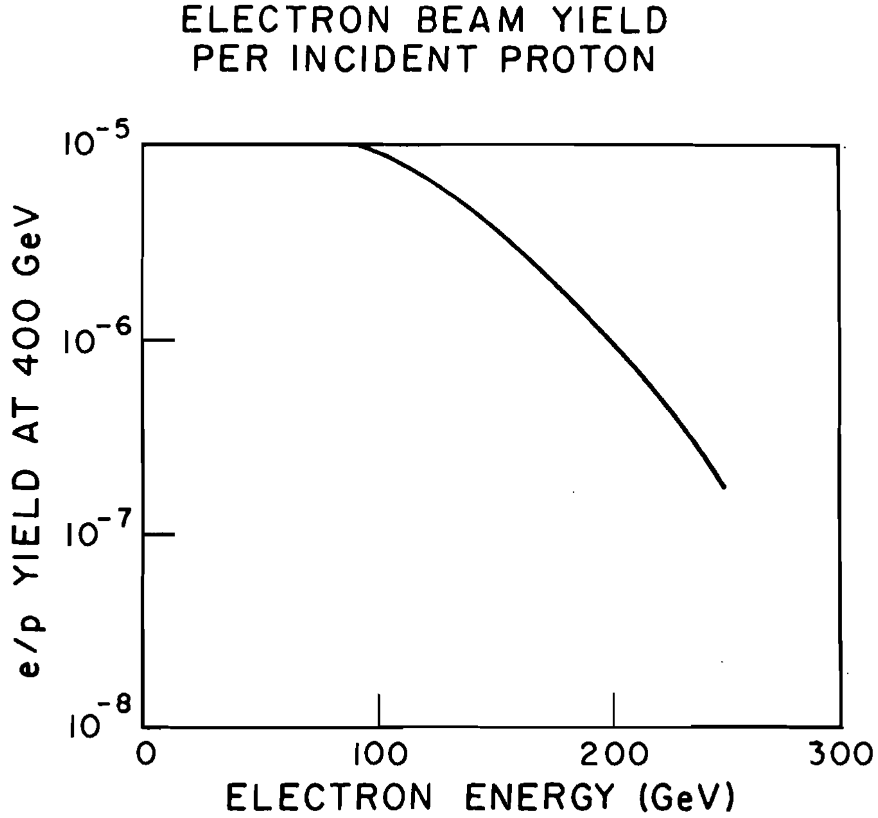

Fig. 2.2 Electron beam yield per incident proton as a function of the electron energy

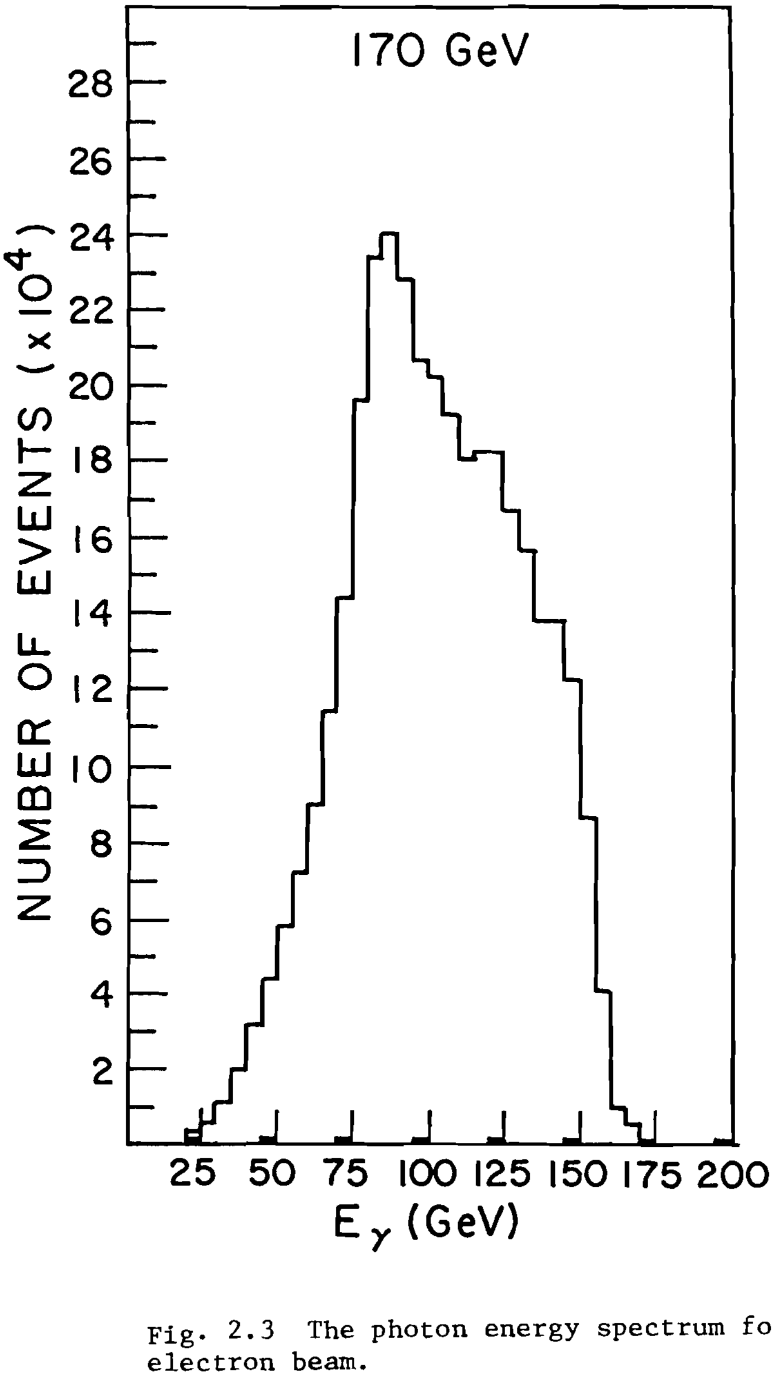

Fig. 2.3 The photon energy spectrum for 170 GeV electron beam.

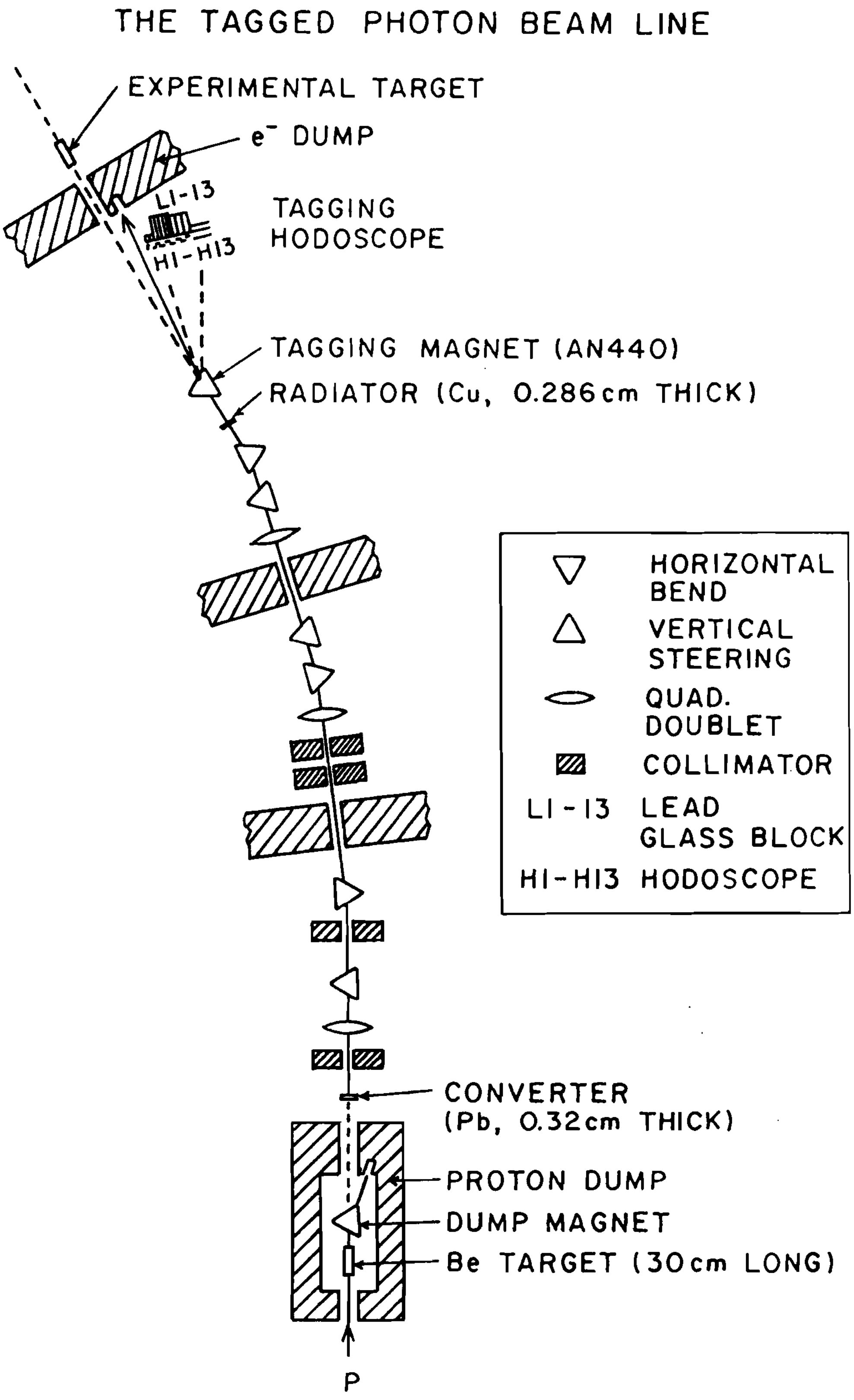

Figure 2.4 The tagged photon beam line.

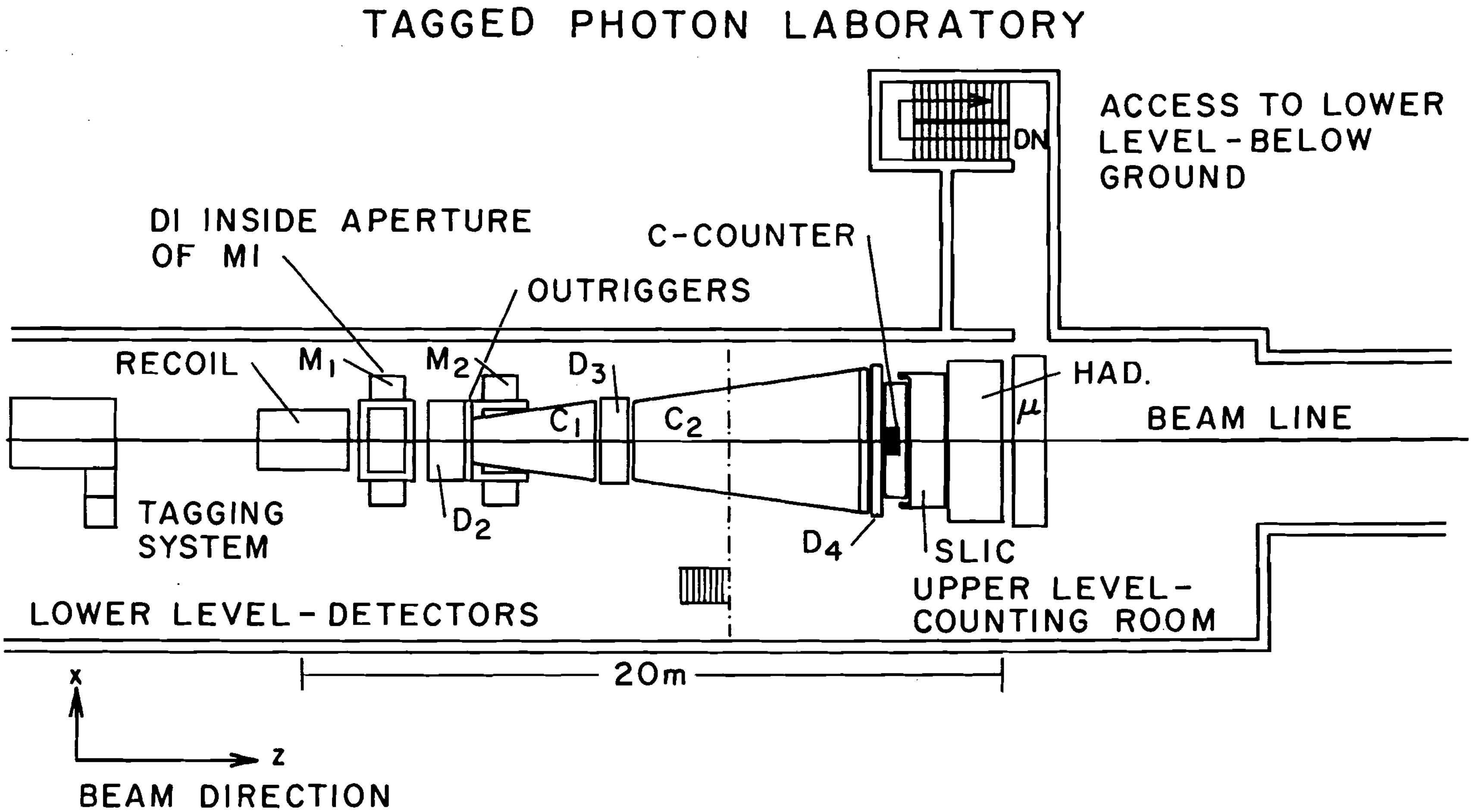

Figure 2.5 Layout of the tagged photon laboratory.

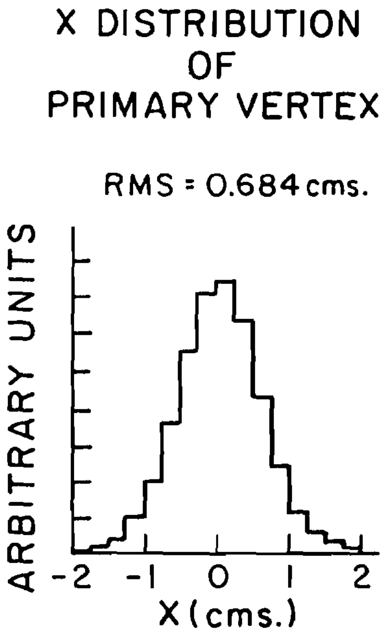

Figure 2.6

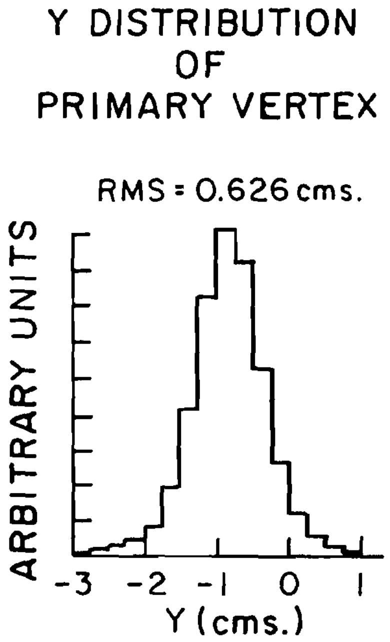

Figure 2.7

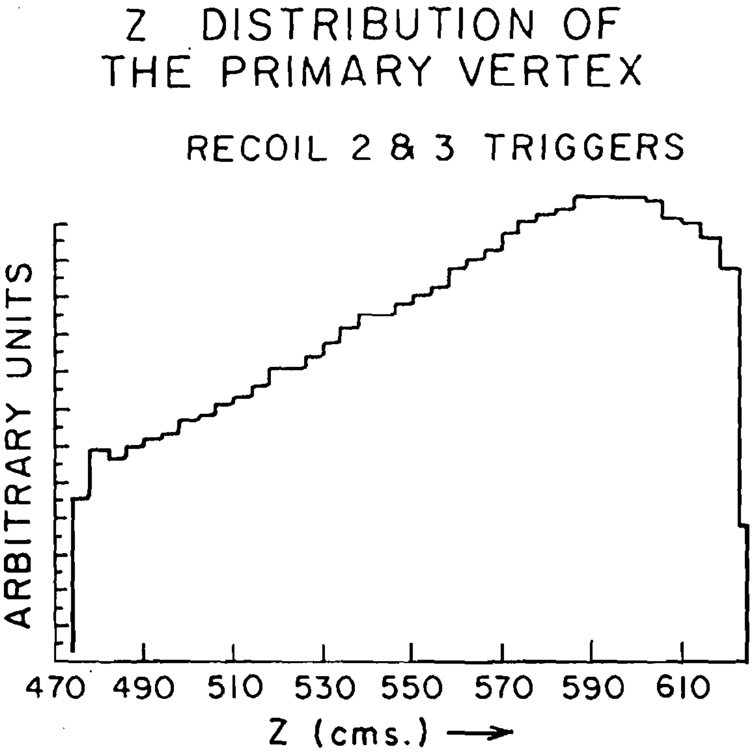
Z DISTRIBUTION OF
THE PRIMARY VERTEX
RECOIL 2 & 3 TRIGGERS
ARBITRARY UNITS
470
490
510
530
550
570
590
610
Z (cms.) →

Figure 2.8

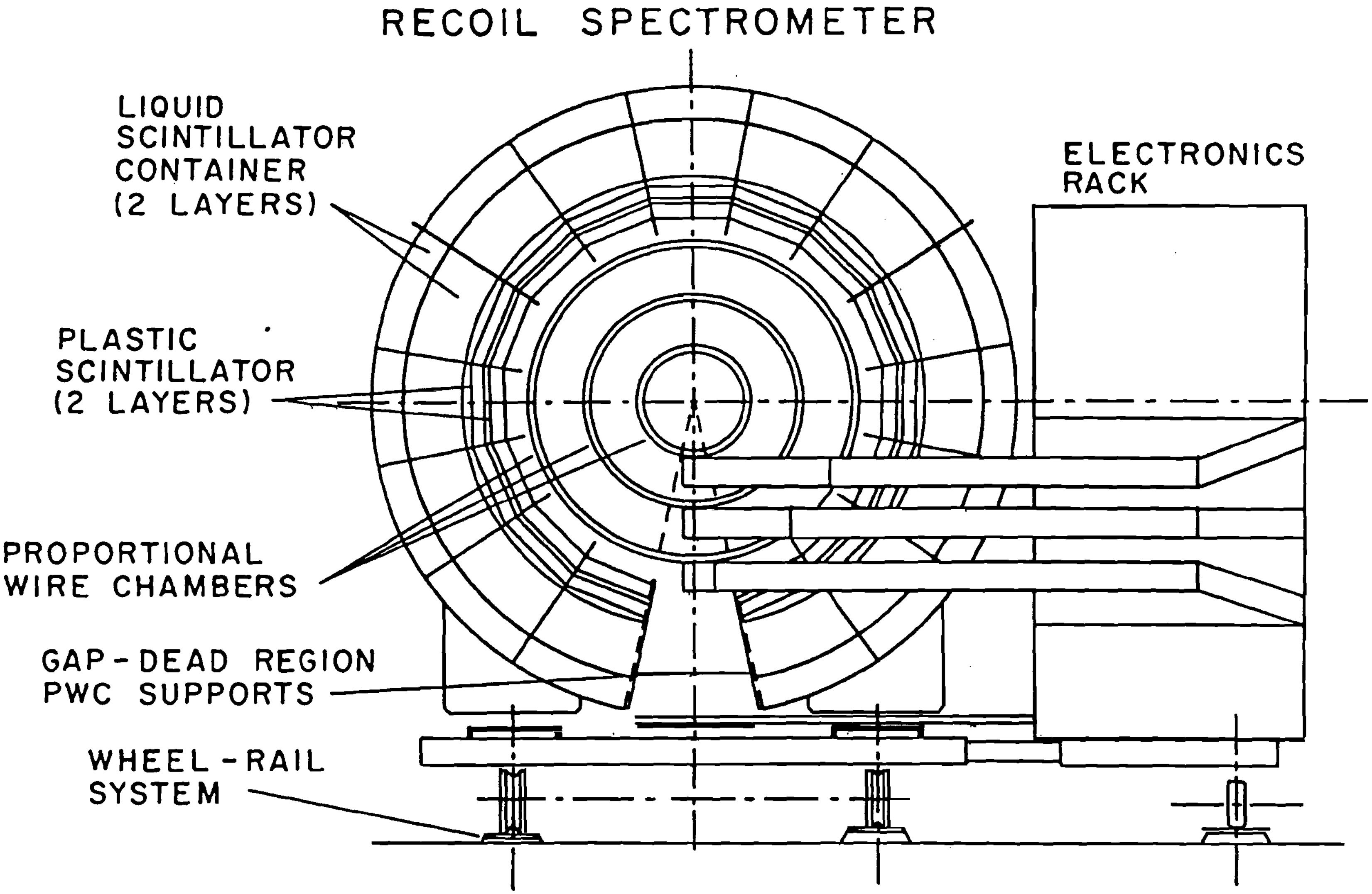

Figure 2.9 Radial profile of the recoil detector.

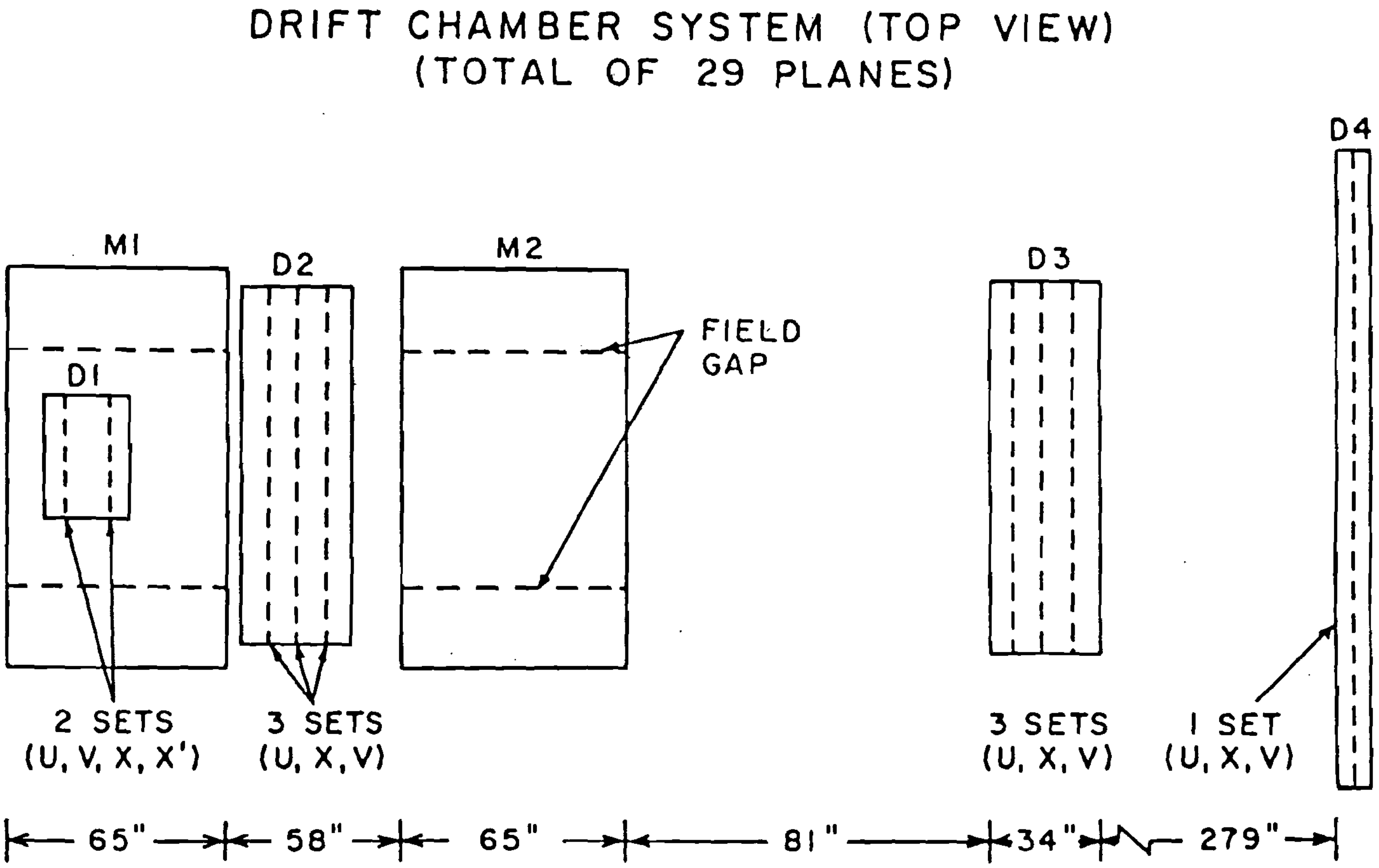

Figure 2.10 Schematic diagram of the drift chambers

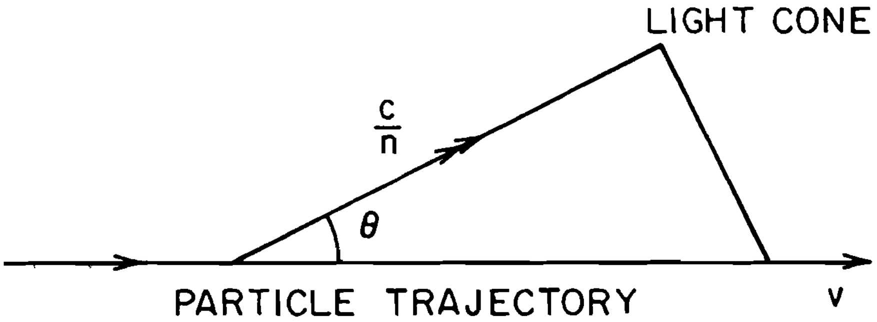

$$\cos\theta = \frac{c}{vn} = \frac{1}{\beta n}$$

Figure 2.11 Diagram of Cherenkov light emission.

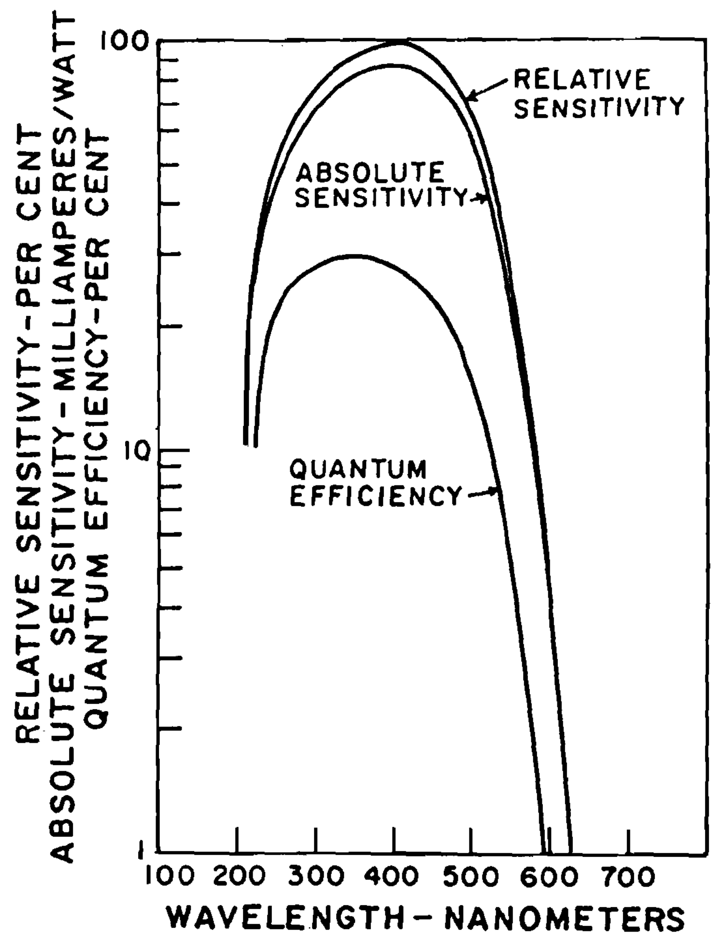

Figure 2.12 Quantum efficiency of RC8854 phototubes.

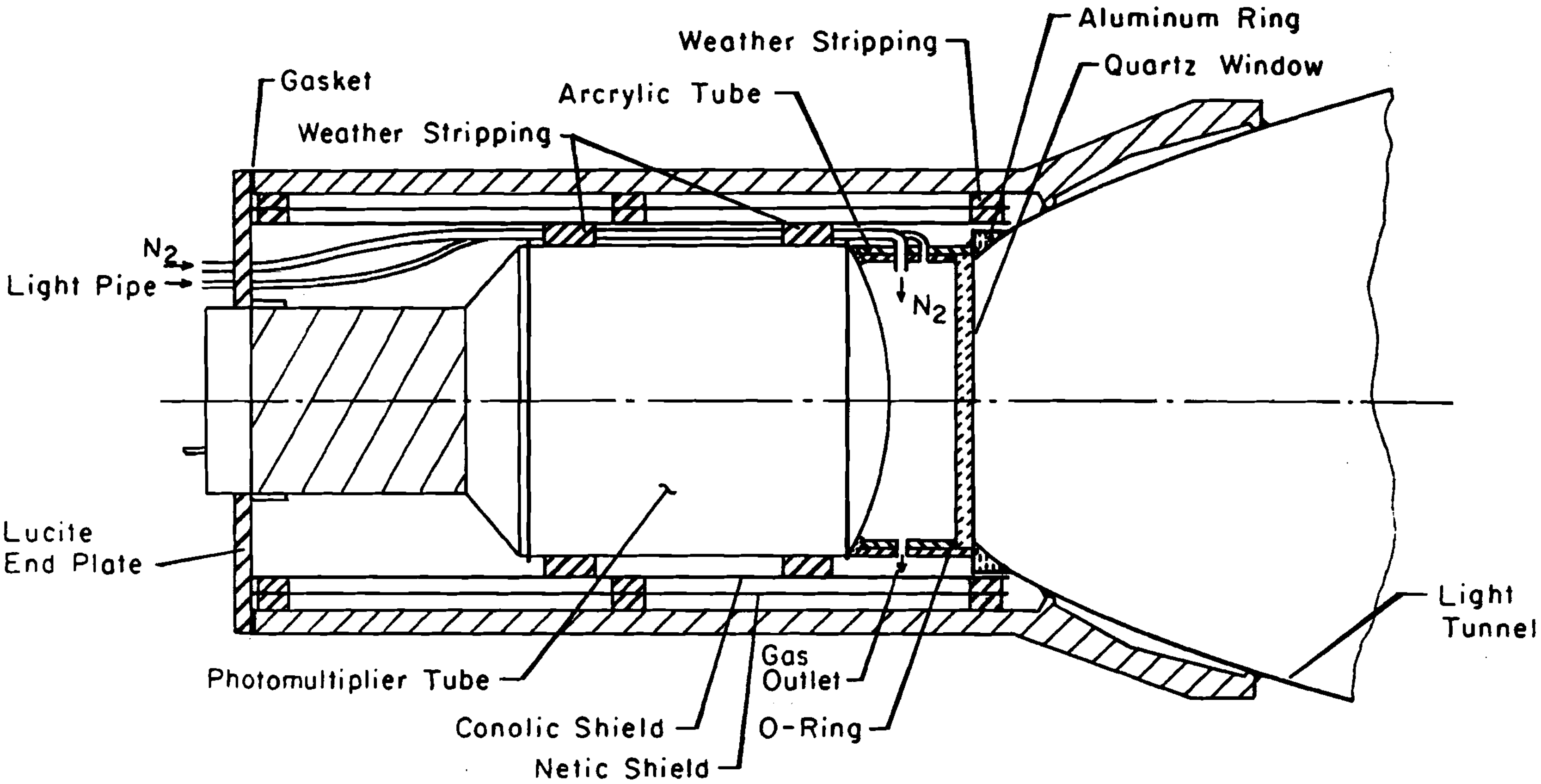

Figure 2.13 A schematic diagram of the Winston cone and phototube assembly.

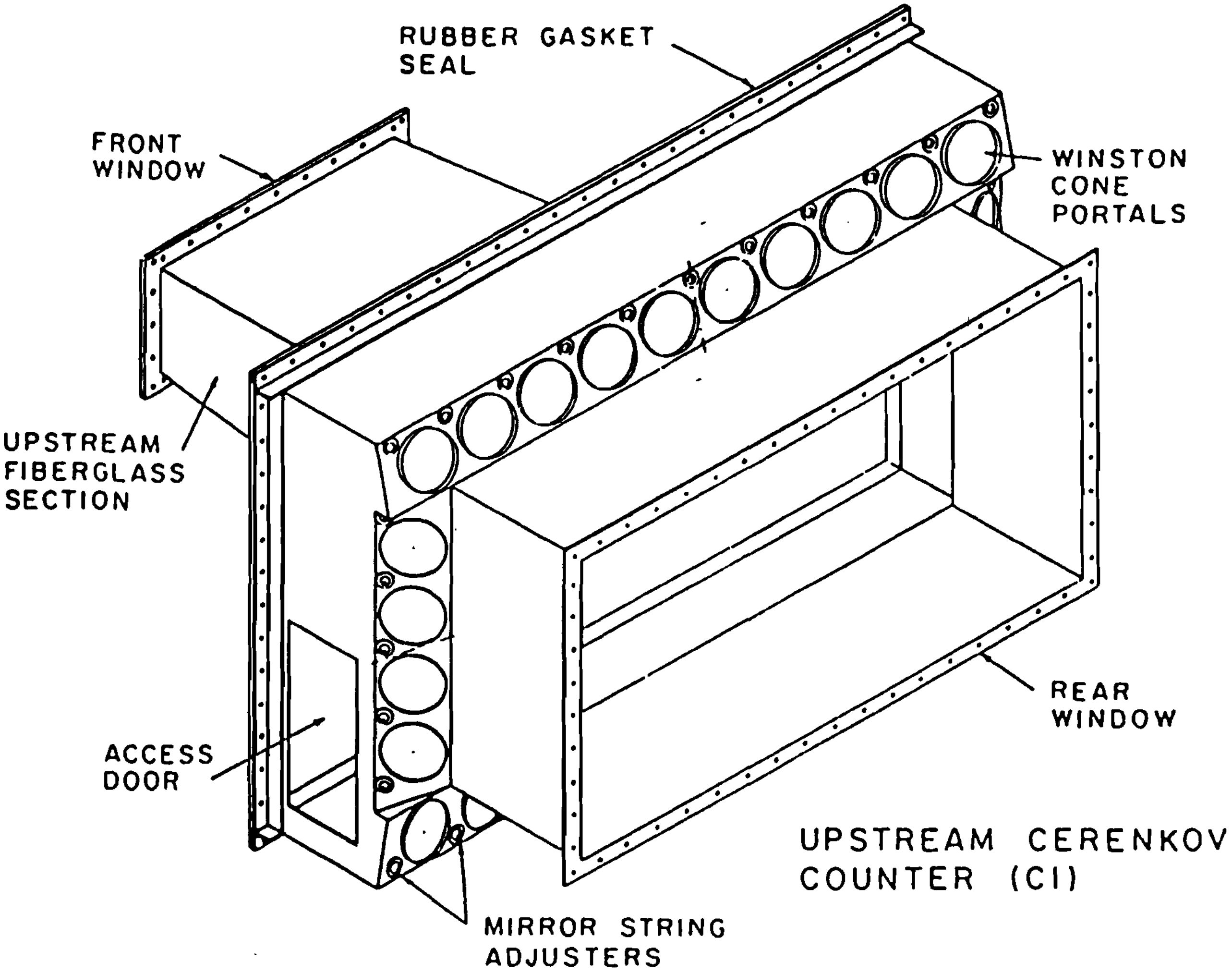

Figure 2.14 Schematic diagram of C1

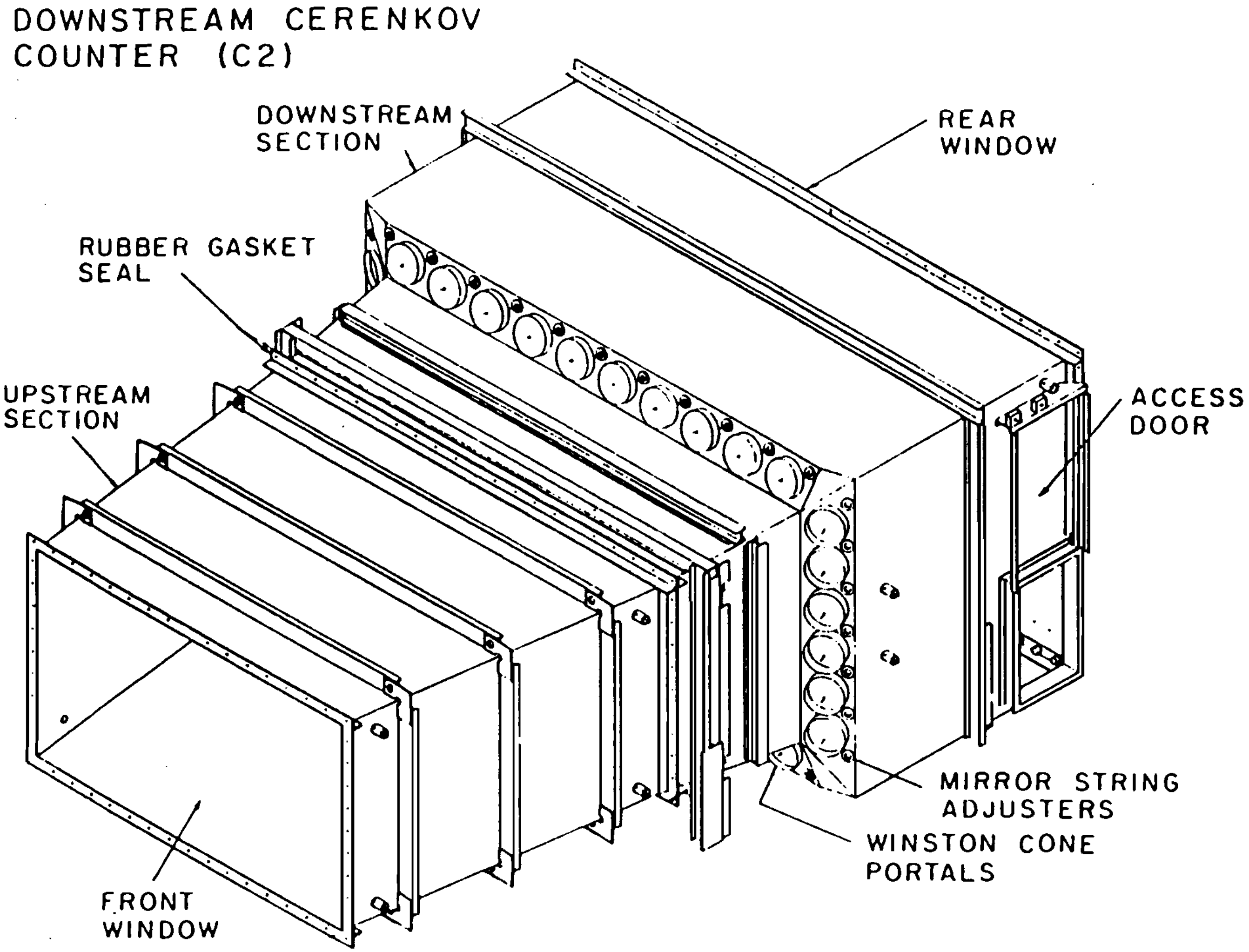

Figure 2.15 Schematic diagram of C2

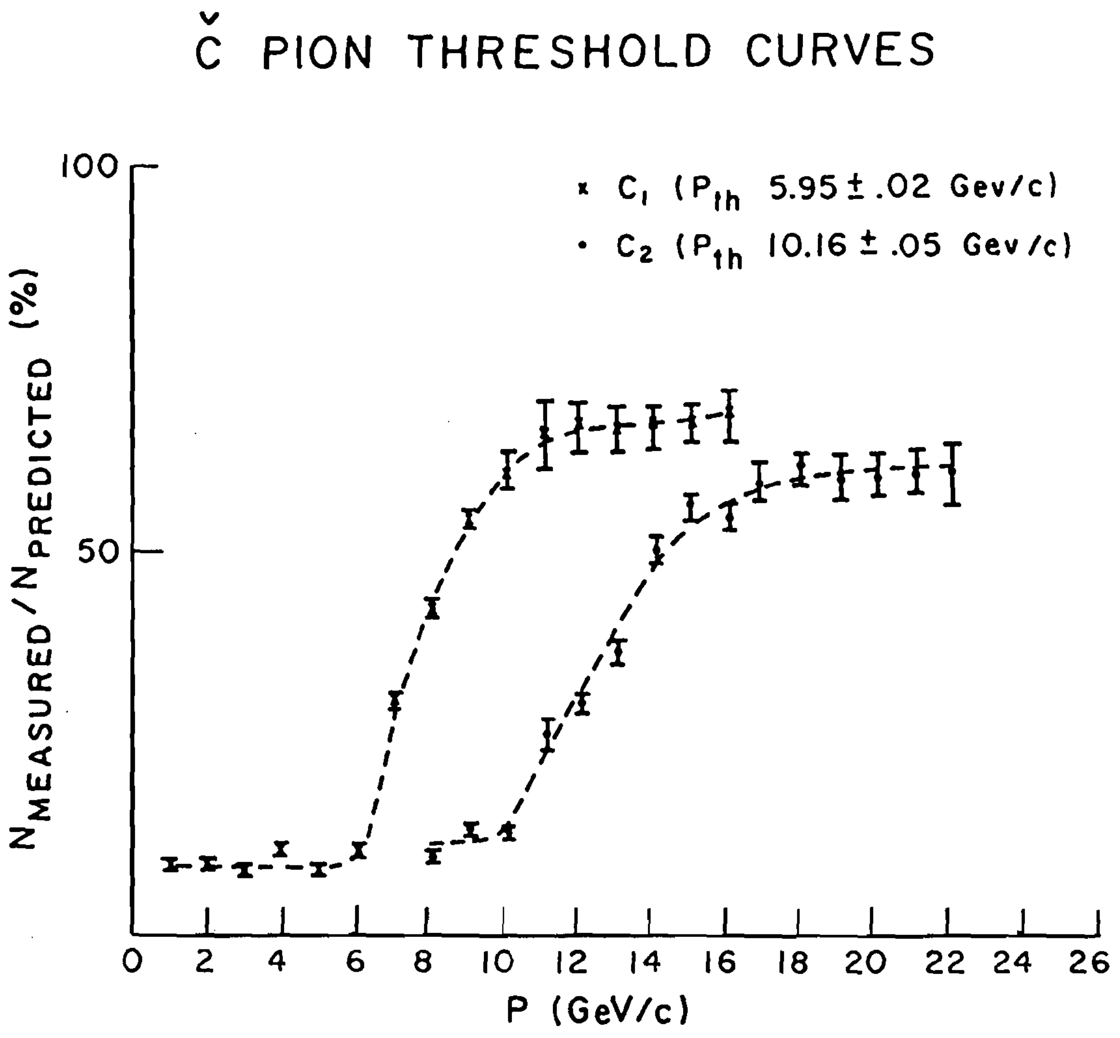

Figure 2.16 Cherenkov threshold curves for pions in C1 and C2.

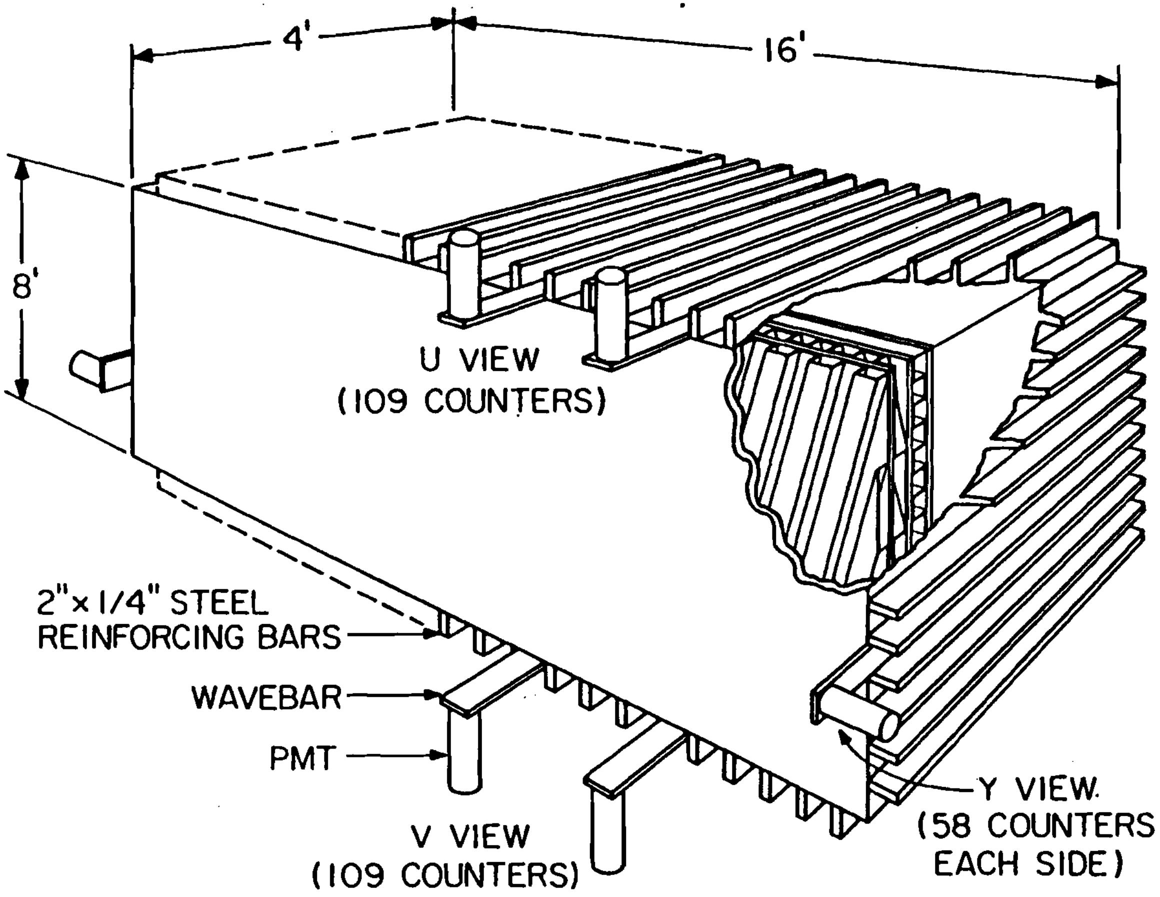

LEAD/LIQUID SCINTILLATOR SHOWER COUNTER (SLIC)
(SCHEMATIC)

Figure 2.17

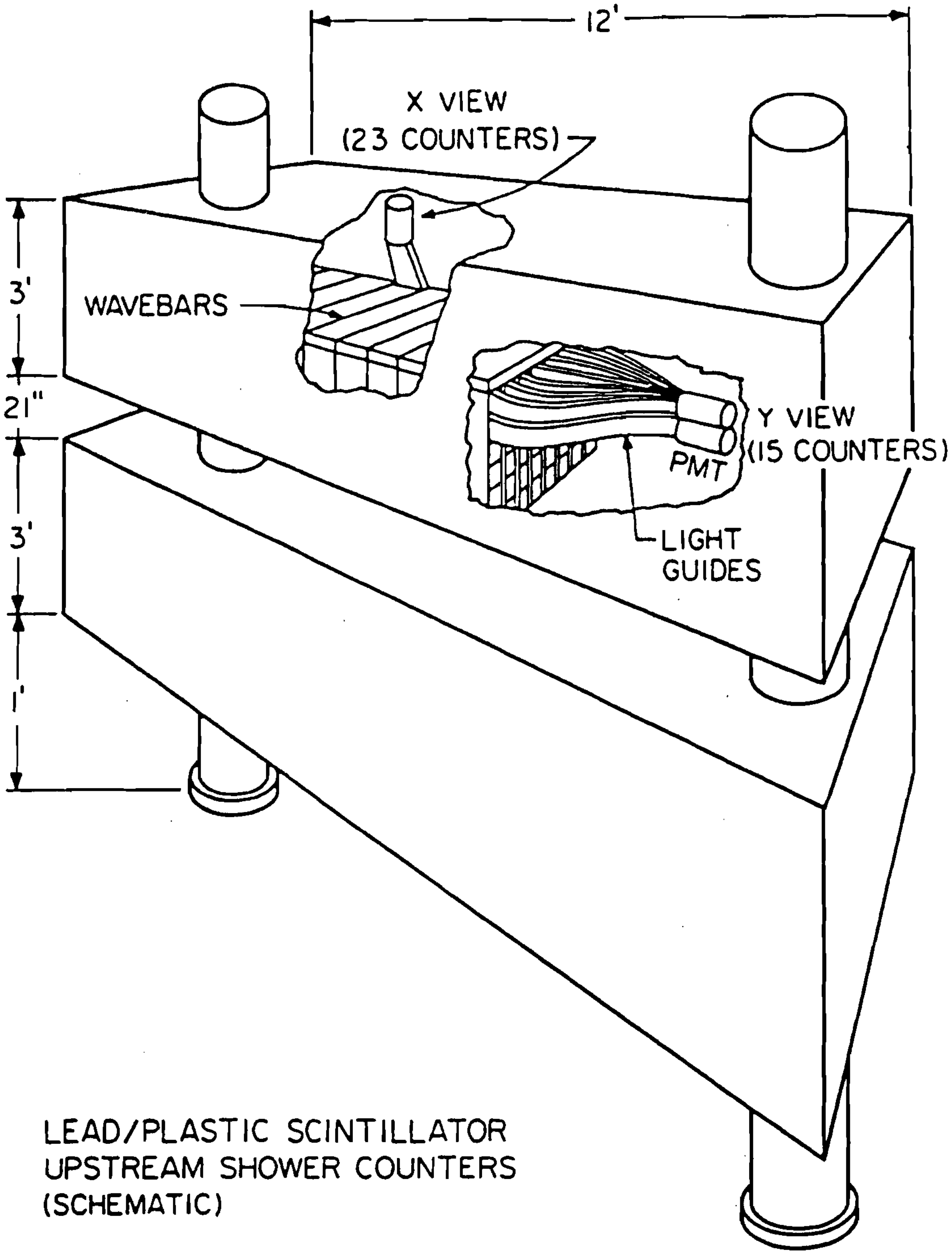
12'
X VIEW
(23 COUNTERS)
3'
WAVEBARS
21"
Y VIEW
(15 COUNTERS)
PMT
3'
LIGHT
GUIDES
1'
LEAD/PLASTIC SCINTILLATOR
UPSTREAM SHOWER COUNTERS
(SCHEMATIC)

Figure 2.18

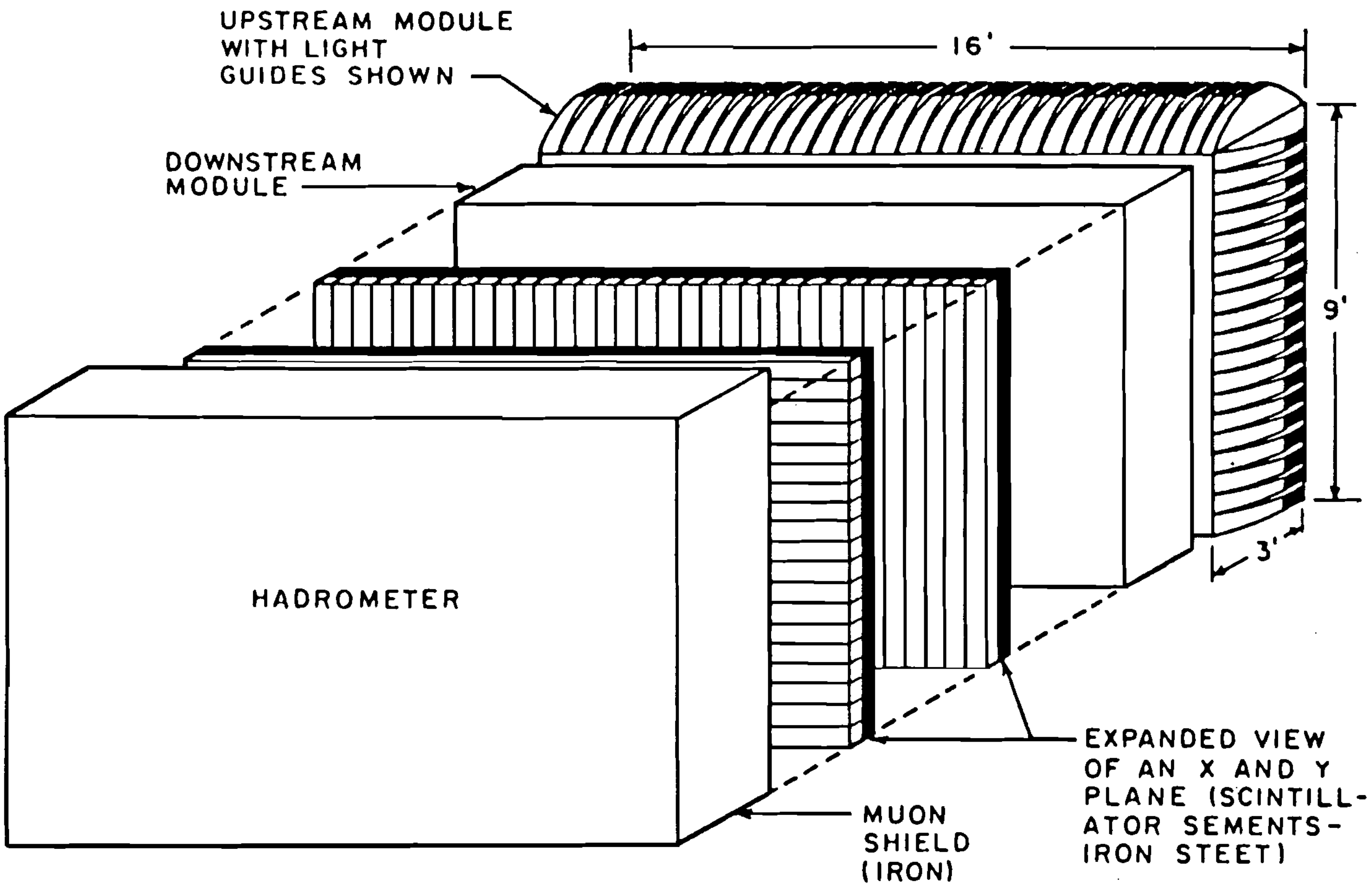

Figure 2.19 Schematic diagram of the hadrometer.

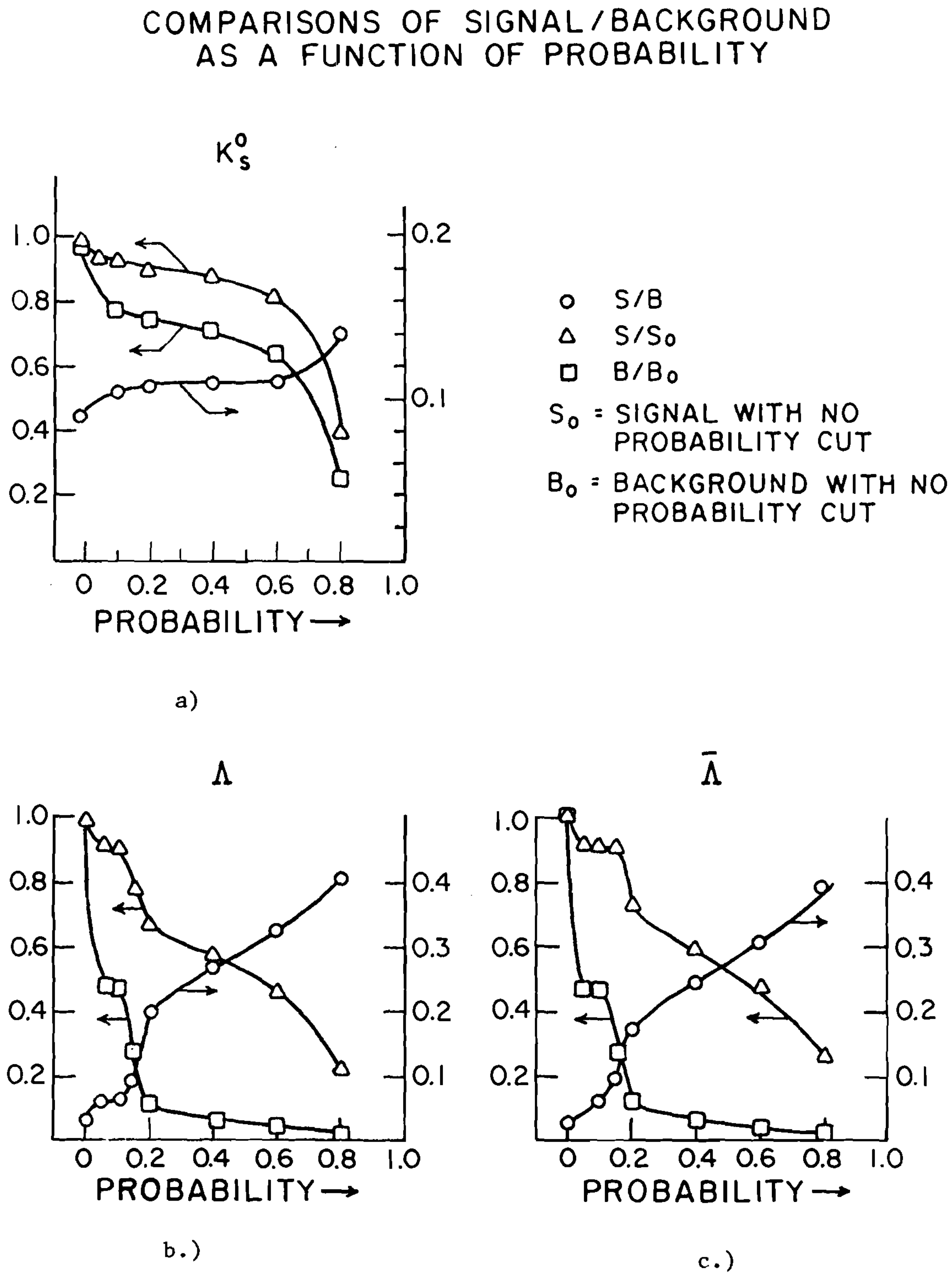

Figure 4.1 Comparisons of the signal/background as a function of probability. Arrows point to the appropriate scale.

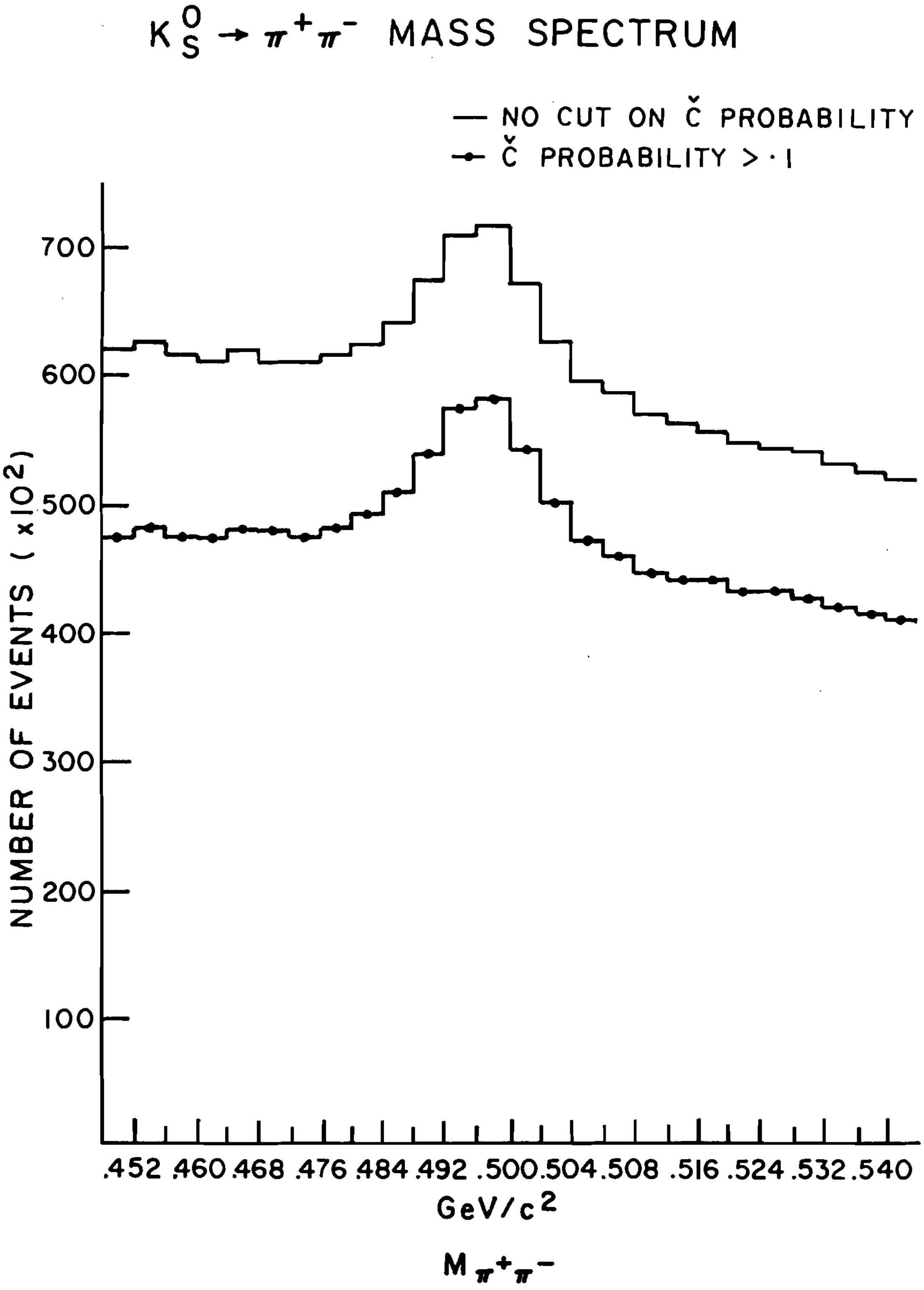

Figure 4.2 Invariant mass distribution of oppositely charged pions without (-) and without (-.-) a Cherenkov cut

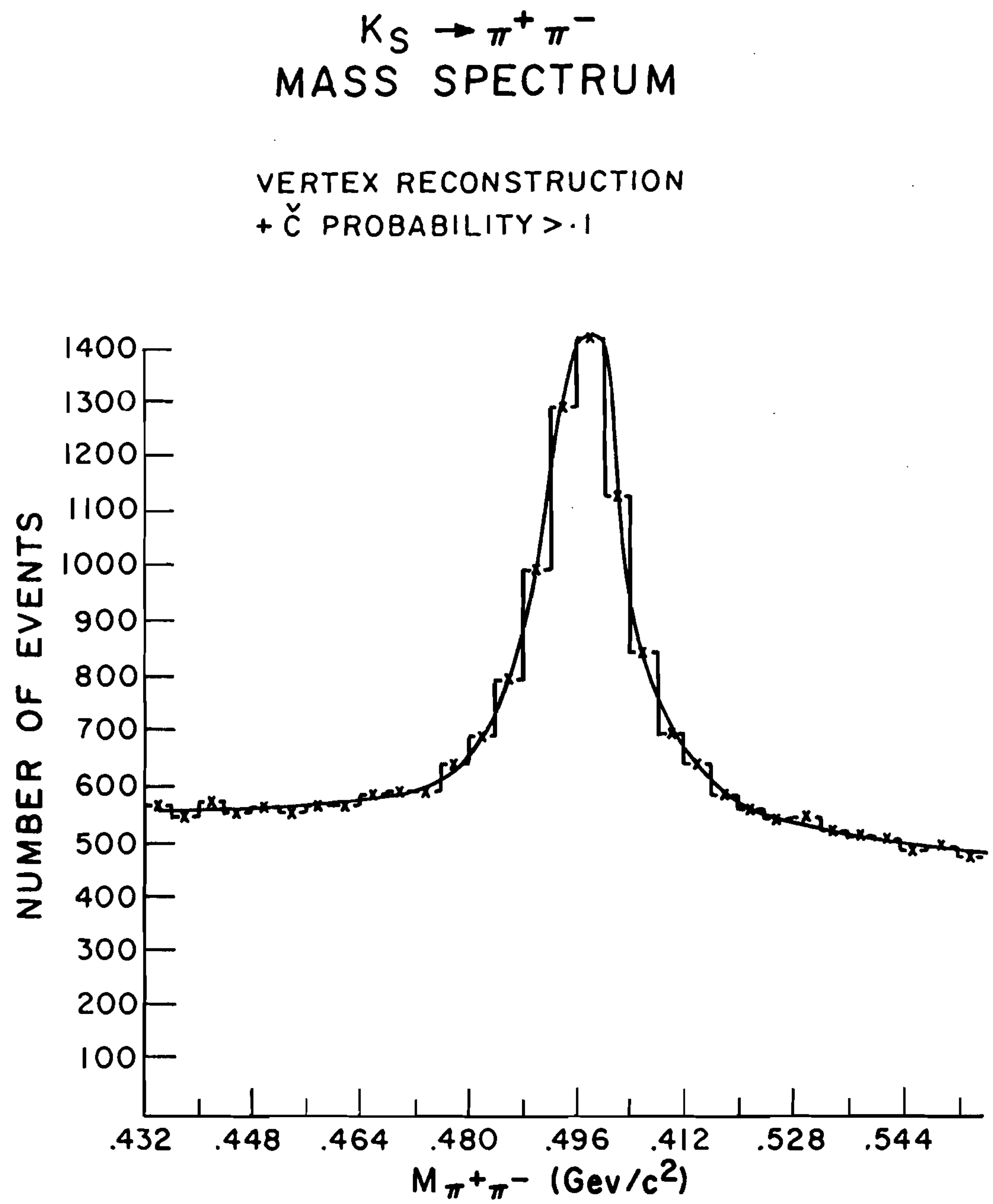

Figure 4.3 Mass distribution of neutral kaons with verticising.

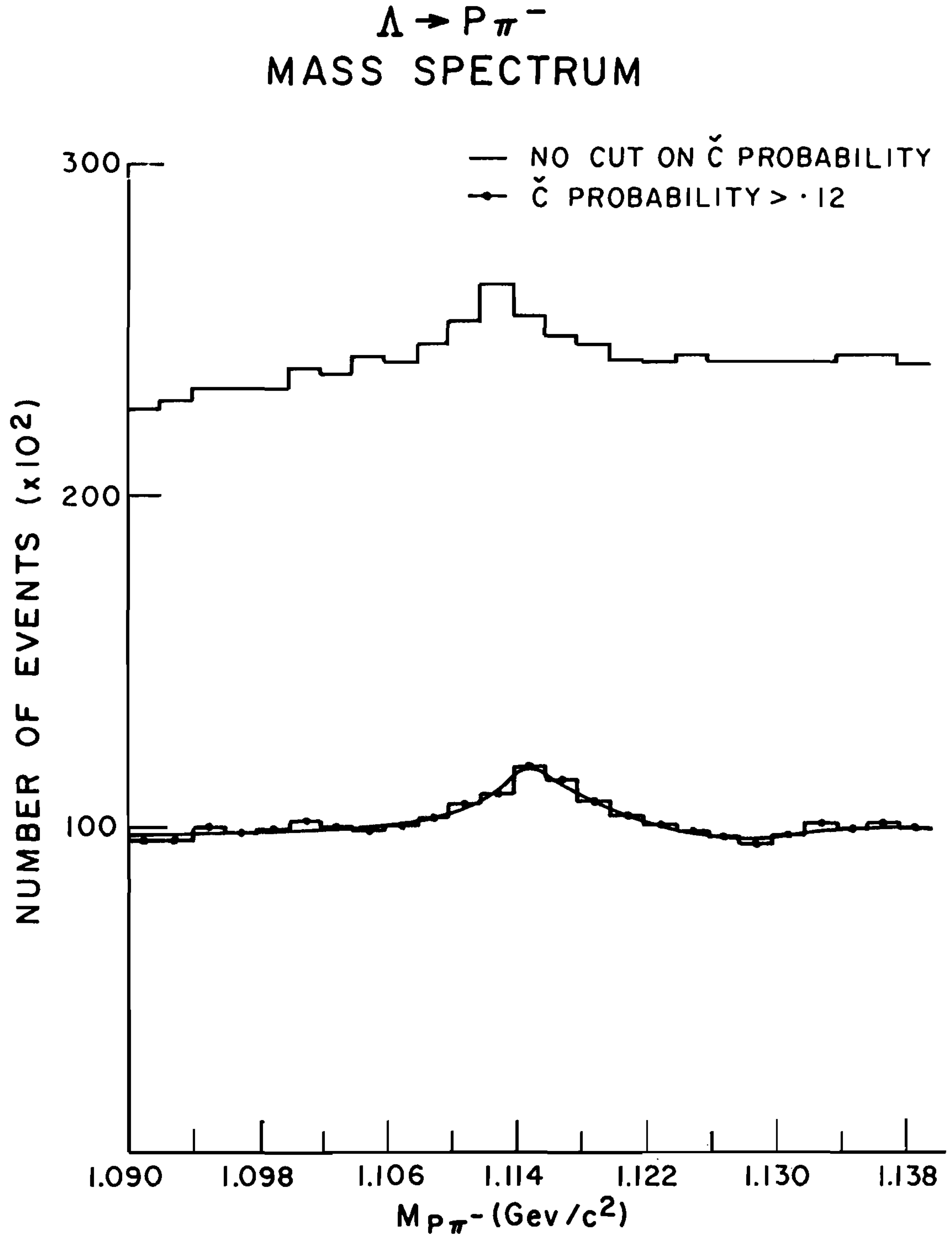

Figure 4.4 Invariant mass distribution of a positive proton and a negative pion without (-) and with (-.-) a Cherenkov cut.

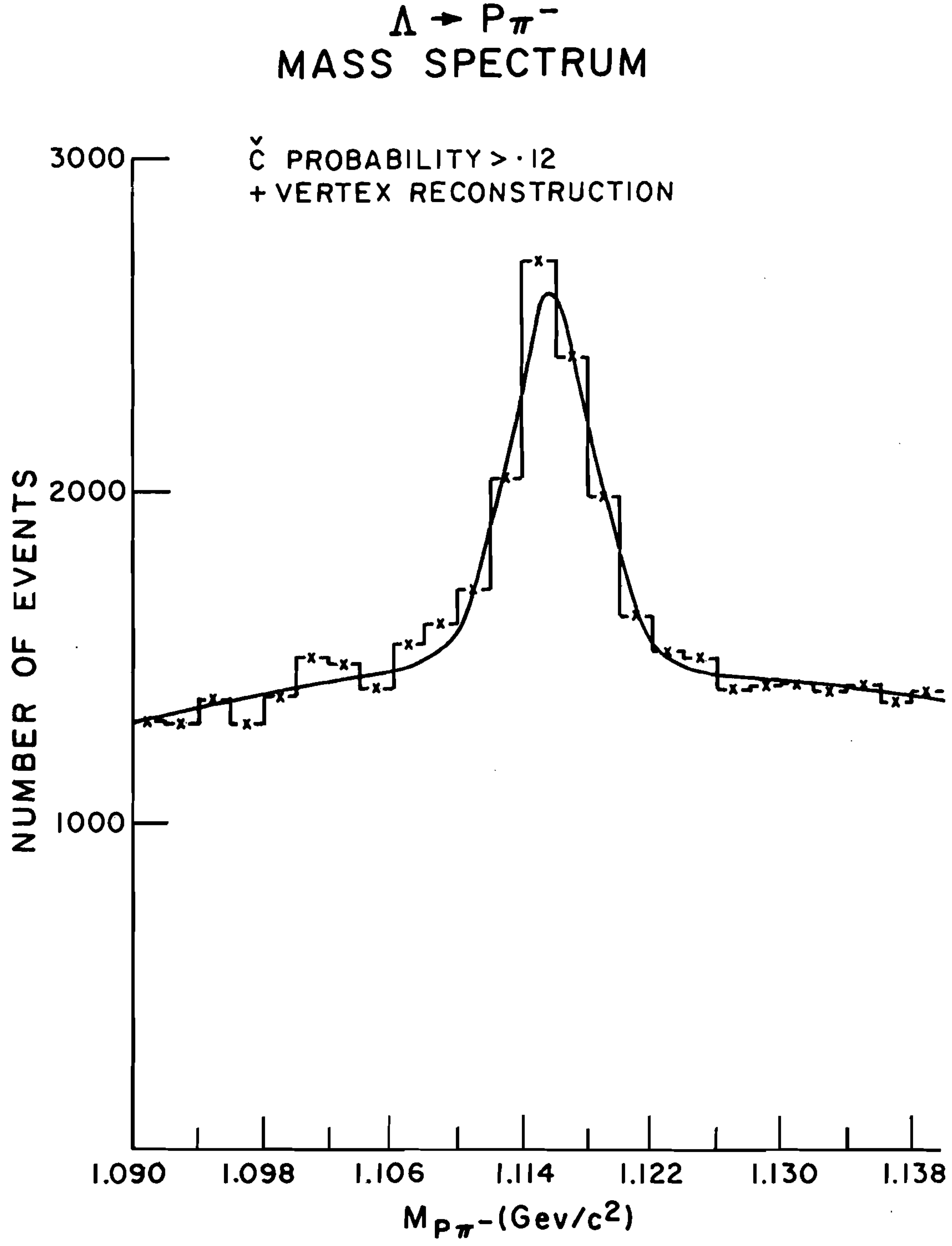

Figure 4.5 Mass distribution of lambdas with a verticising cut.

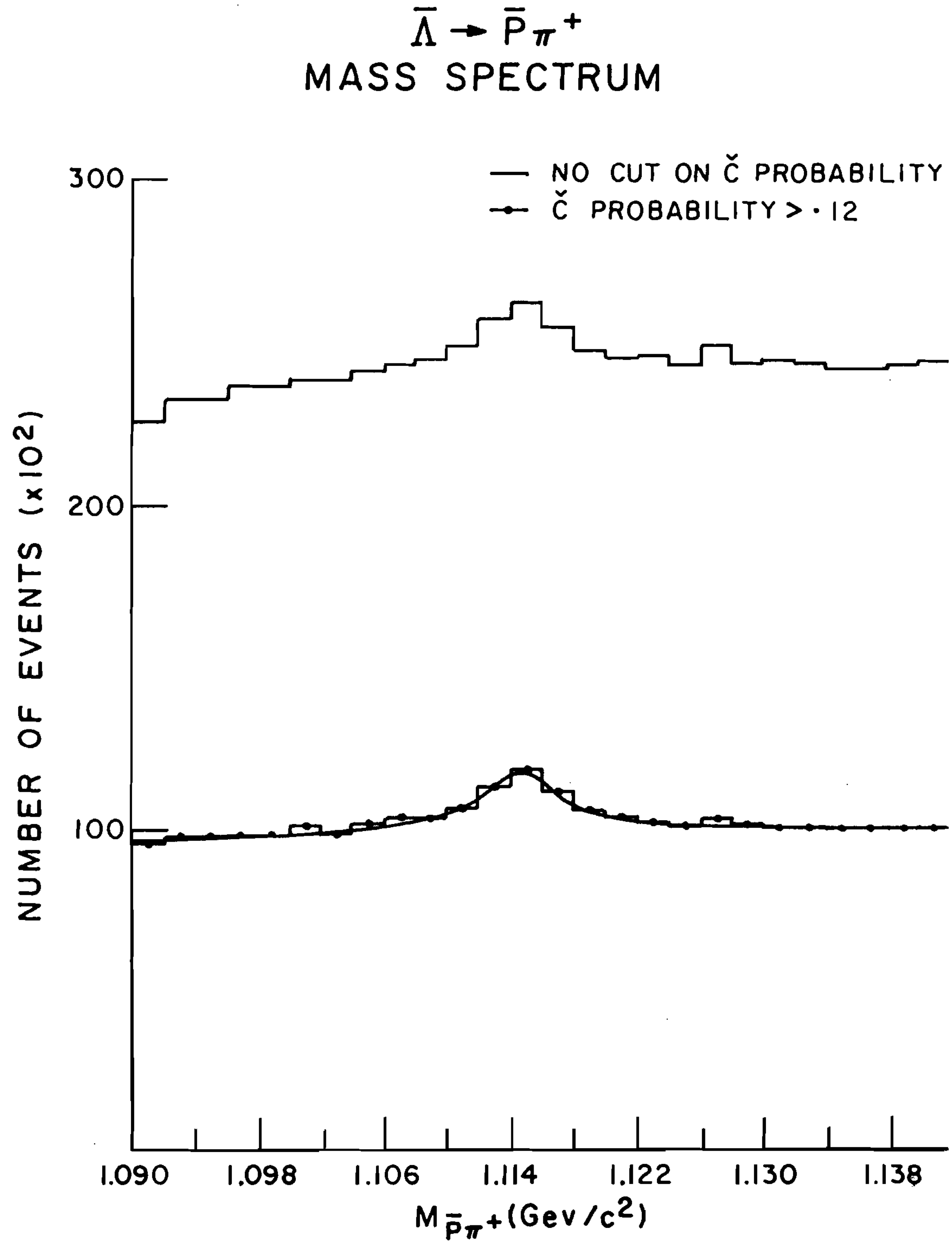

Figure 4.6 Invariant mass distribution of a negative proton and a positive pion without (-) and with (-.-) a Cherenkov cut.

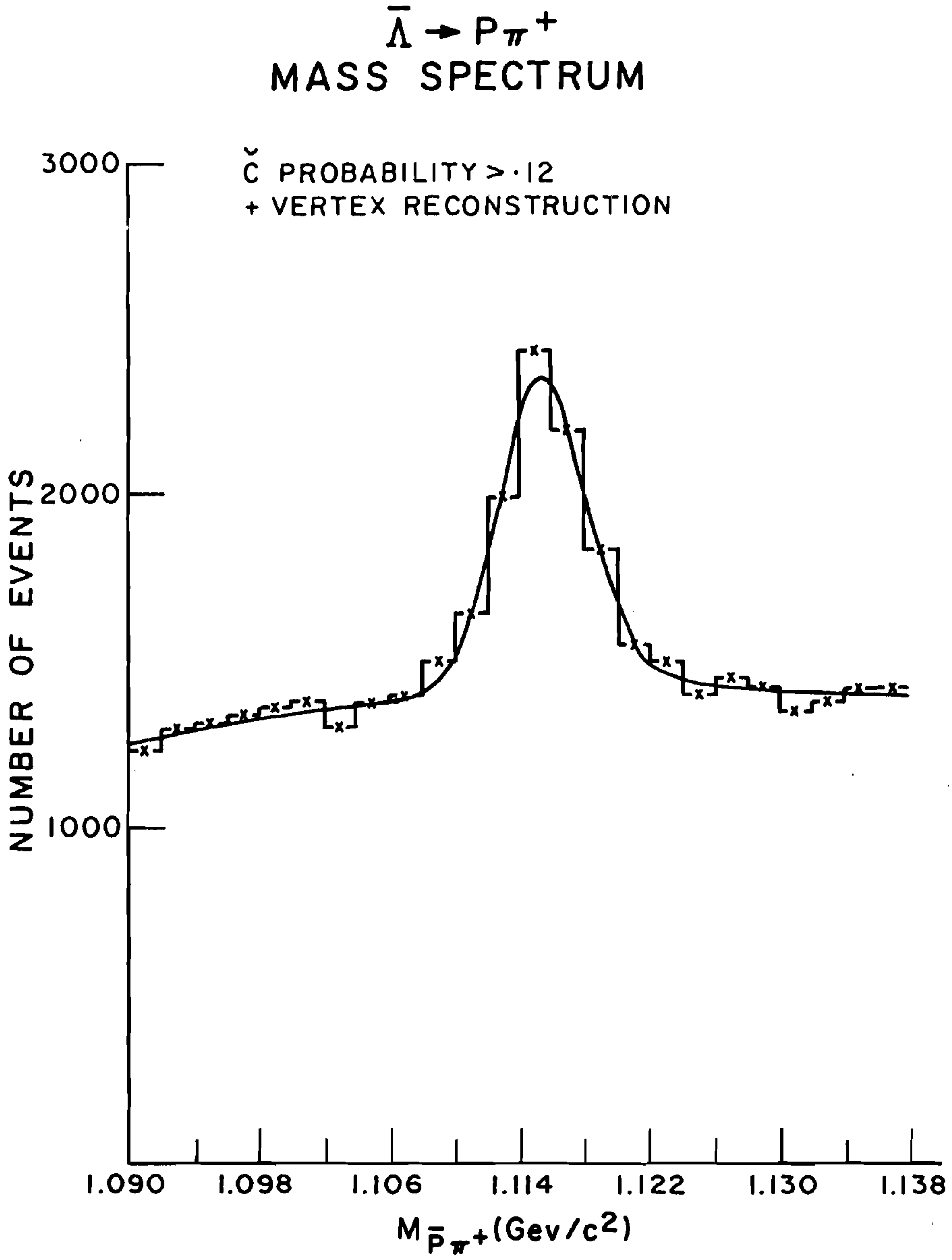

Figure 4.7 Mass distribution of antilambdas with a verticising cut.

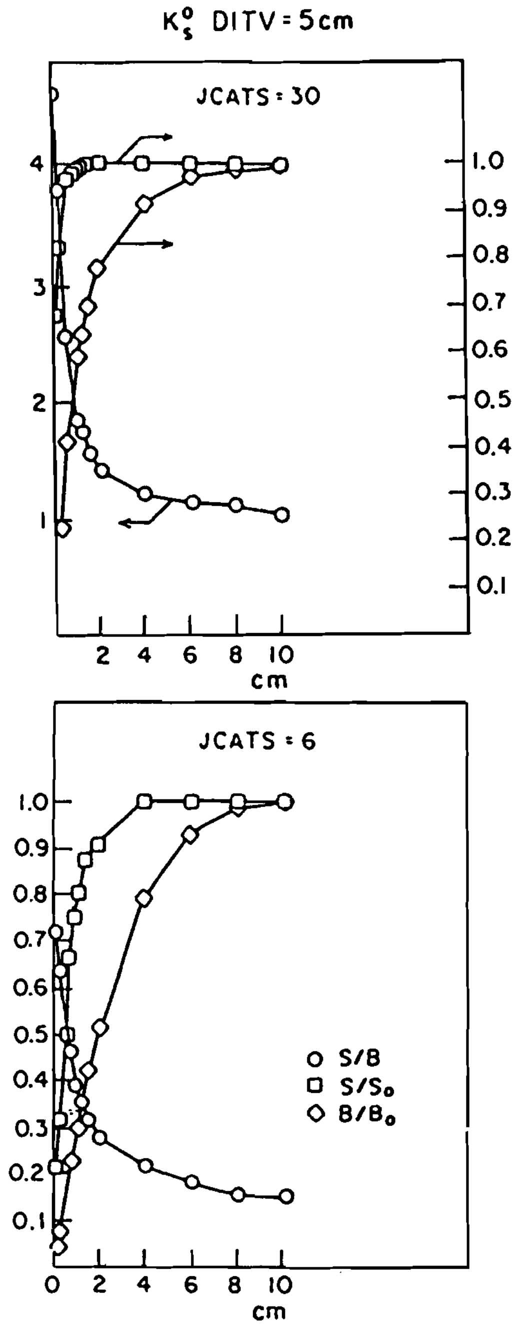

Figure 4.8 Signal to background variation for neutral kaons with DITV = 5 cm. and JCATS = 6 and 30

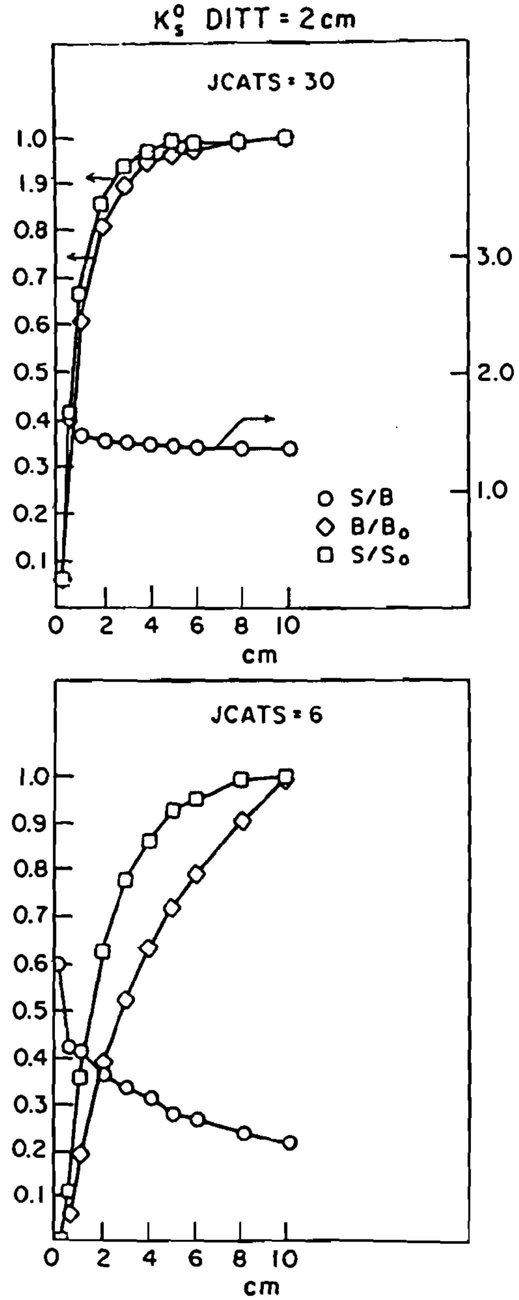

Figure 4.9 Signal to background variation for neutral kaons with DITT = 2 cm. and JCATS = 6 and 30

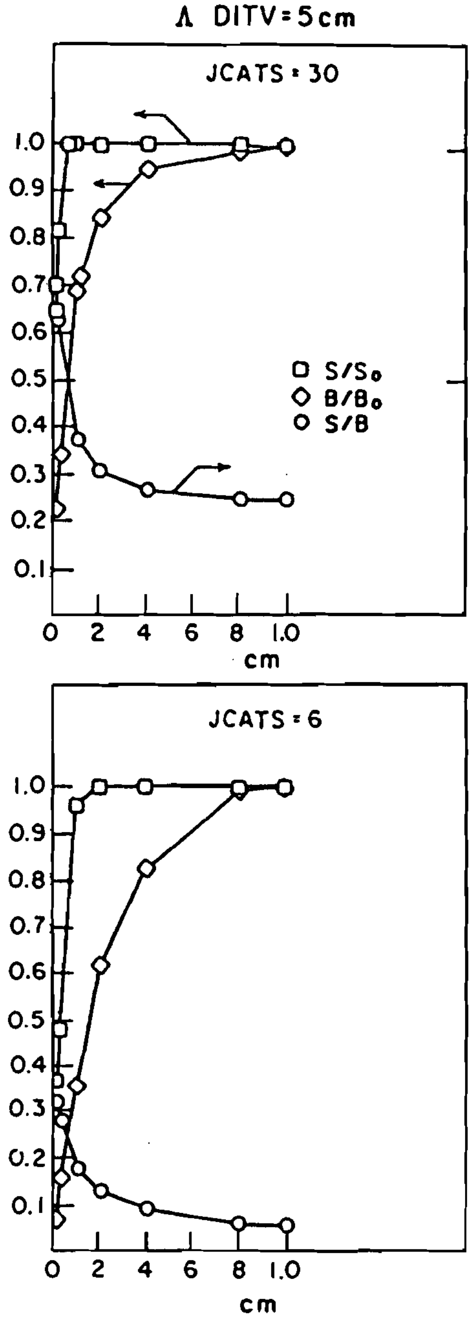

Figure 4.10 Signal to background variation for lambdas with DITV = 5 cm. and JCATS = 6 and 30.

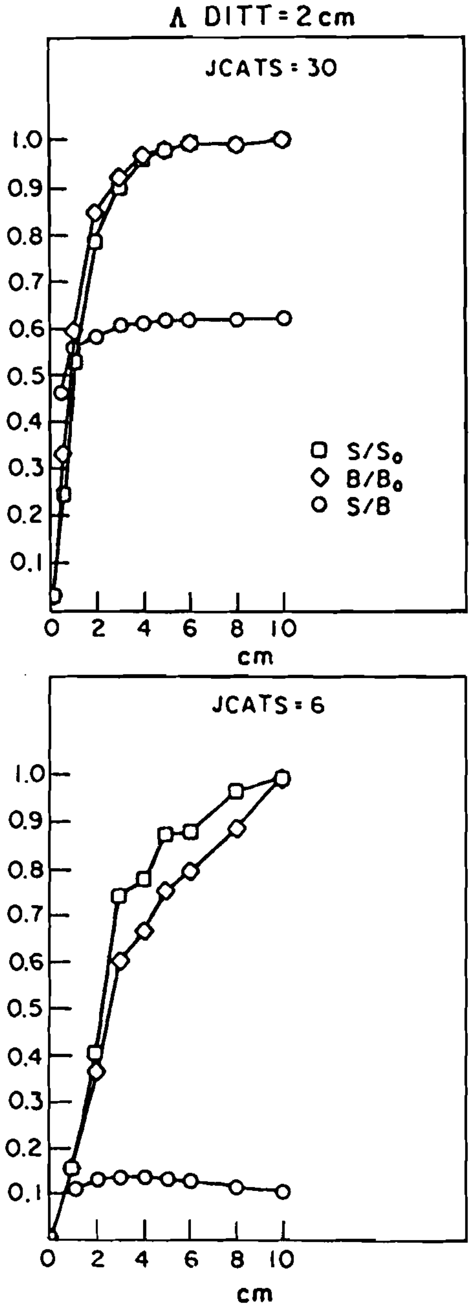

Figure 4.11 Signal to background variation for lambdas with DITT = 2 cm. and JCATS = 6 and 30.

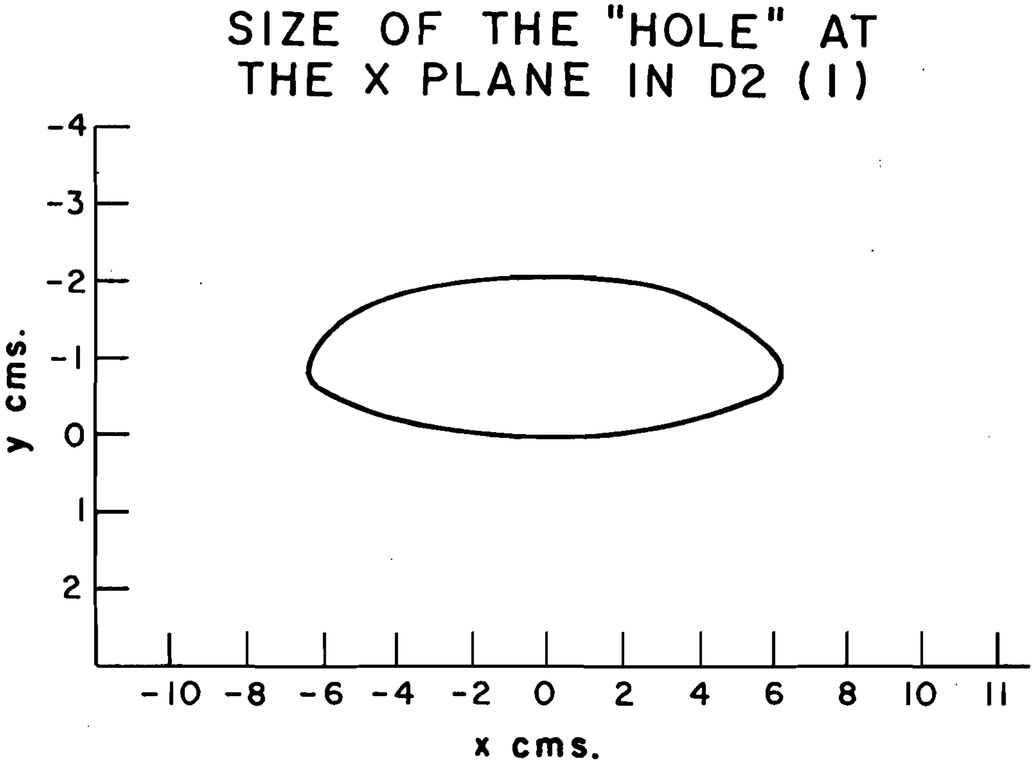

Figure 5.1 The effective size of the inefficient region in the drift chambers.

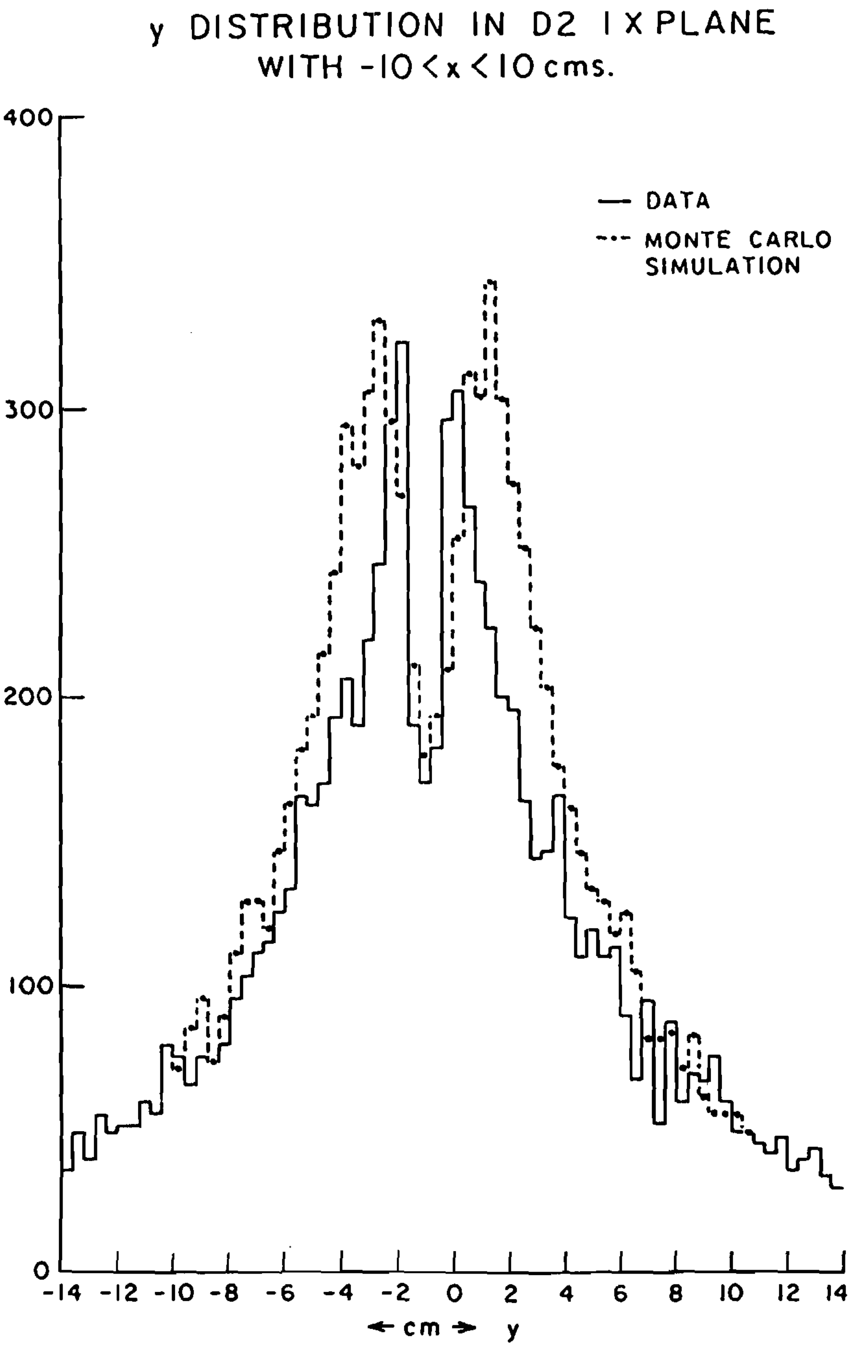
y DISTRIBUTION IN D2 I X PLANE
WITH -10 < x < 10 cms.
400
300
200
100
0
— DATA
-·- MONTE CARLO SIMULATION
-14
-12
-10
-8
-6
-4
-2
0
2
4
6
8
10
12
14
← cm → y

Figure 5.2

y DISTRIBUTION IN D2 I X PLANE WITH -2<x<0 cms.

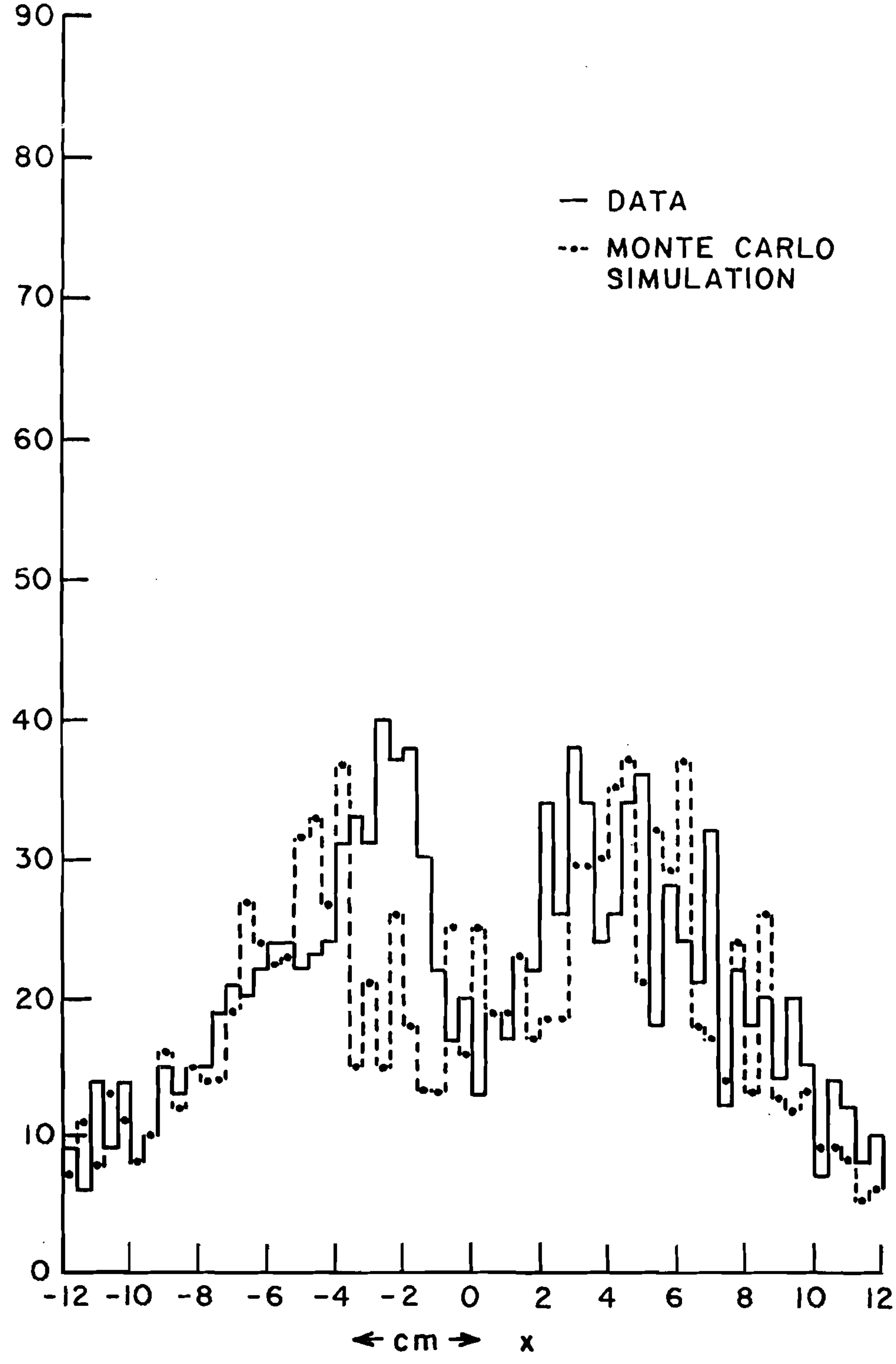

Figure 5.3

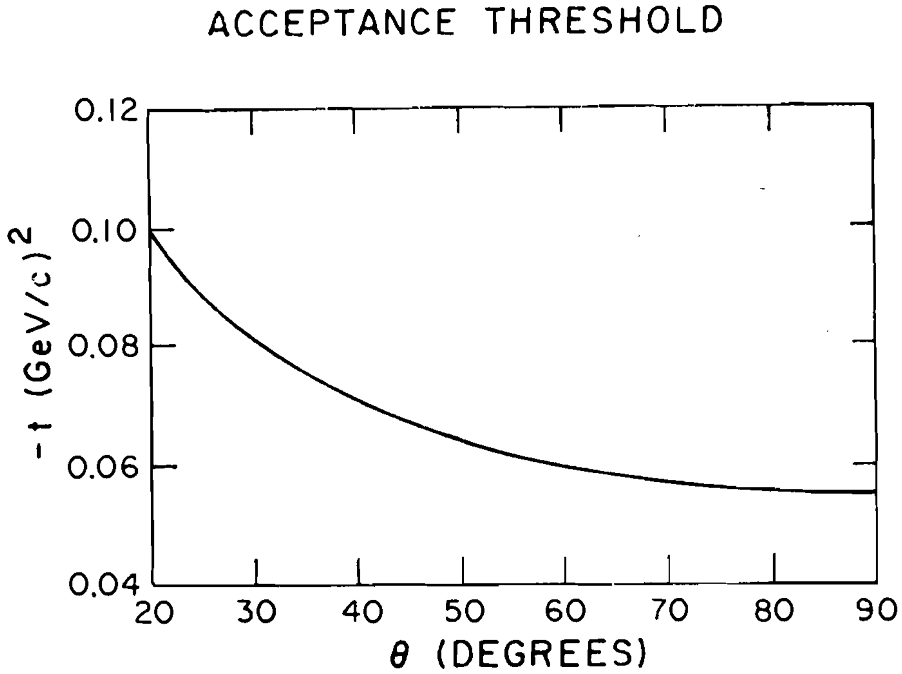

Figure 5.4 Acceptance threshold curves for the recoil proton.

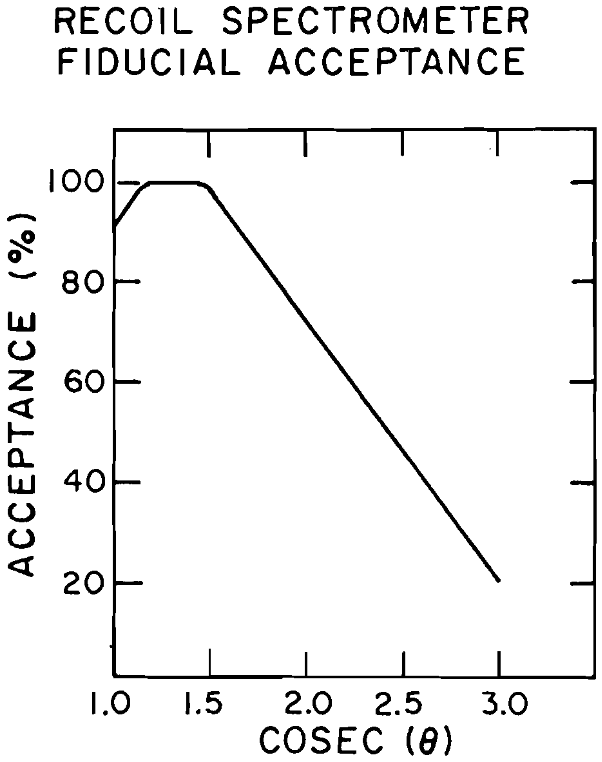

Figure 5.5 Fiducial acceptance curve for the recoil proton

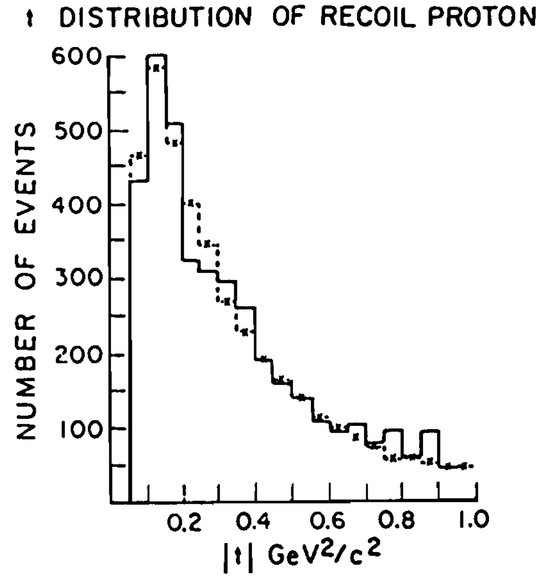

Figure 5.6 Comparison of M.C. events with data events for t distribution.

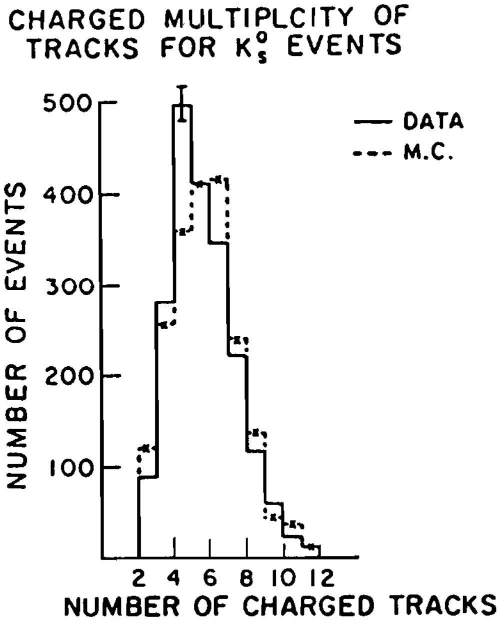

Figure 5.7 Comparison of M.C. events with data events for the charged multiplicity

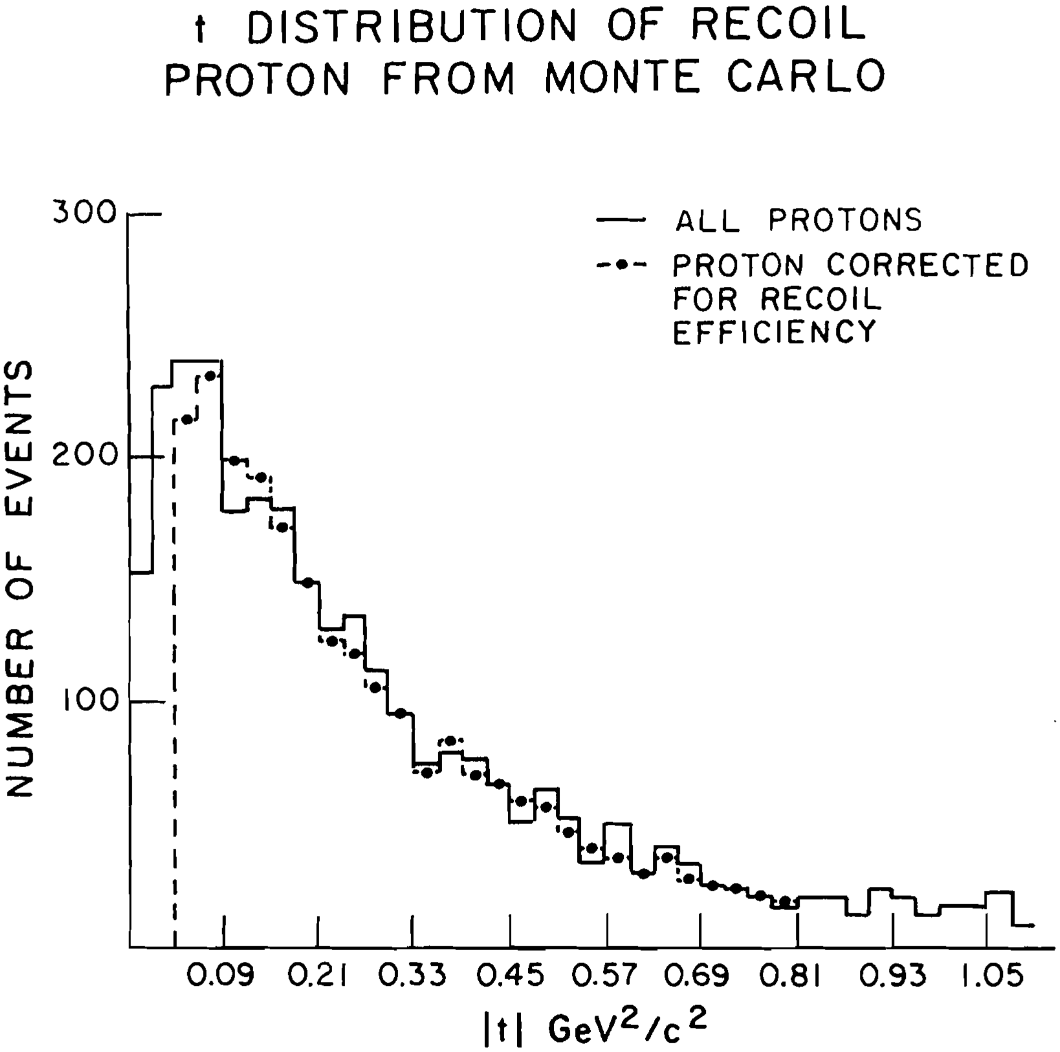
t DISTRIBUTION OF RECOIL
PROTON FROM MONTE CARLO
— ALL PROTONS
-•- PROTON CORRECTED FOR RECOIL EFFICIENCY
NUMBER OF EVENTS
300
200
100
0.09
0.21
0.33
0.45
0.57
0.69
0.81
0.93
1.05
|t| GeV^2/c^2

Figure 5.8

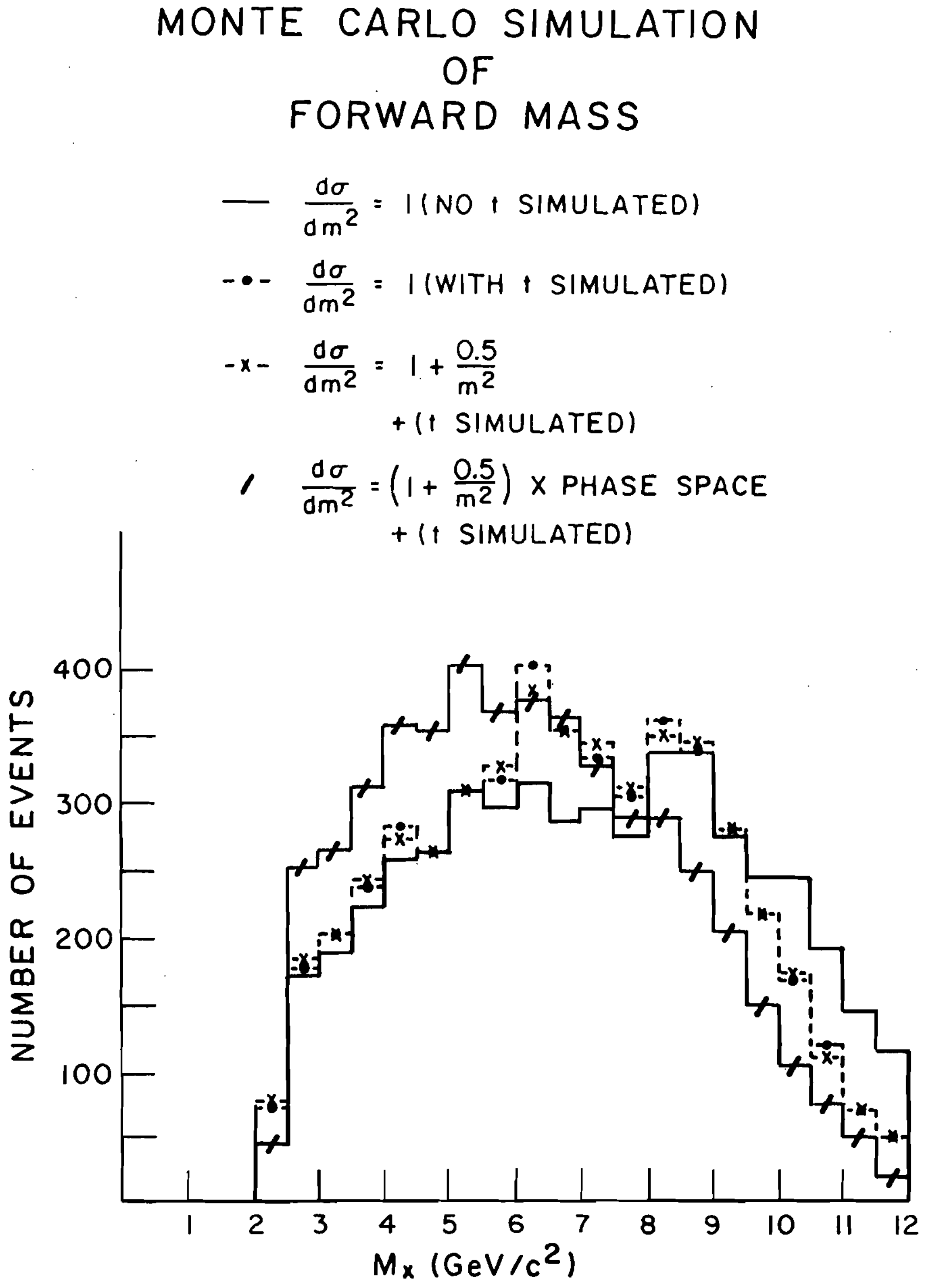
MONTE CARLO SIMULATION
OF
FORWARD MASS
— $\frac{d\sigma}{dm^2}$ = 1 (NO t SIMULATED)
-•- $\frac{d\sigma}{dm^2}$ = 1 (WITH t SIMULATED)
-x- $\frac{d\sigma}{dm^2}$ = $1 + \frac{0.5}{m^2}$ + (t SIMULATED)
/ $\frac{d\sigma}{dm^2}$ = $\left(1 + \frac{0.5}{m^2}\right)$ X PHASE SPACE + (t SIMULATED)
NUMBER OF EVENTS
400
300
200
100
1
2
3
4
5
6
7
8
9
10
11
12
M_x (GeV/c^2)

Figure 5.9

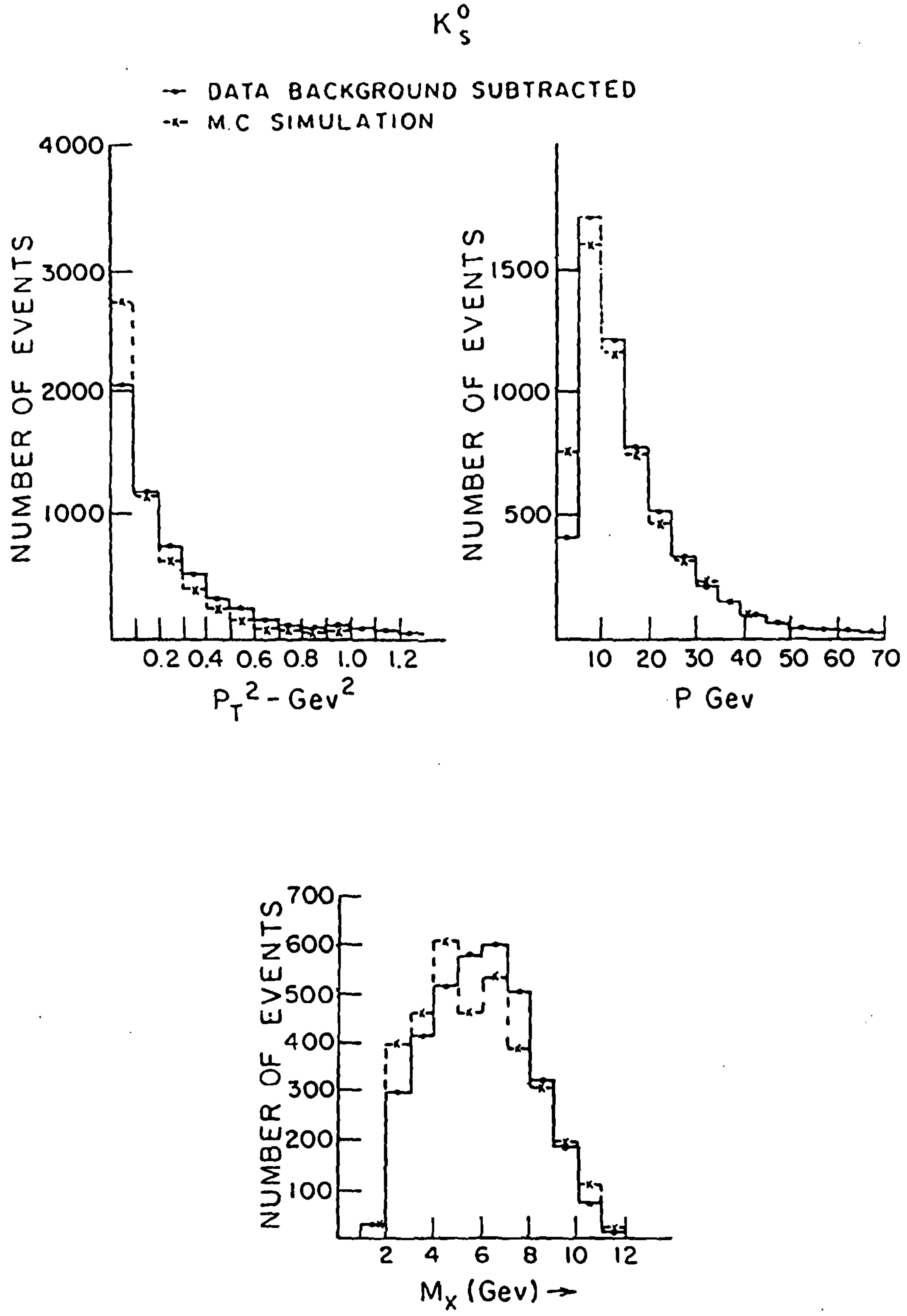

Figure 5.10 Comparisons of M.C. and data events for the longitudinal and transverse momentum, and M_X.

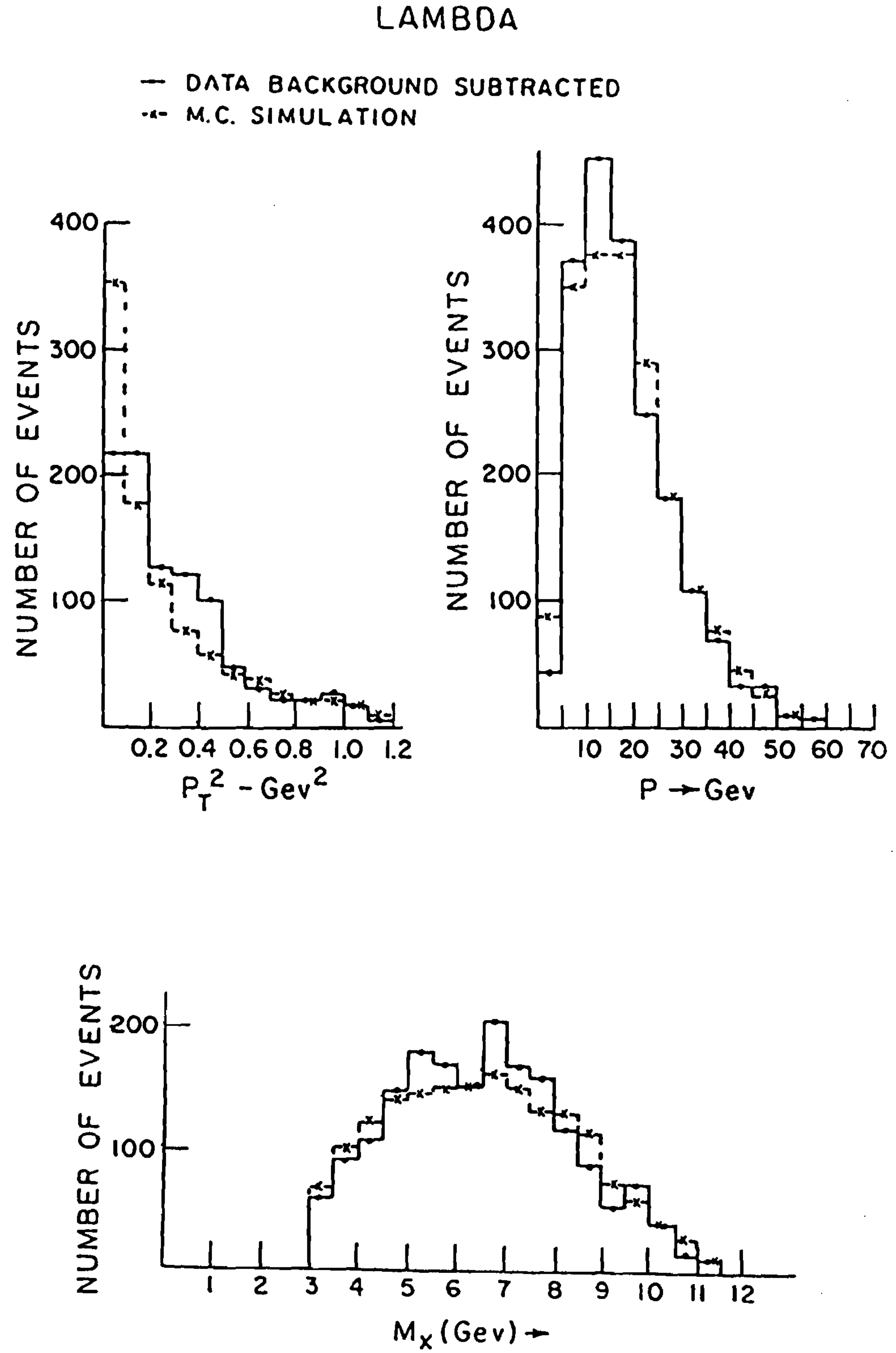

Figure 5.11 Comparisons of M.C. events and data events for the longitudinal and transverse momentum and M_X .

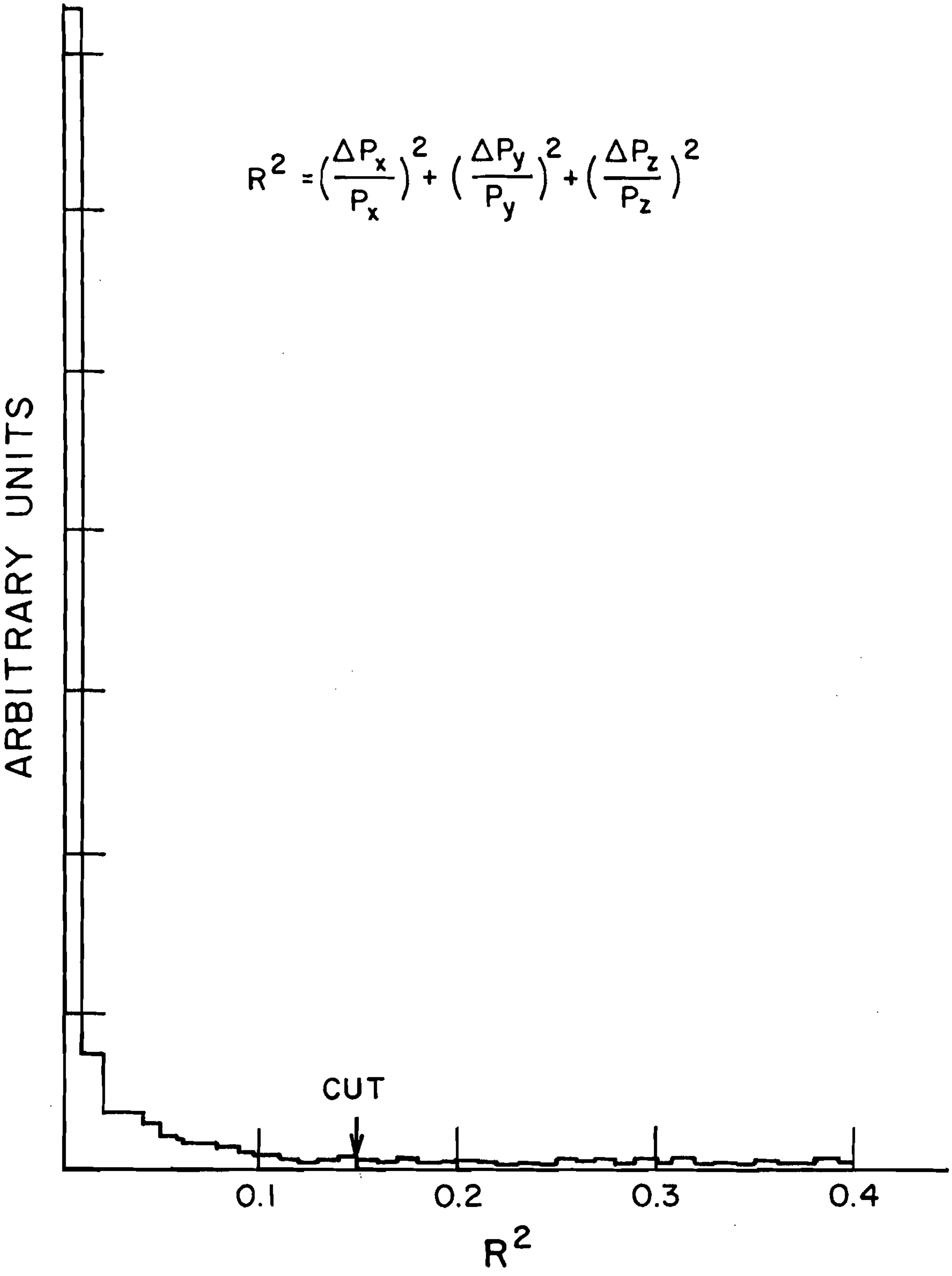
$R^2 = \left(\frac{\Delta P_x}{P_x}\right)^2 + \left(\frac{\Delta P_y}{P_y}\right)^2 + \left(\frac{\Delta P_z}{P_z}\right)^2$
ARBITRARY UNITS
CUT
0.1
0.2
0.3
0.4
R^2

Figure 5.12

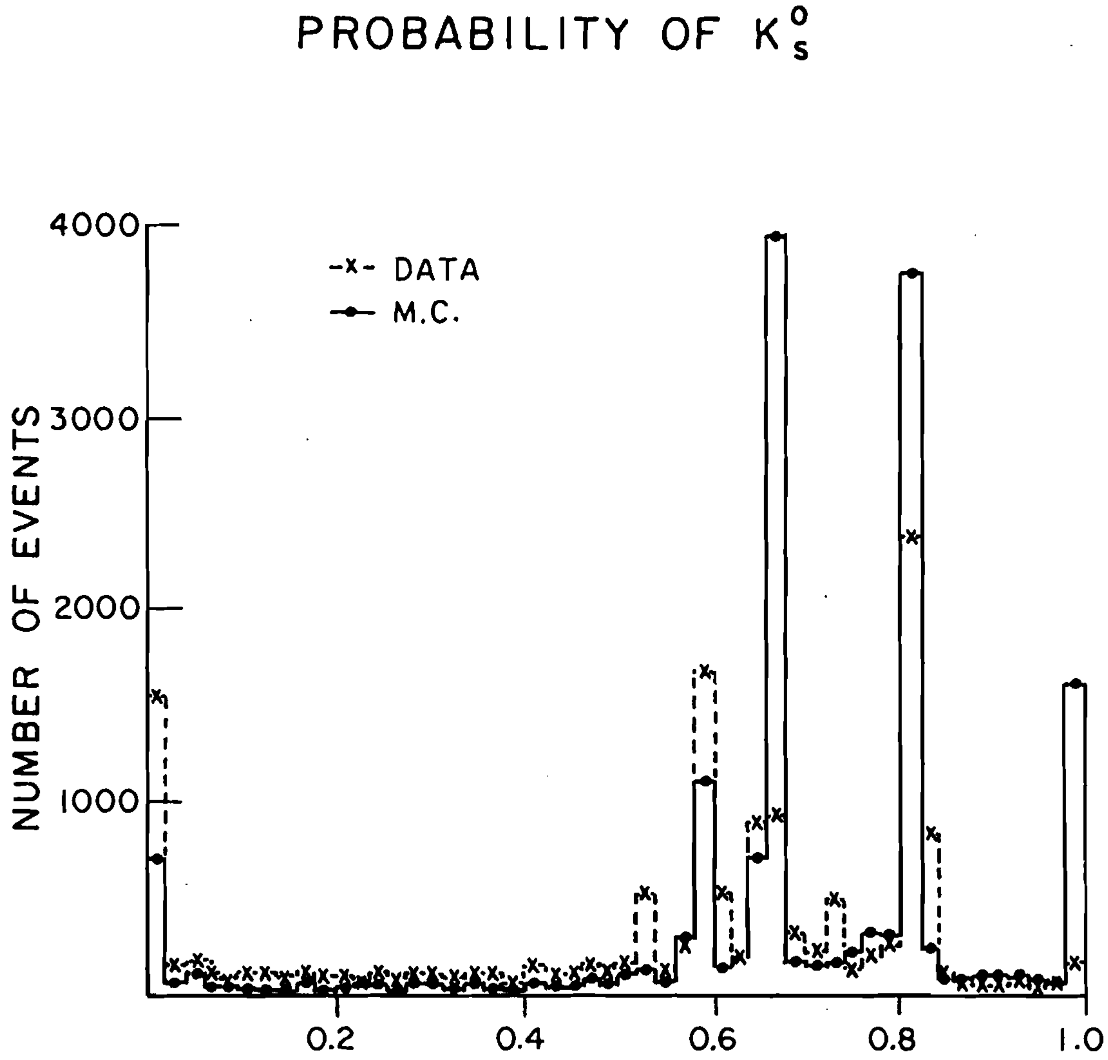

Figure 5.13 Cherenkov probability of neutral kaons.

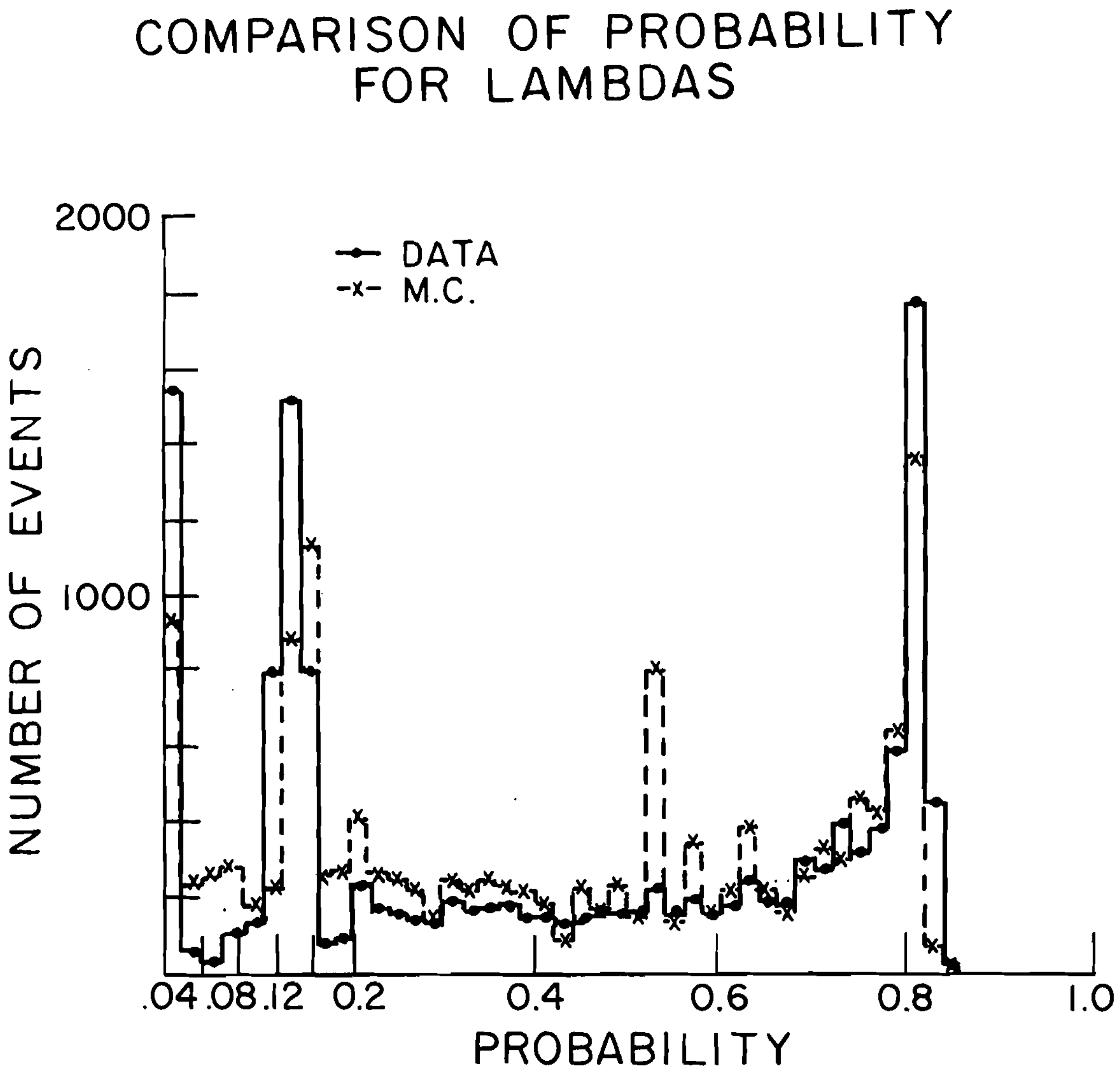

Figure 5.14 Cherenkov probability for lambdas.

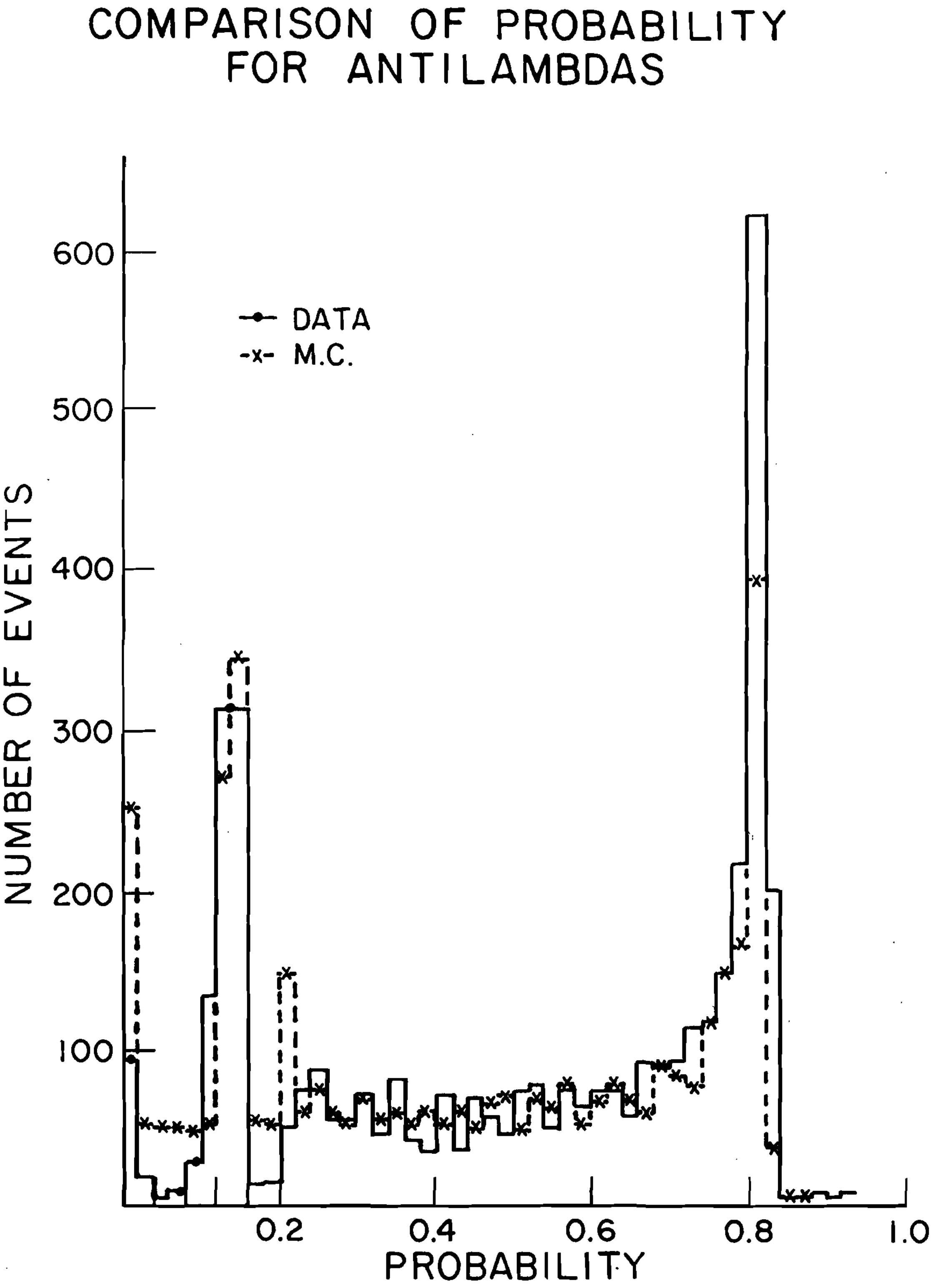

Figure 5.15 Cherenkov probability for antilambdas.

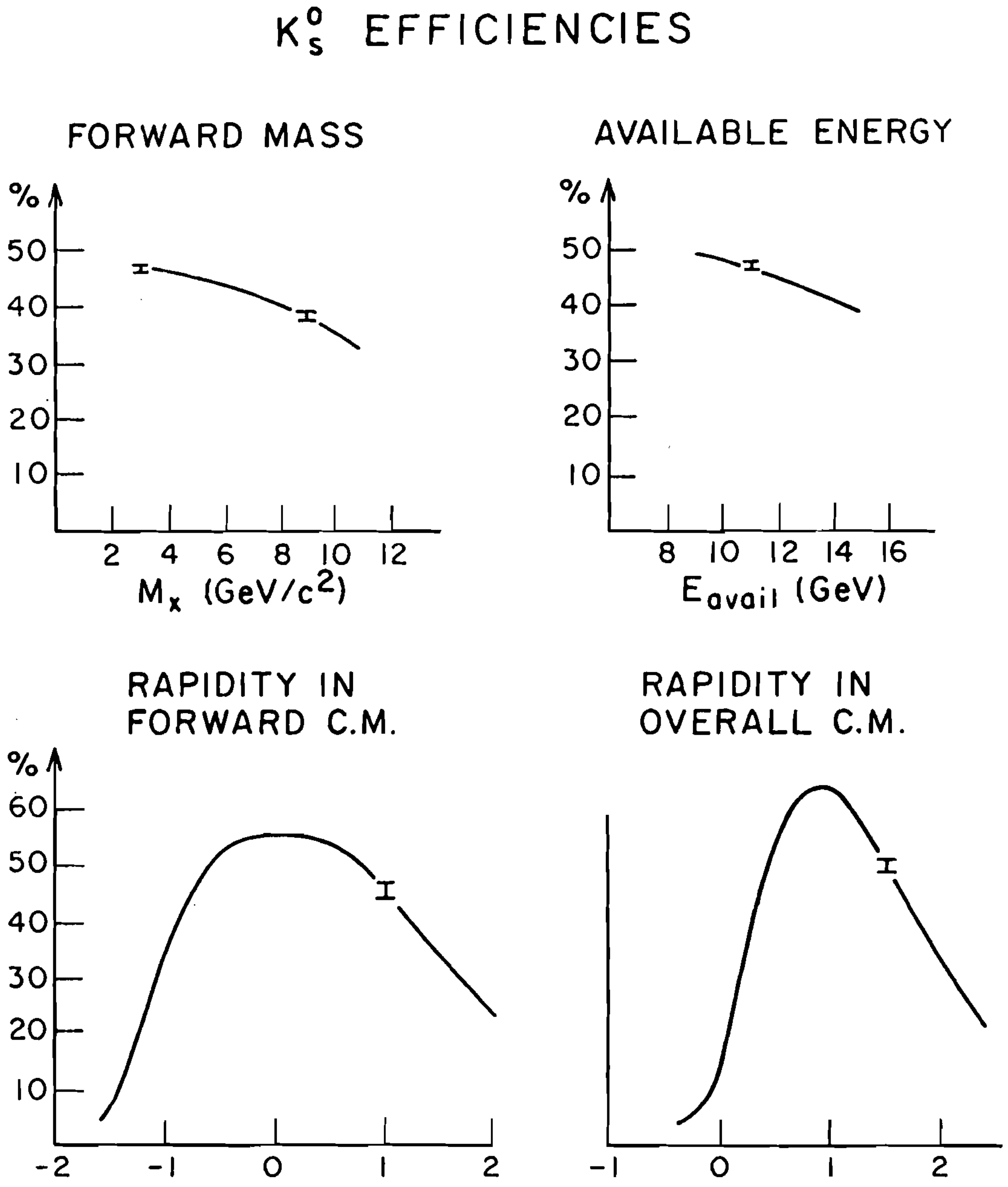

Figure 5.16 Neutral kaon efficiencies in terms of the forward mass, the available energy, the rapidity in the overall centre of mass and the forward centre of mass.

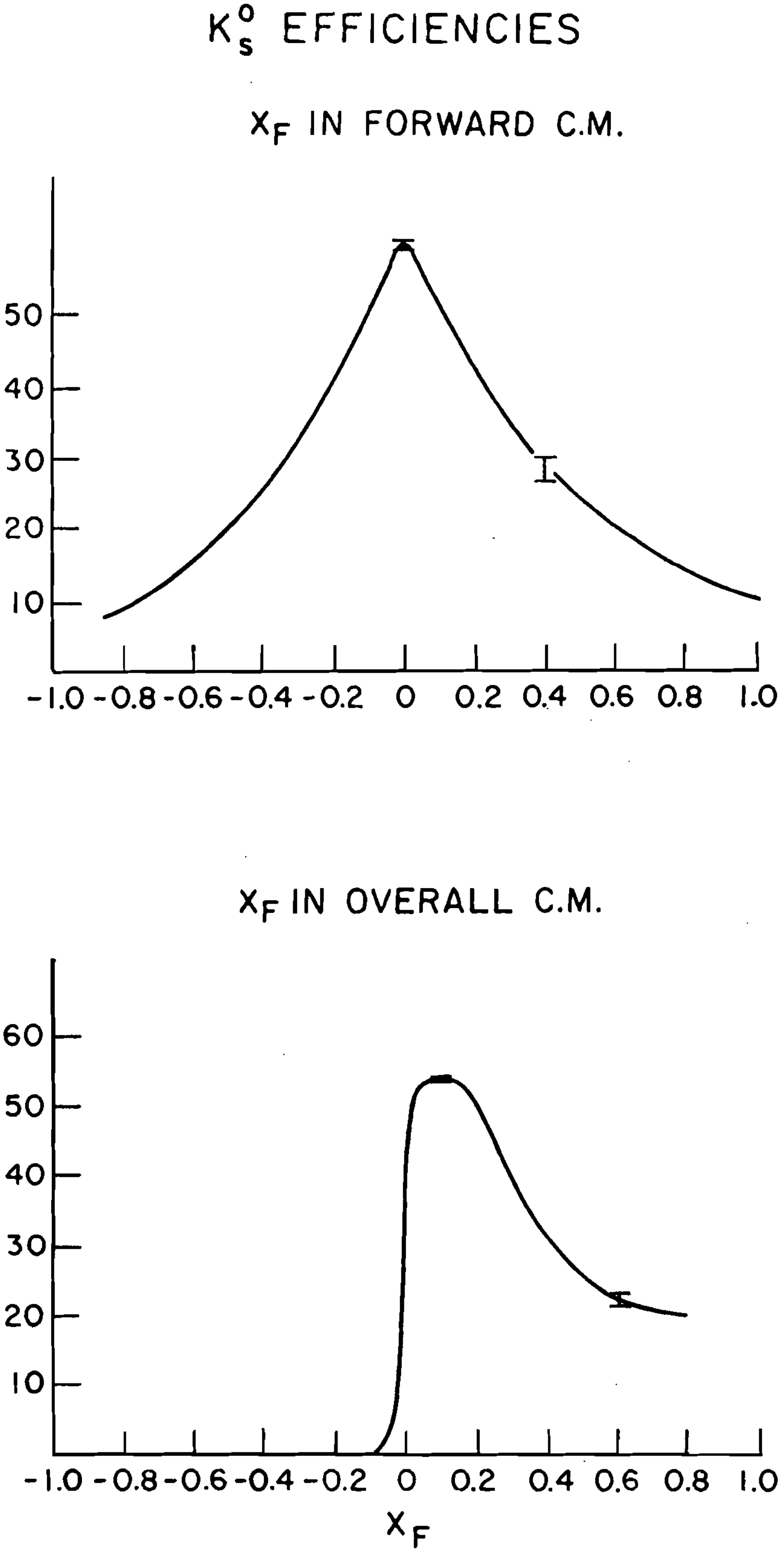

Figure 5.17 Neutral kaon efficiencies in terms of the Feynman X in the forward centre of mass and the overall centre of mass.

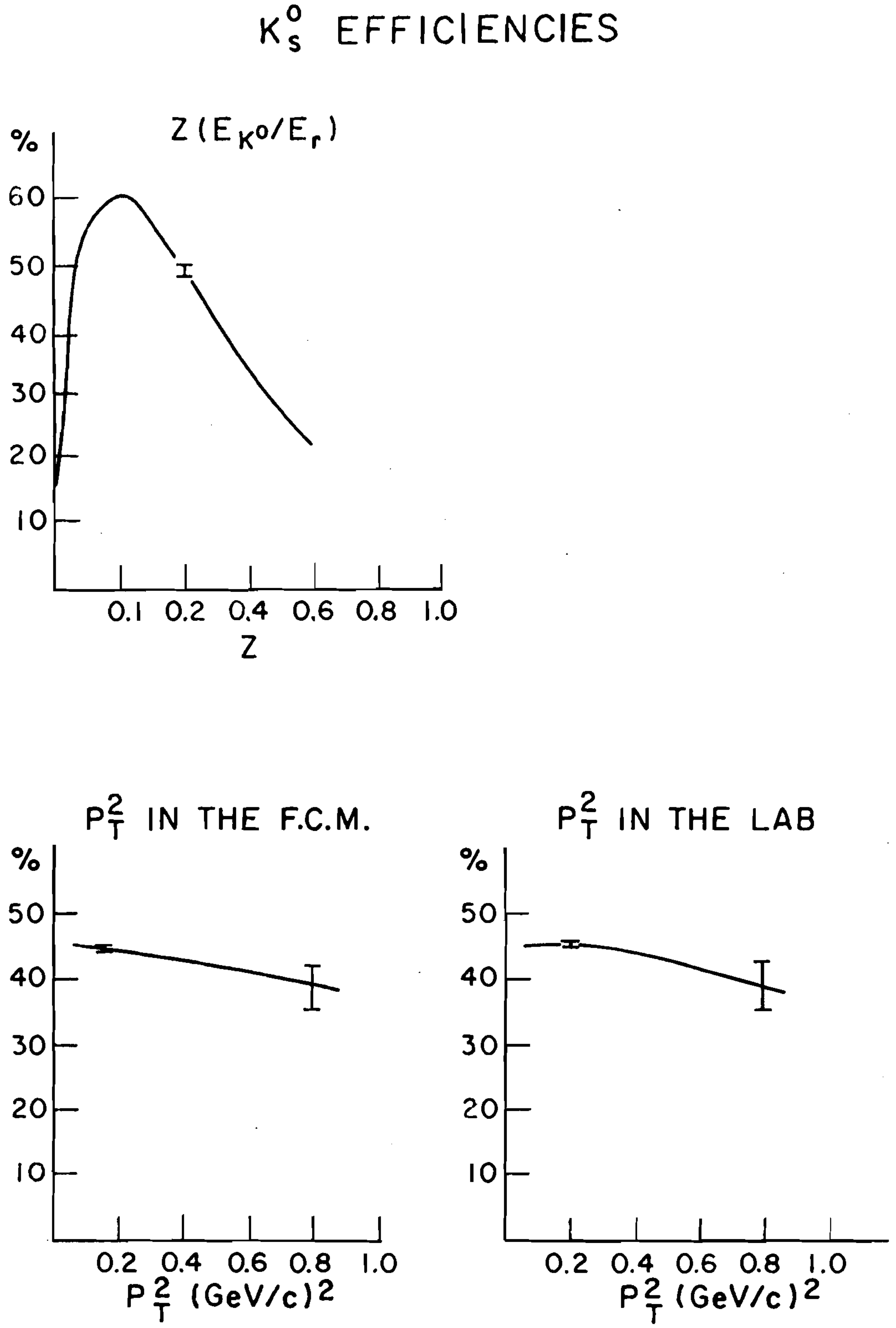

Figure 5.18 Neutral kaon efficiencies in terms of the Z value and the transverse momentum in forward centre of mass and the lab.

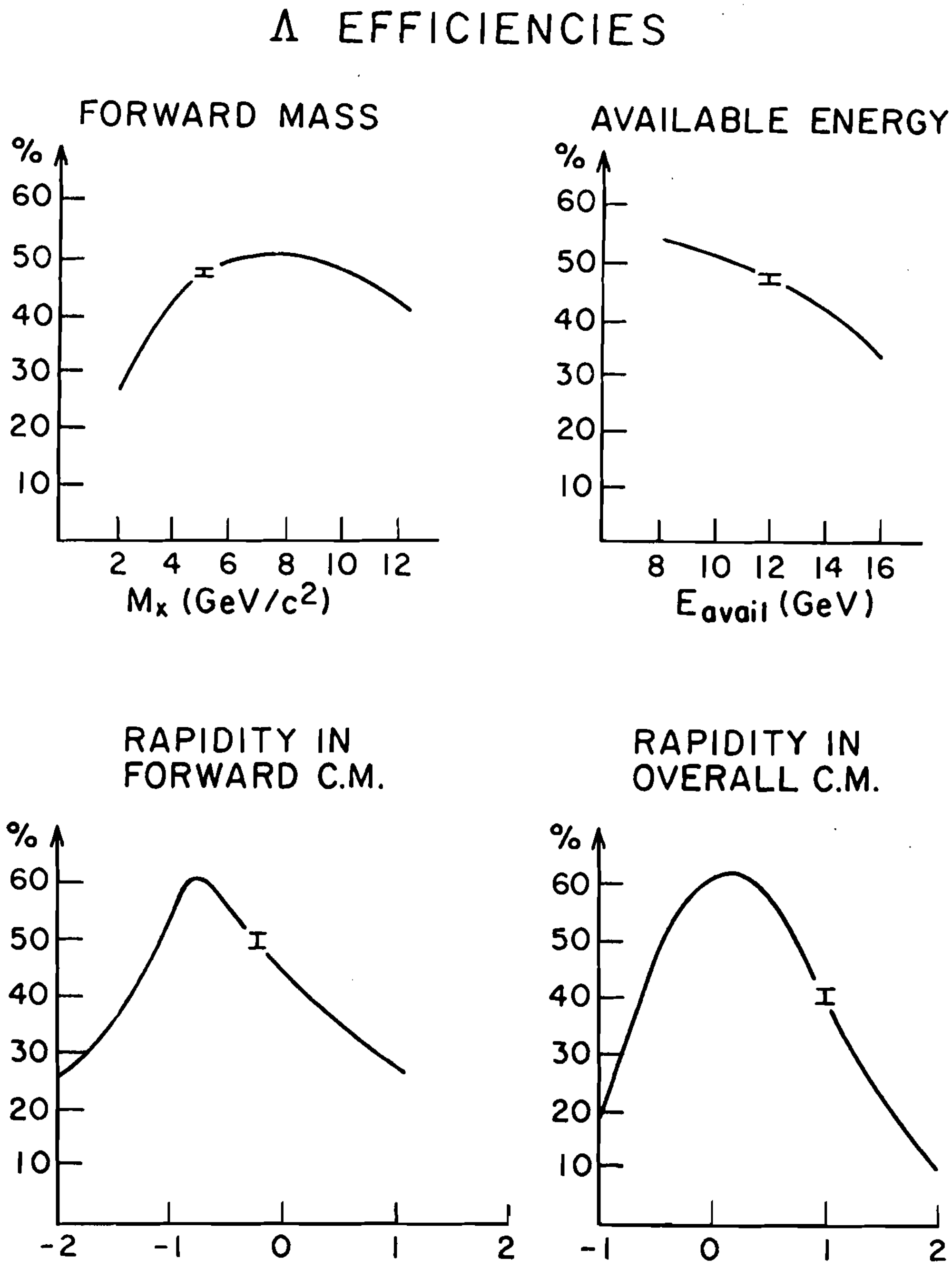

Figure 5.19 Lambda efficiencies in terms of the forward mass, the available energy, the rapidity in the overall centre of mass and the forward centre of mass.

Λ EFFICIENCIES

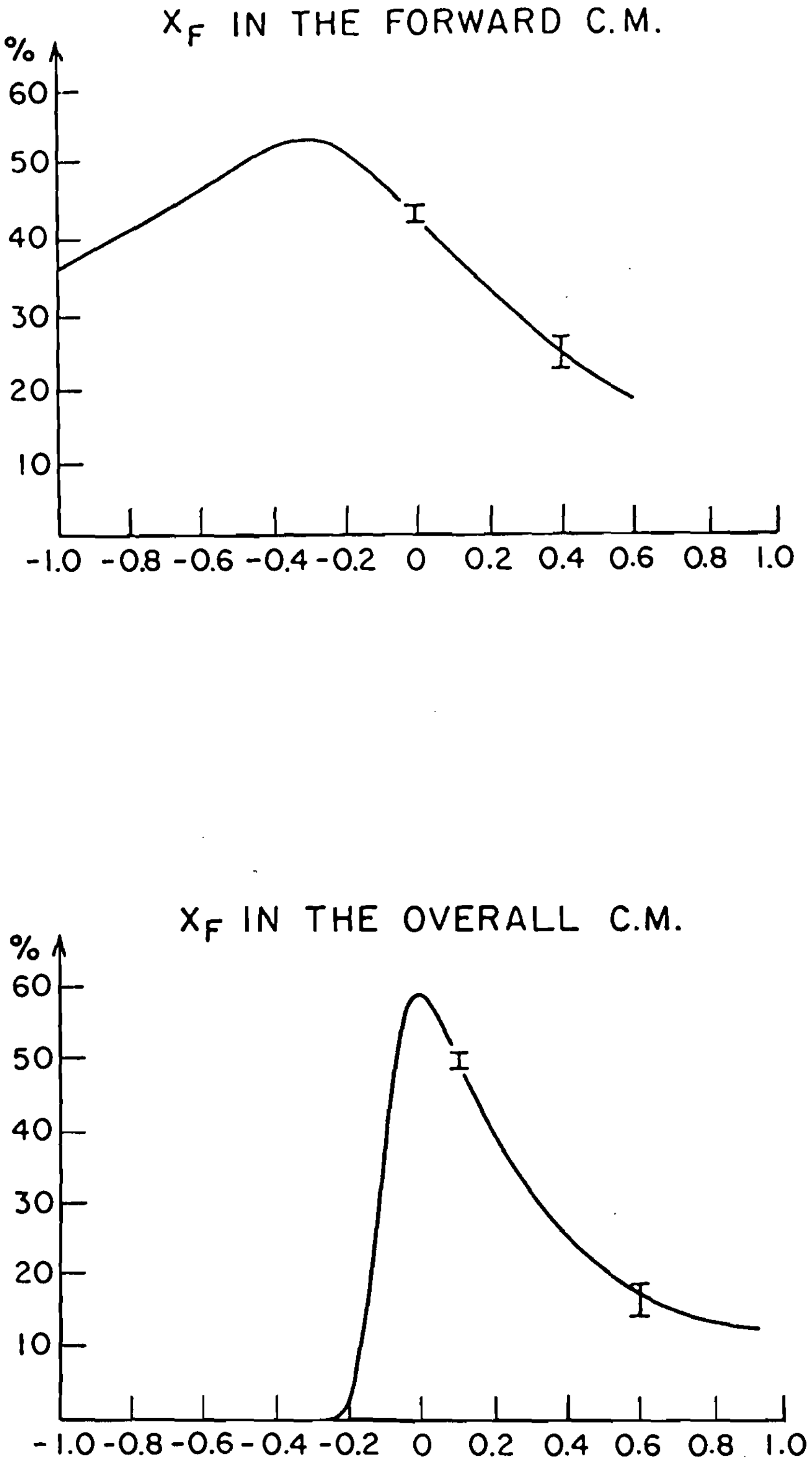

Figure 5.20 Lambda efficiencies in terms of the Feynman X in the forward and overall centre of mass.

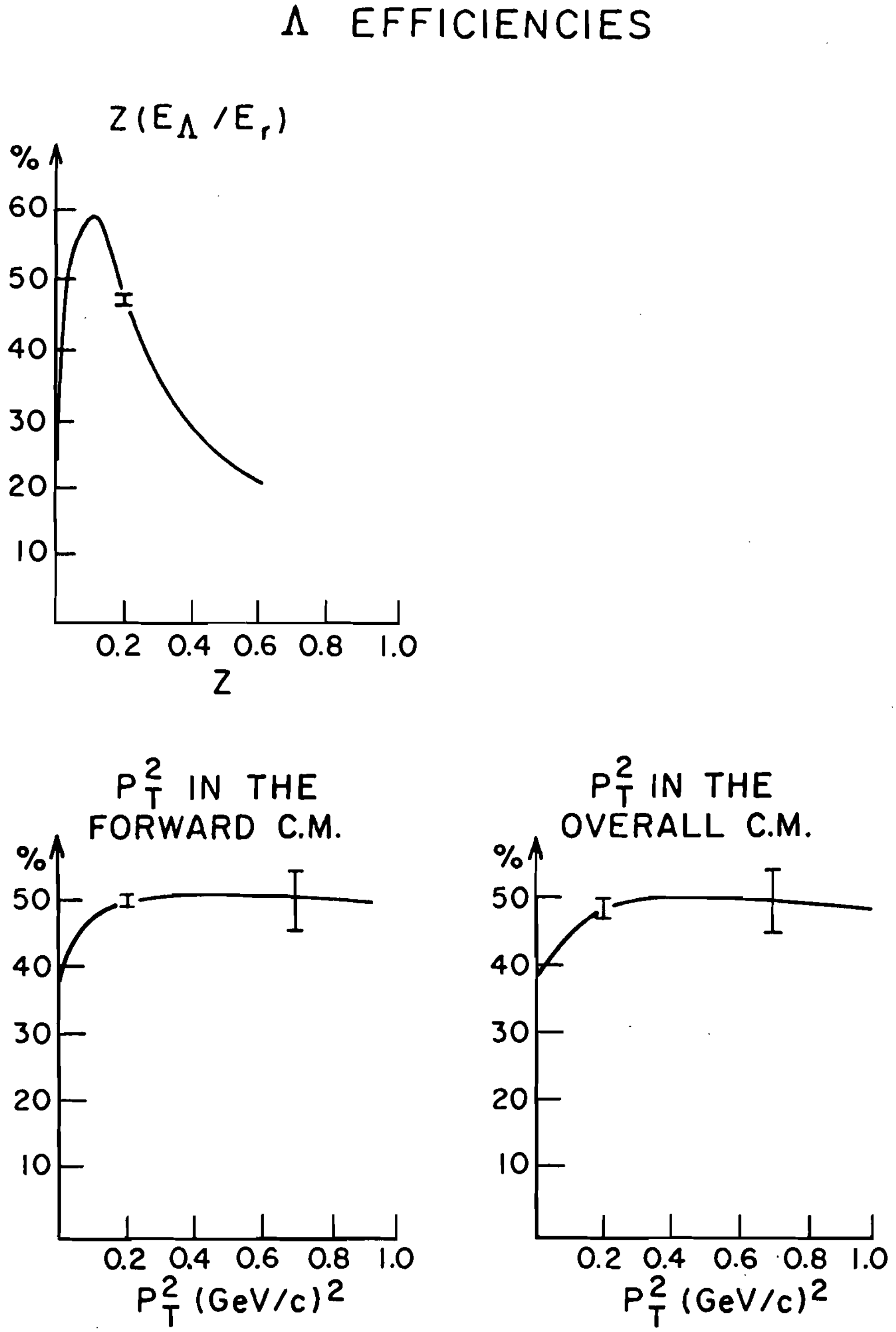

Figure 5.21 Lambda efficiencies in terms of the Z value and the transverse momentum in the forward centre of mass and the lab.

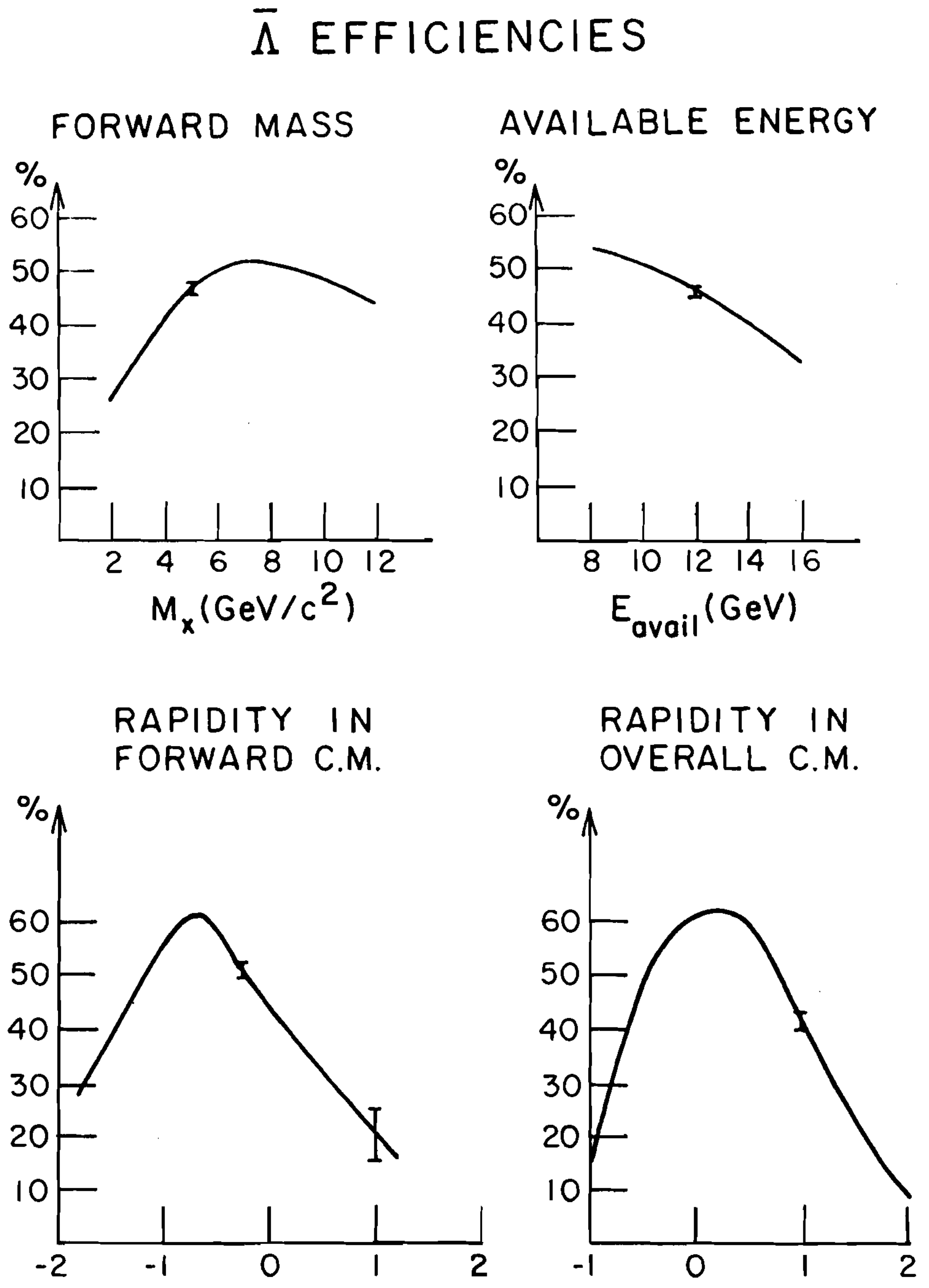

Figure 5.22 Antilambda efficiencies in terms of the forward mass, the available energy, the rapidity in the overall centre of mass and the forward centre of mass.

$\bar{\Lambda}$ EFFICIENCIES

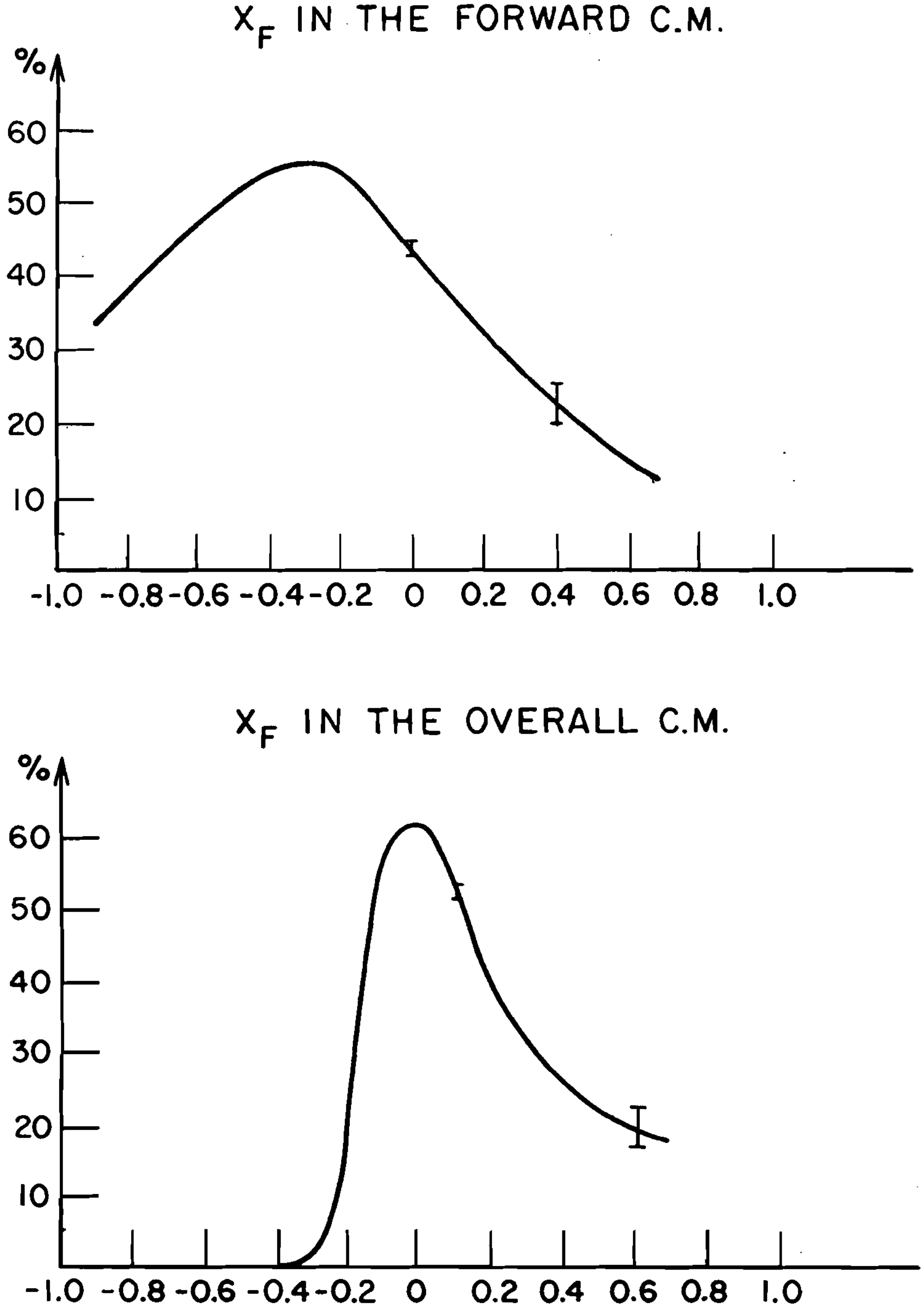

Figure 5.23 Antilambda efficiencies in terms of the Feynman X in the forward and overall centre of mass.

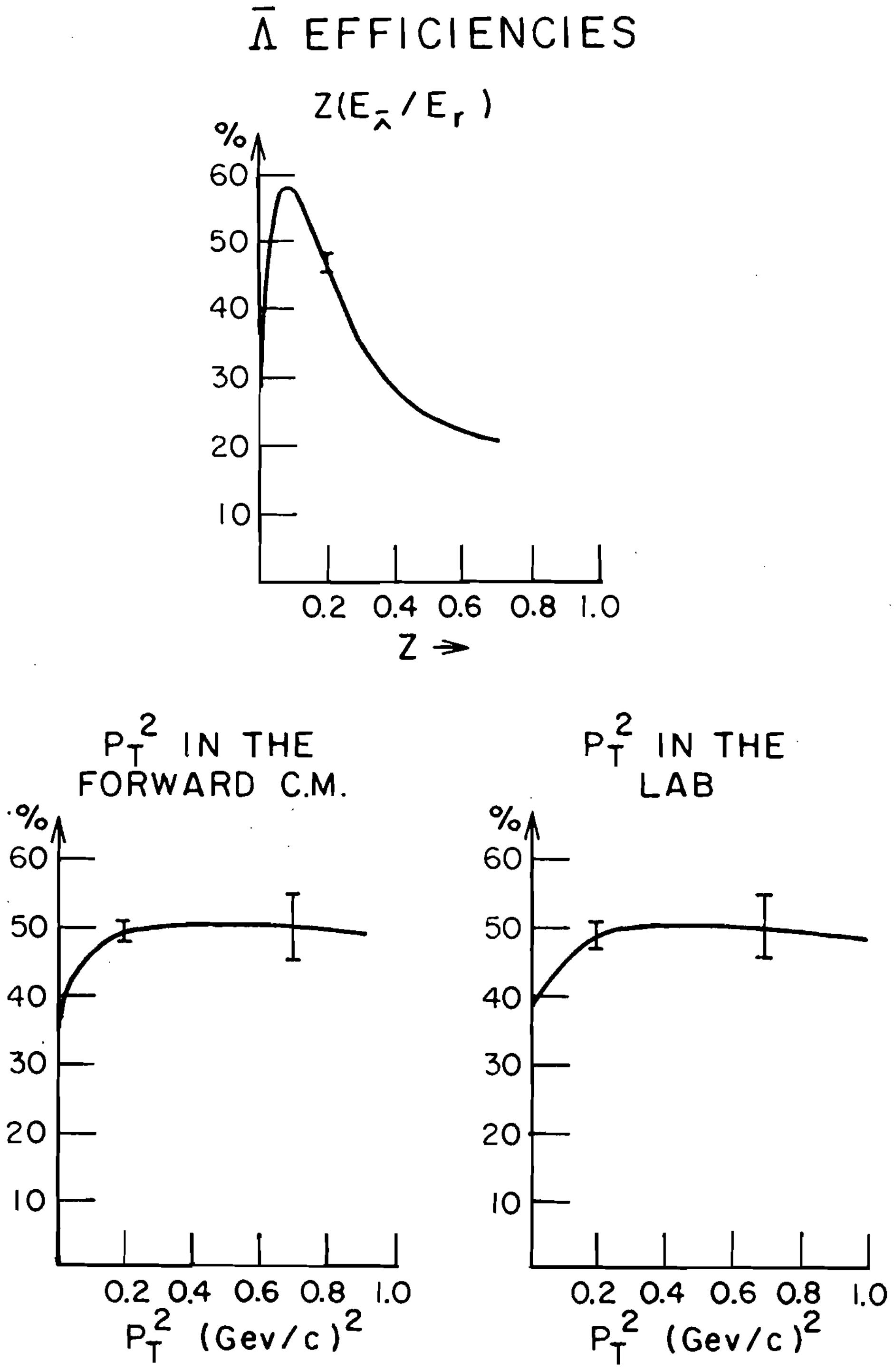

$\bar{\Lambda}$ EFFICIENCIES

$Z(E_{\bar{\Lambda}}/E_r)$

P_T^2 IN THE FORWARD C.M.

P_T^2 IN THE LAB

Figure 5.24 Antilambda efficiencies in terms of the Z value and the transverse momentum in the forward centre of mass and the lab.

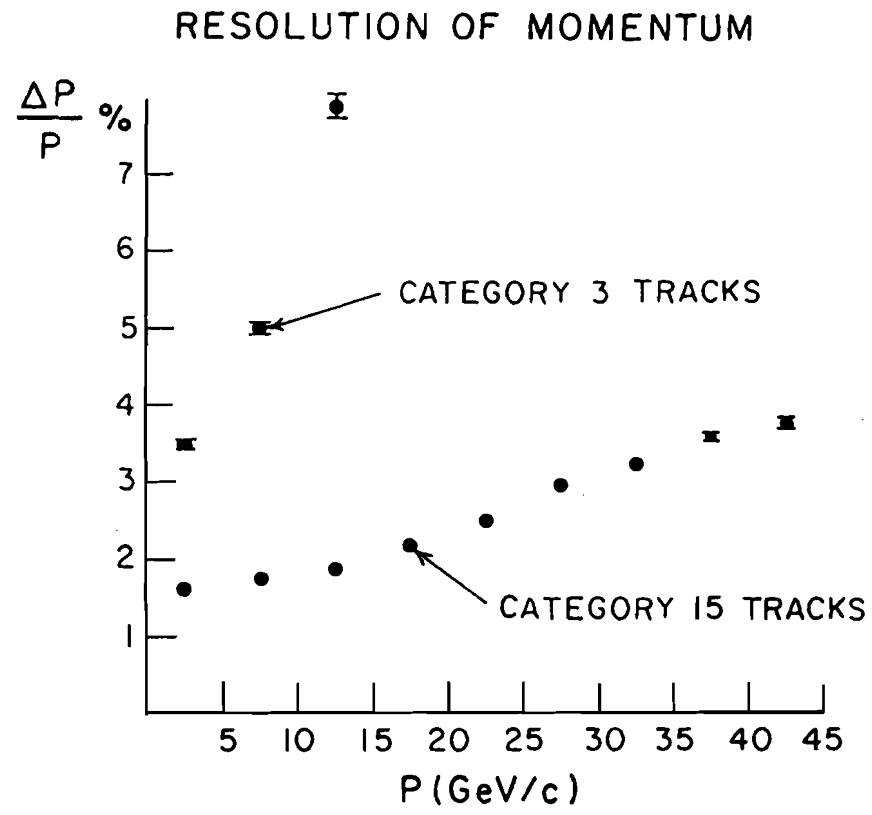

Figure 5.25

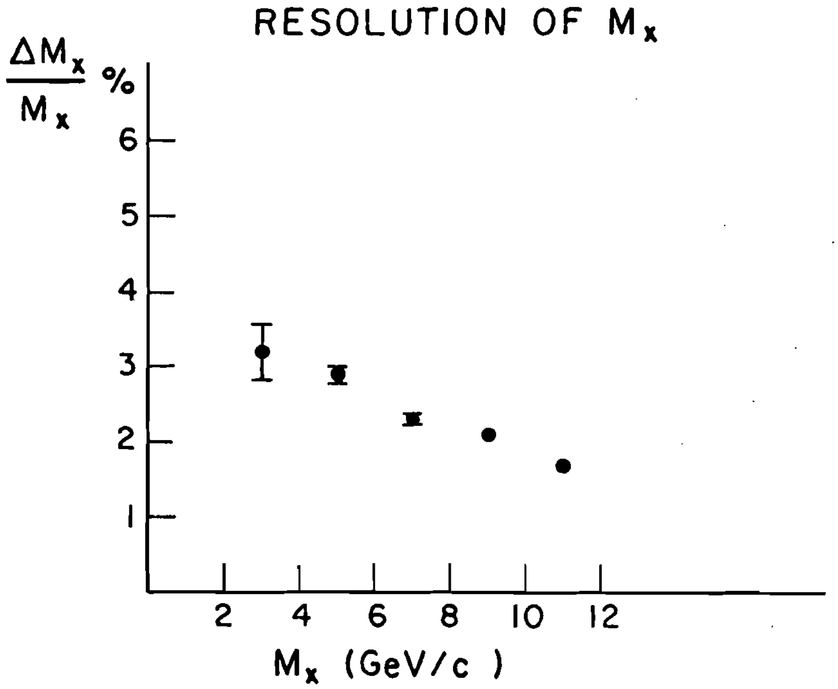

Figure 5.26

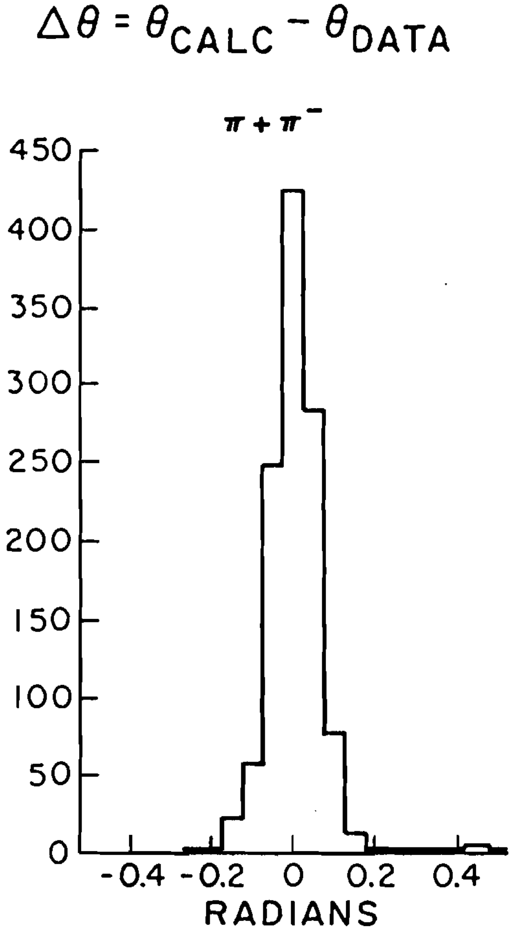

Figure 6.1 Difference in the angle of the recoil proton (calculated minus data).

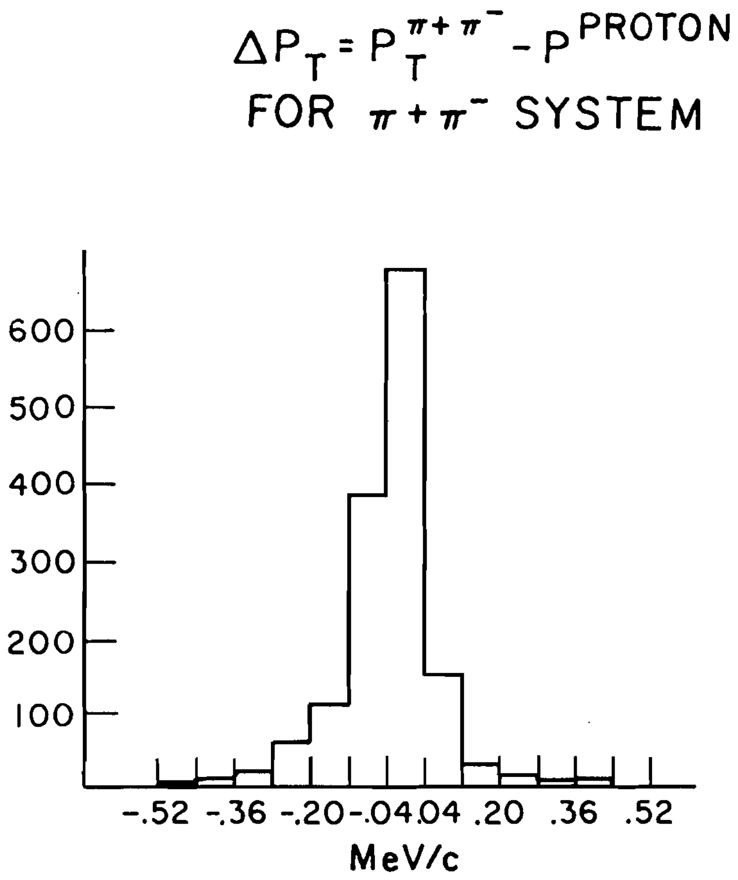

Figure 6.2 Difference in the transverse momentum (calculated minus data).

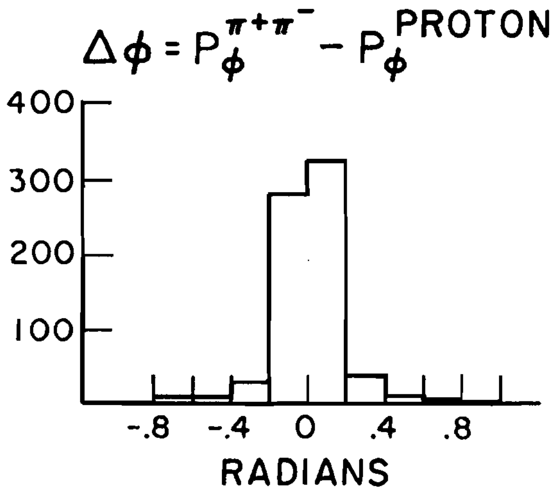

Figure 6.3 Difference in the azimuthal angle (calculated minus data).

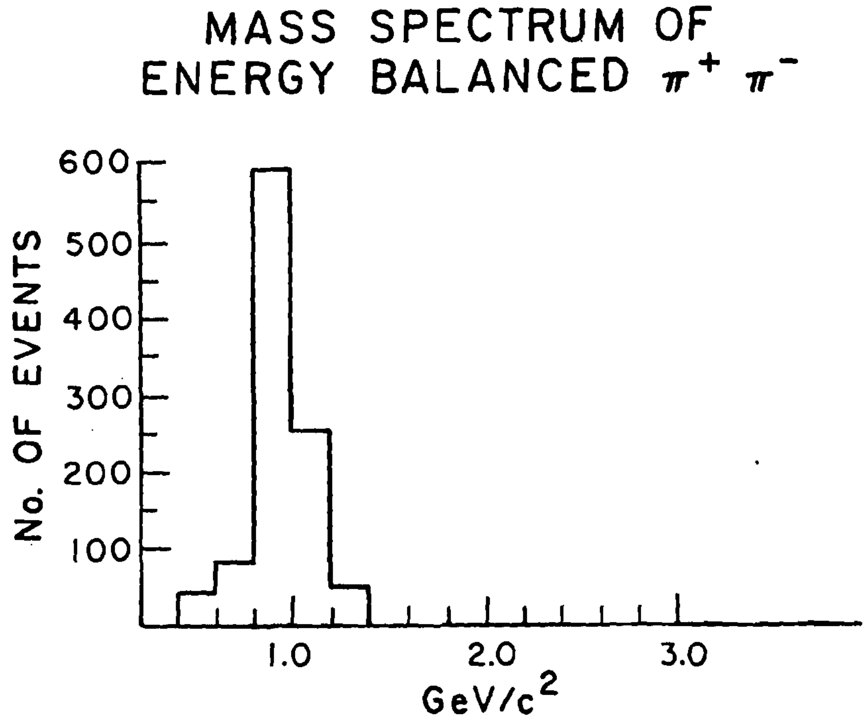

Figure 6.4 Invariant mass of two oppositely charged pions in the forward detector.

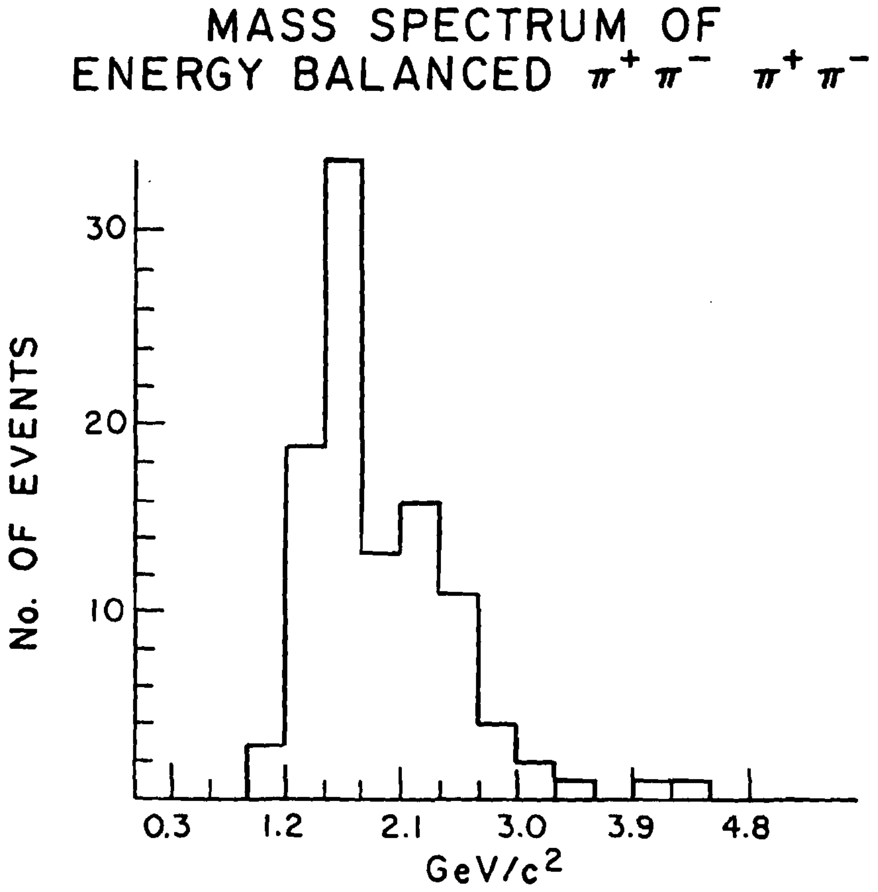

Figure 6.5 Invariant mass of four charged pions in the forward detector.

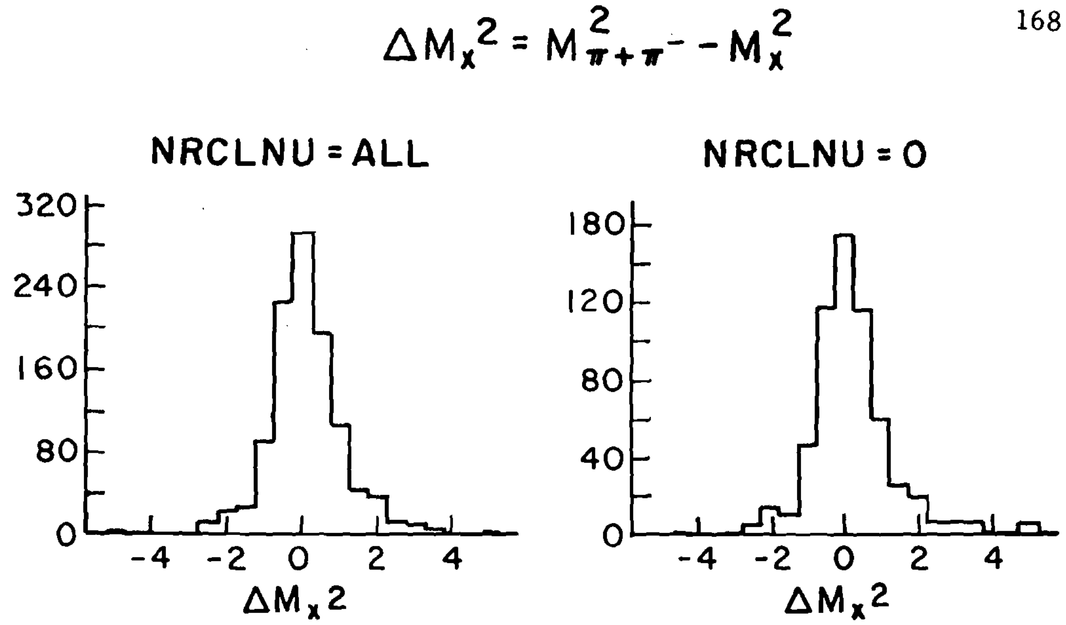

a.) b.)

Figure 6.6 Difference of the square of the mass from the recoil variables and the forward system for two charged tracks.

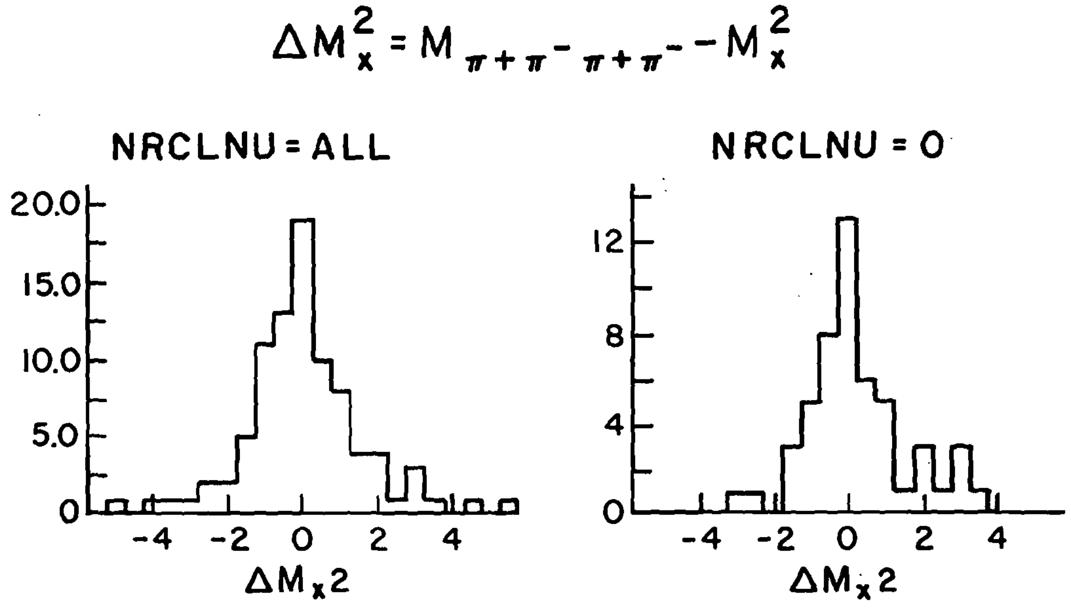

a.) b.)

Figure 6.7 Difference of the square of the mass from the recoil variables and the forward system for four charged tracks.

FORWARD MASS DISTRIBUTION

RECOIL 2+3 TRIGGERS
170 GeV

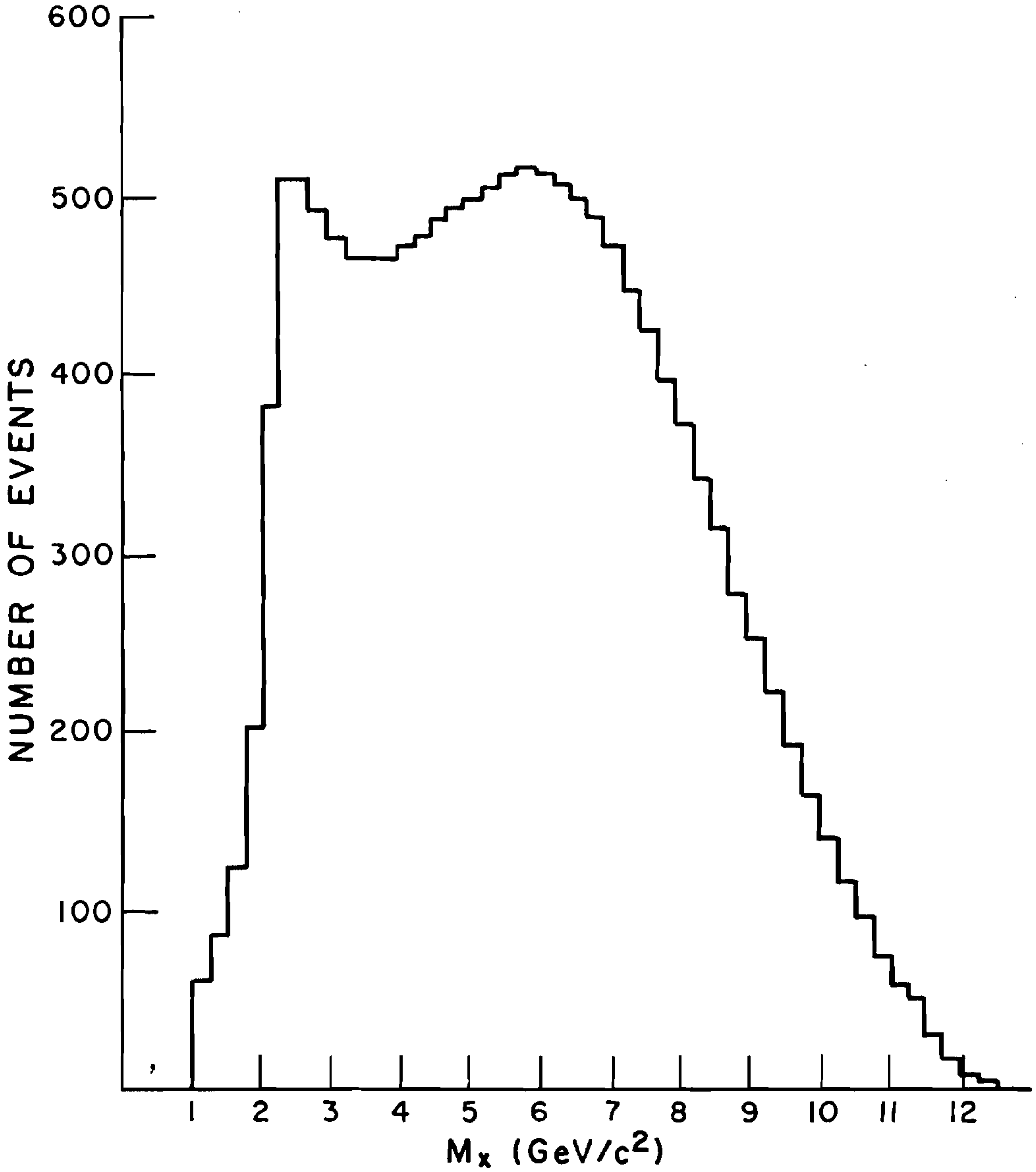

Figure 6.8

M_x FOR $\pi^+\pi^-$ SYSTEM WHEN $.2 < M_\rho < 1.2$ GeV/c
$|E_\gamma - E_F| < .3E_\gamma$

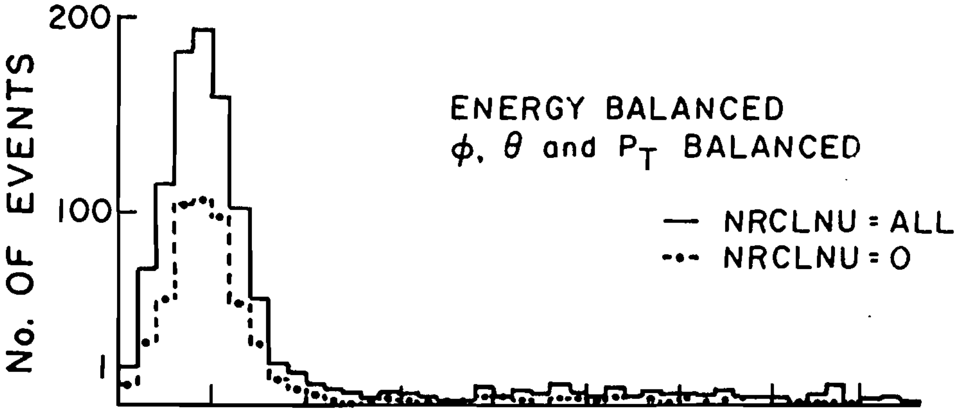

Figure 7.1a

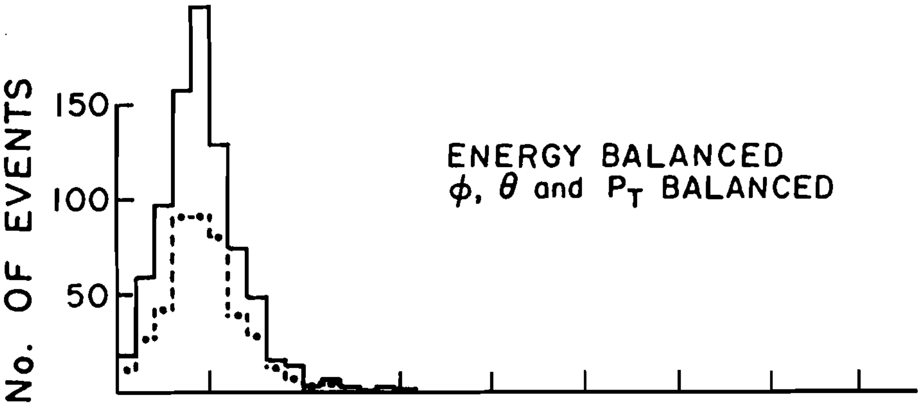

Figure 7.1b

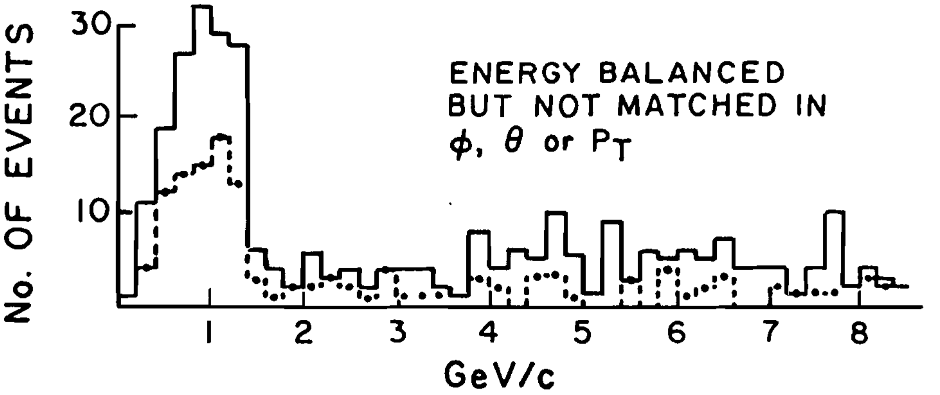

Figure 7.1c

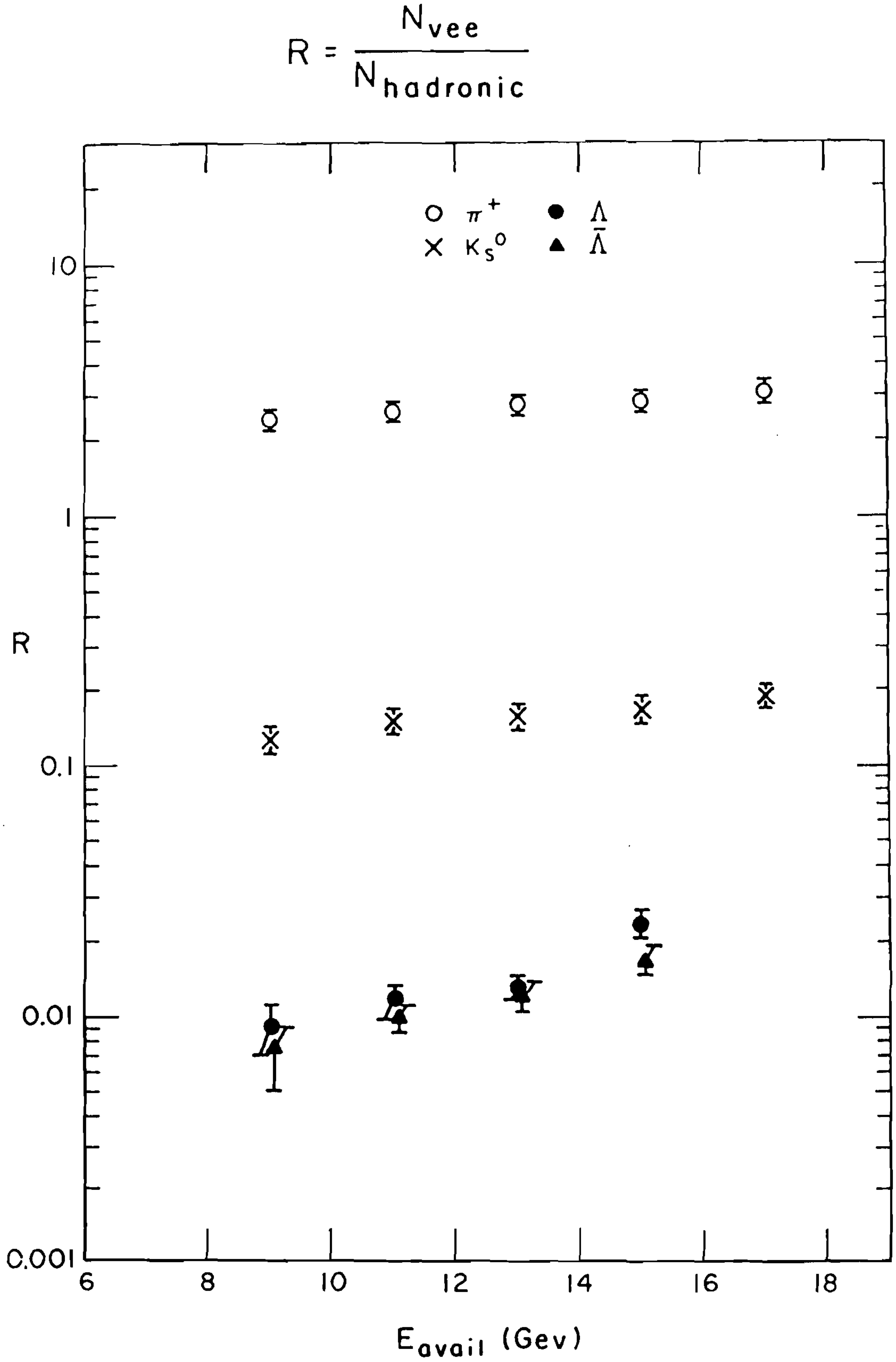

Figure 8.1a The yield of pions, neutral kaons, lambdas and antilambdas per hadronic event in terms of the available energy.

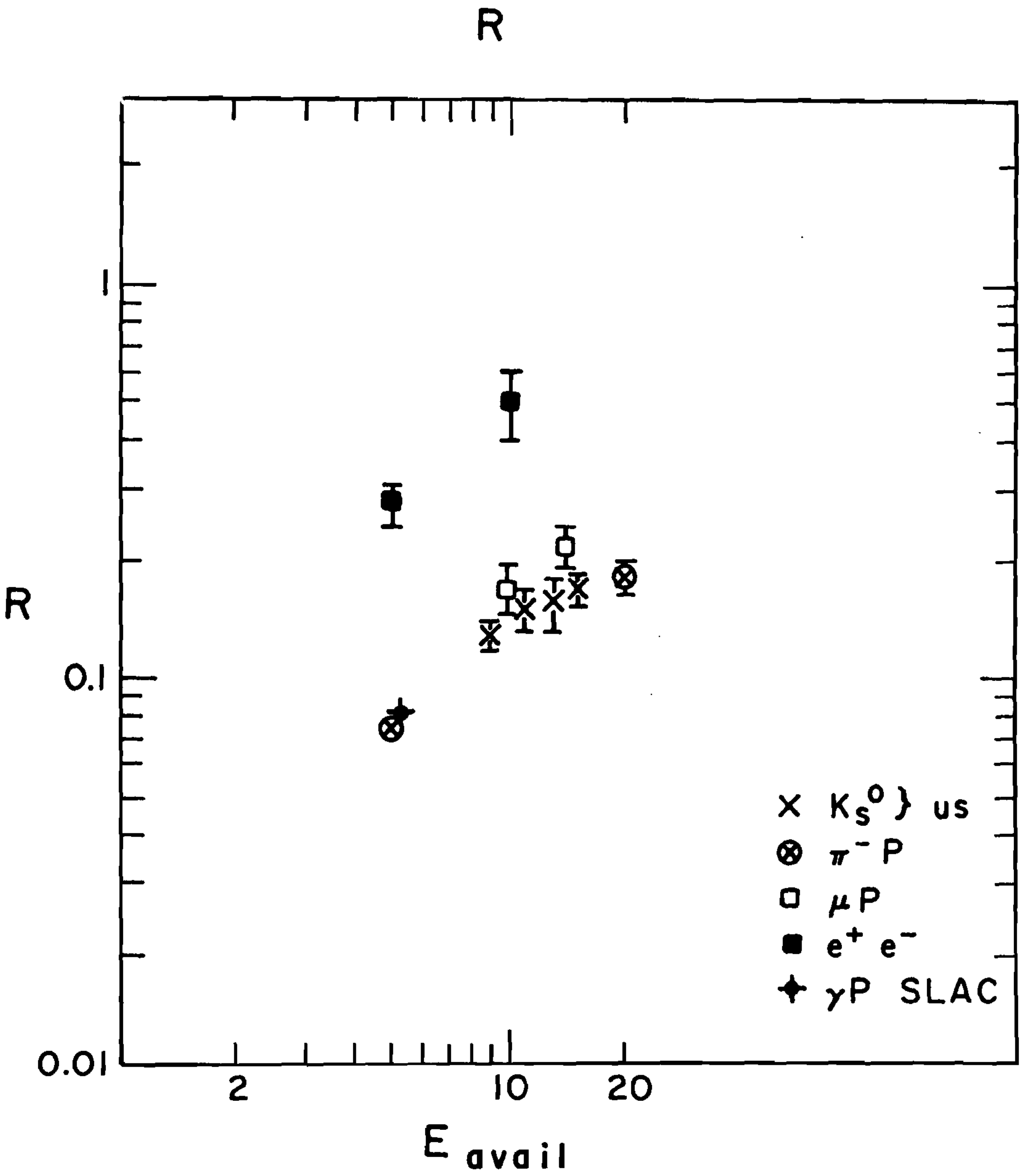

Figure 8.1b Comparison of the yield of neutral kaons per hadronic event with other experiments.

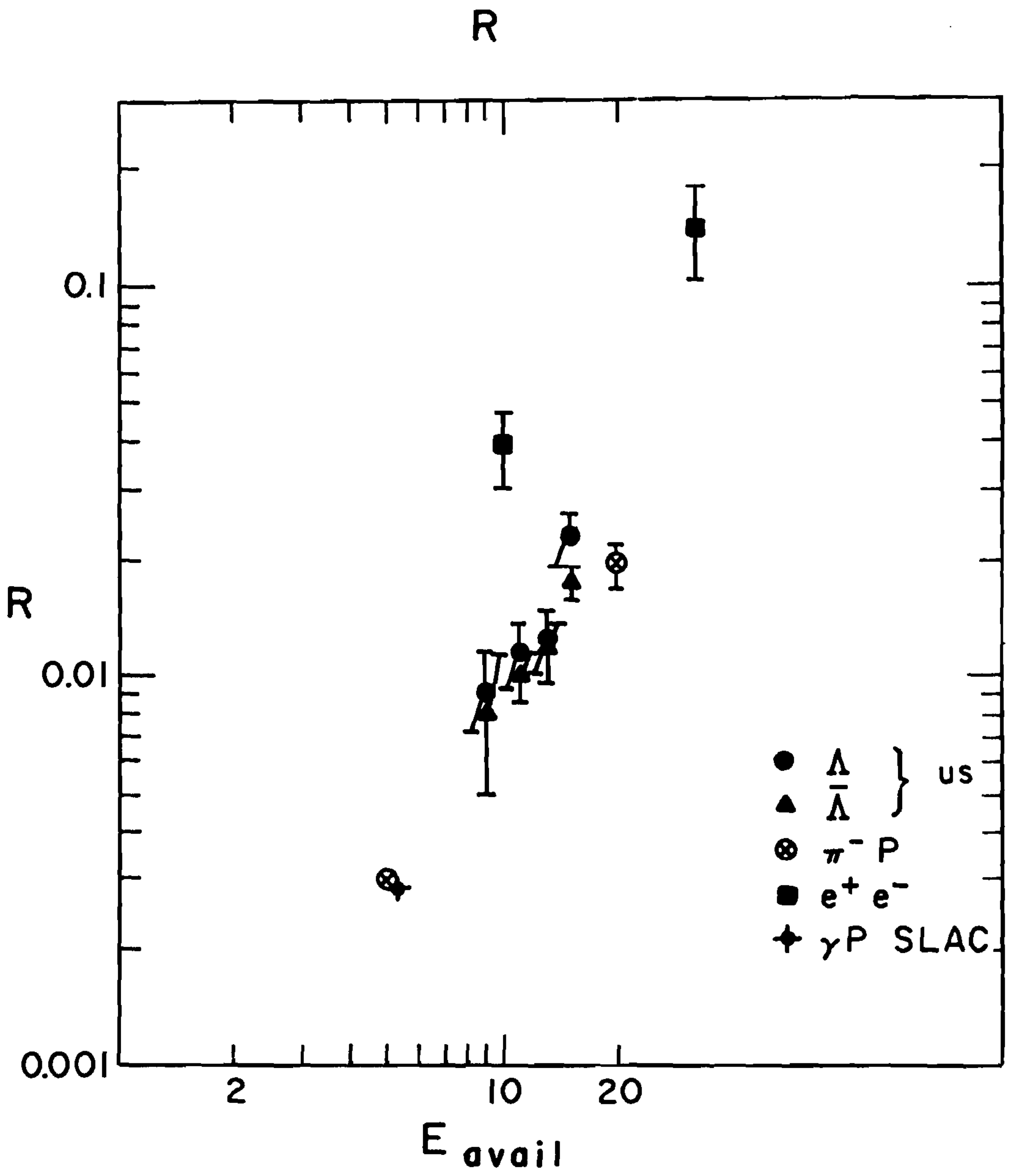

Figure 8.1c Comparison of the yield of lambdas and antilambdas per hadronic event with other experiments.

$$R = \frac{\text{NUMBER OF } \pi/K_s^0/\Lambda/\bar{\Lambda}}{\text{NUMBER OF HADRONIC EVENTS}}$$

AS A FUNCTION OF M_x

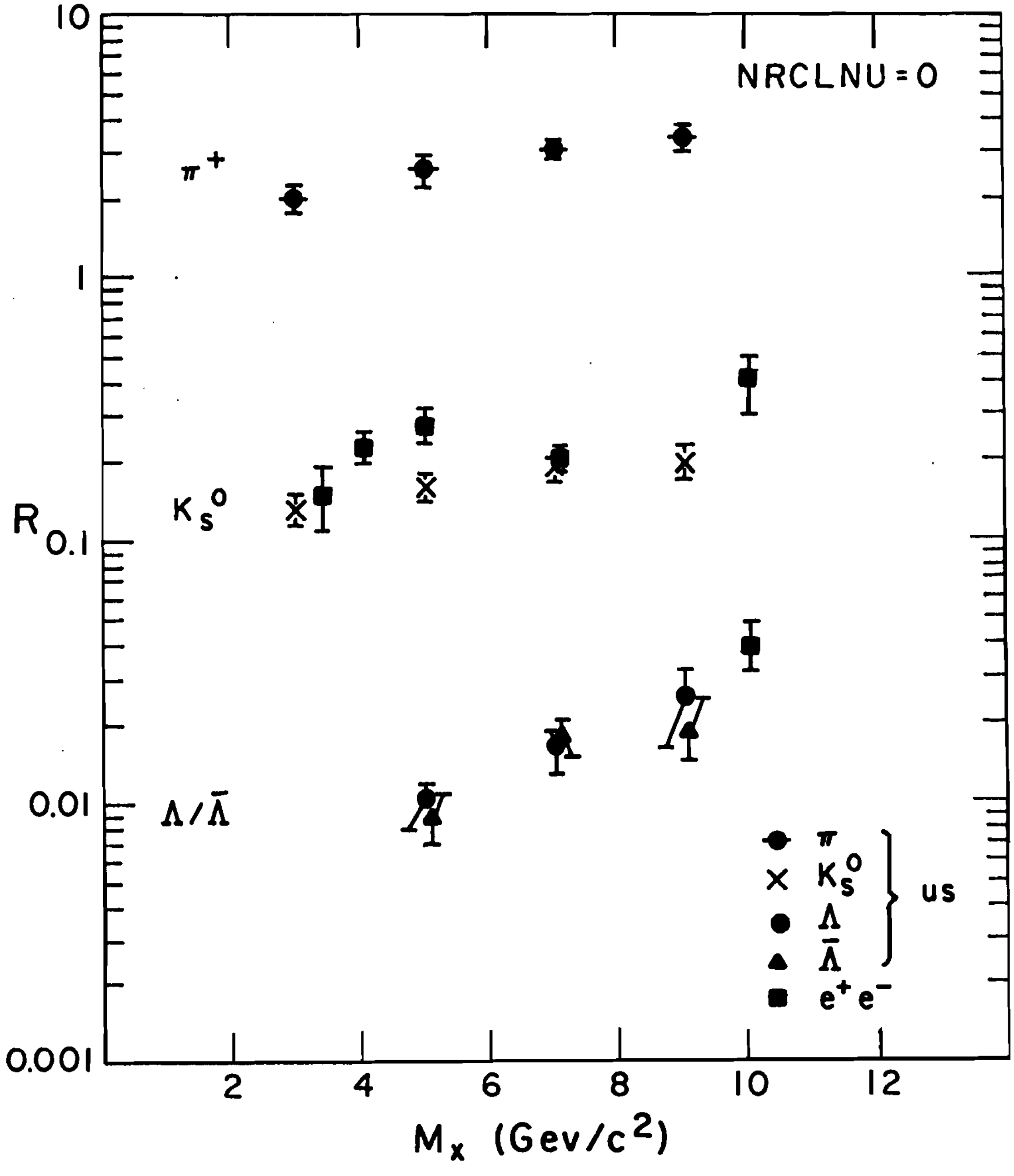

Figure 8.2 The yield of pions, neutral kaons, lambdas, and antilambdas per hadronic event with no detected neutrals in the recoil detector.

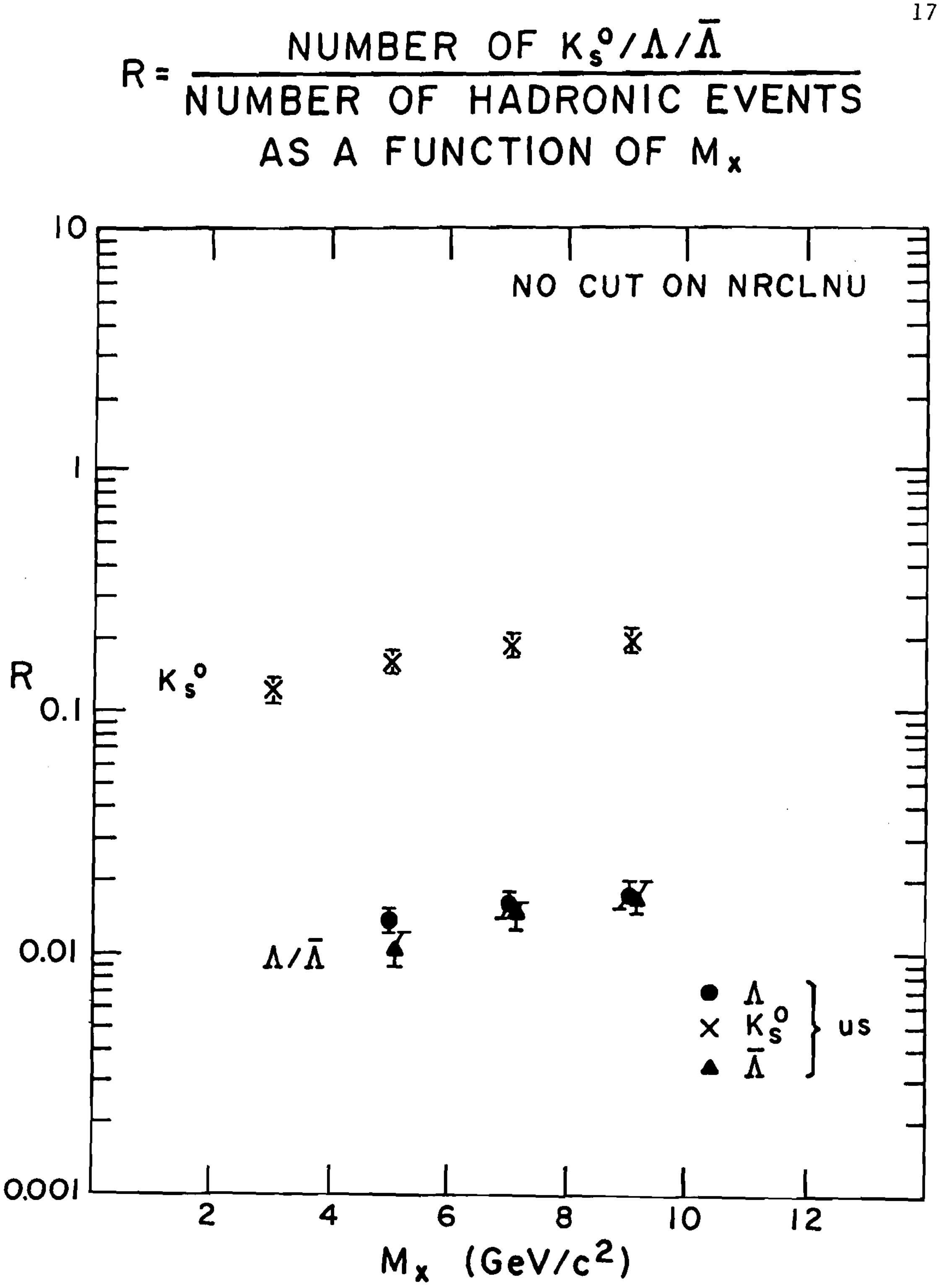

Figure 8.3 The yield of neutral kaons, lambdas and antilambdas with no requirement on the number of neutrals in the recoil detector.

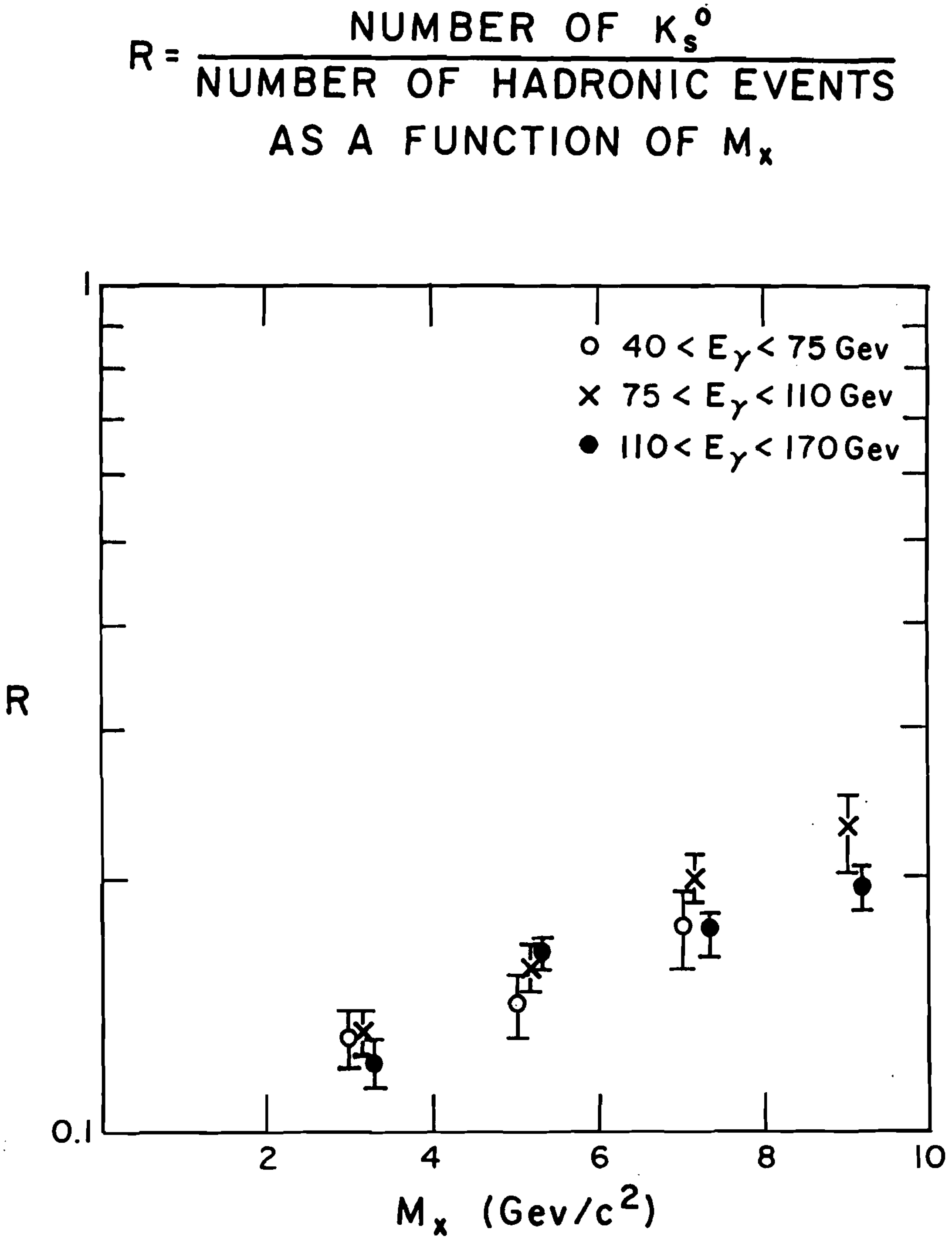

Figure 8.4 The yield per hadronic event of neutral kaons for three different photon energy range.

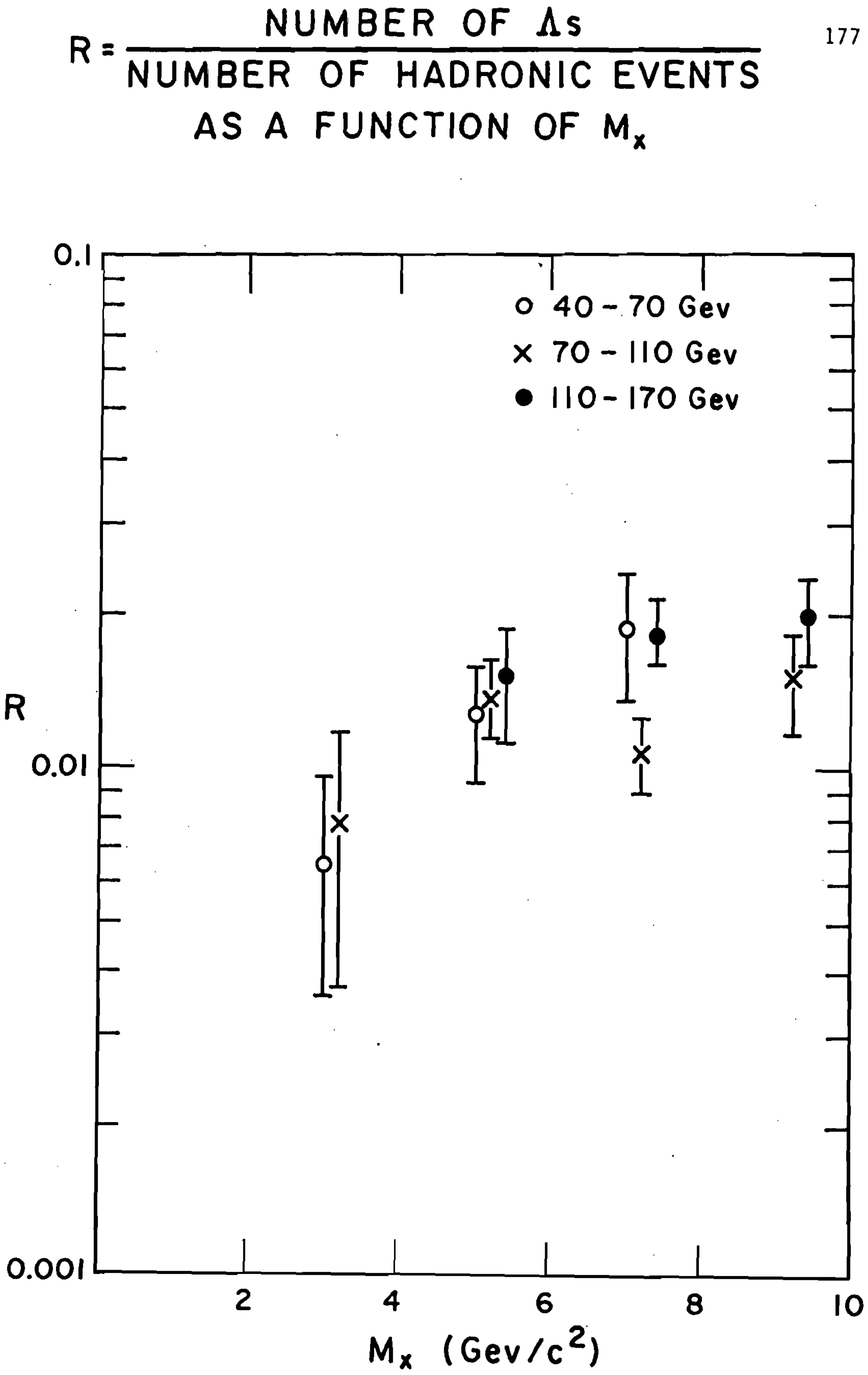

Figure 8.5 The yield per hadronic event of lambdas for three different photon energy ranges.

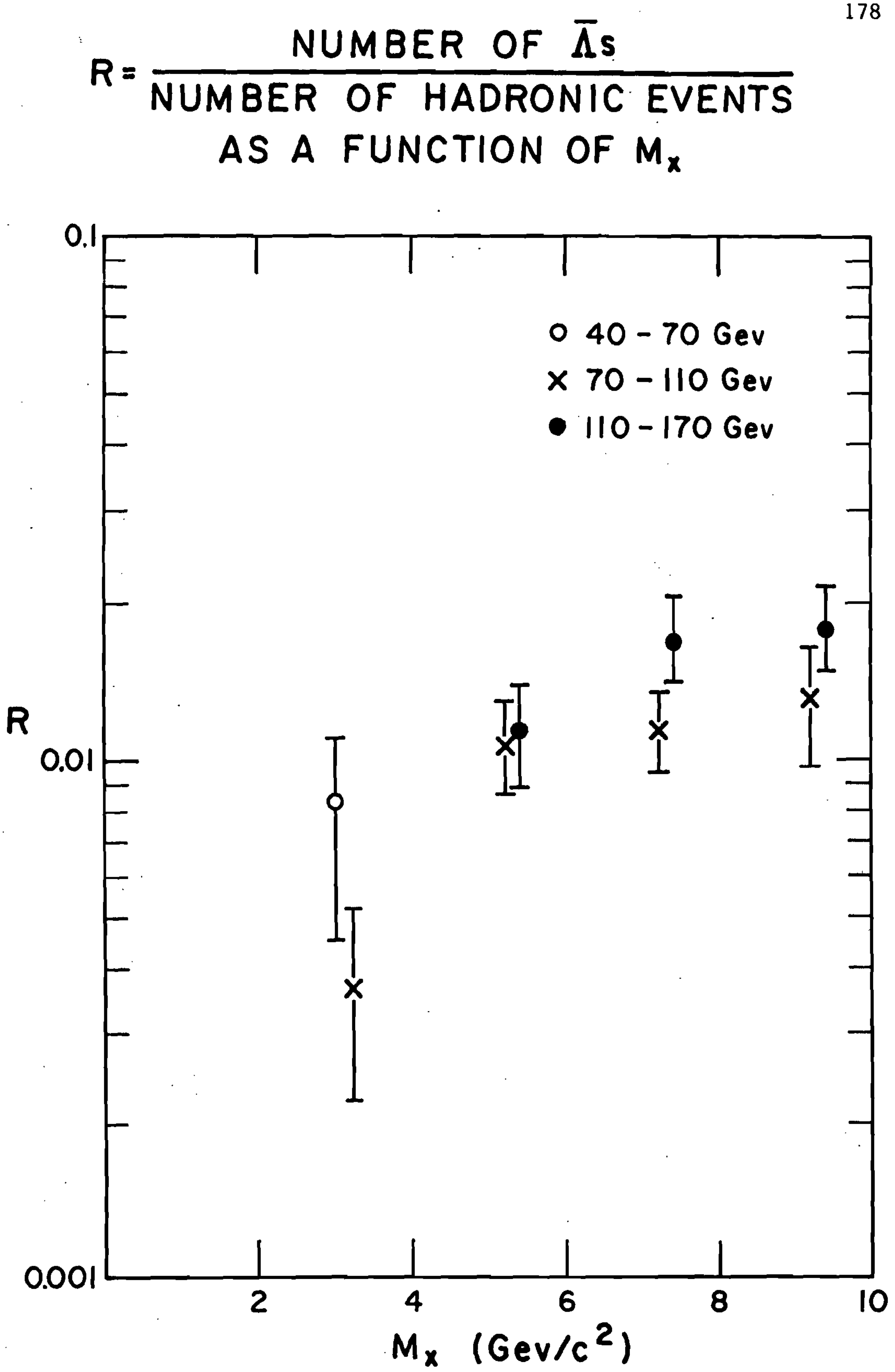

Figure 8.6 The yield per hadronic event of antilambdas for three different photon energy ranges.

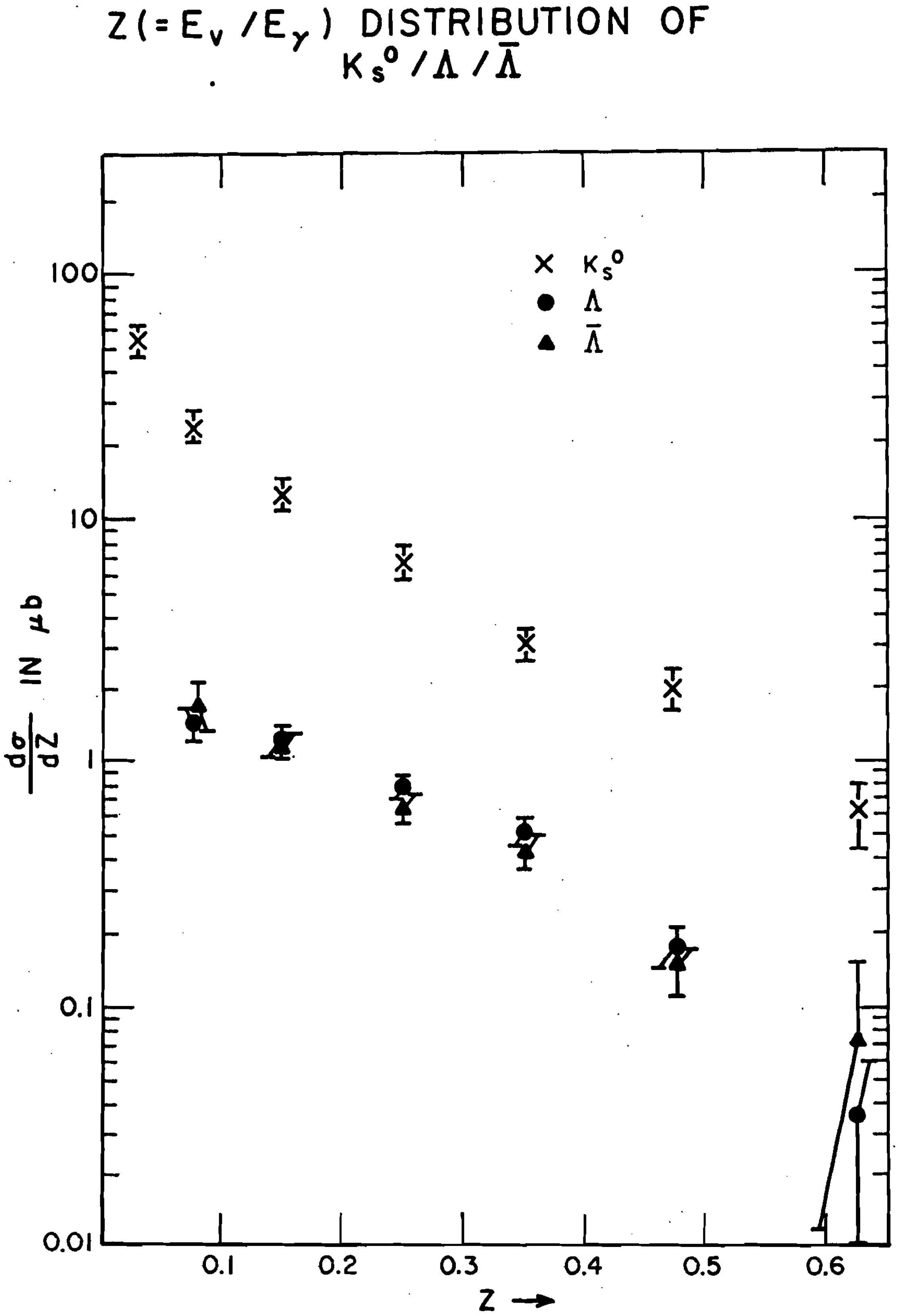

Figure 8.7 The differential cross section of the neutral kaons, lambdas and antilambdas as a function of Z.

FEYNMAN X DISTRIBUTION OF π^+ AND K_s^0 IN THE OVERALL CENTER OF MASS

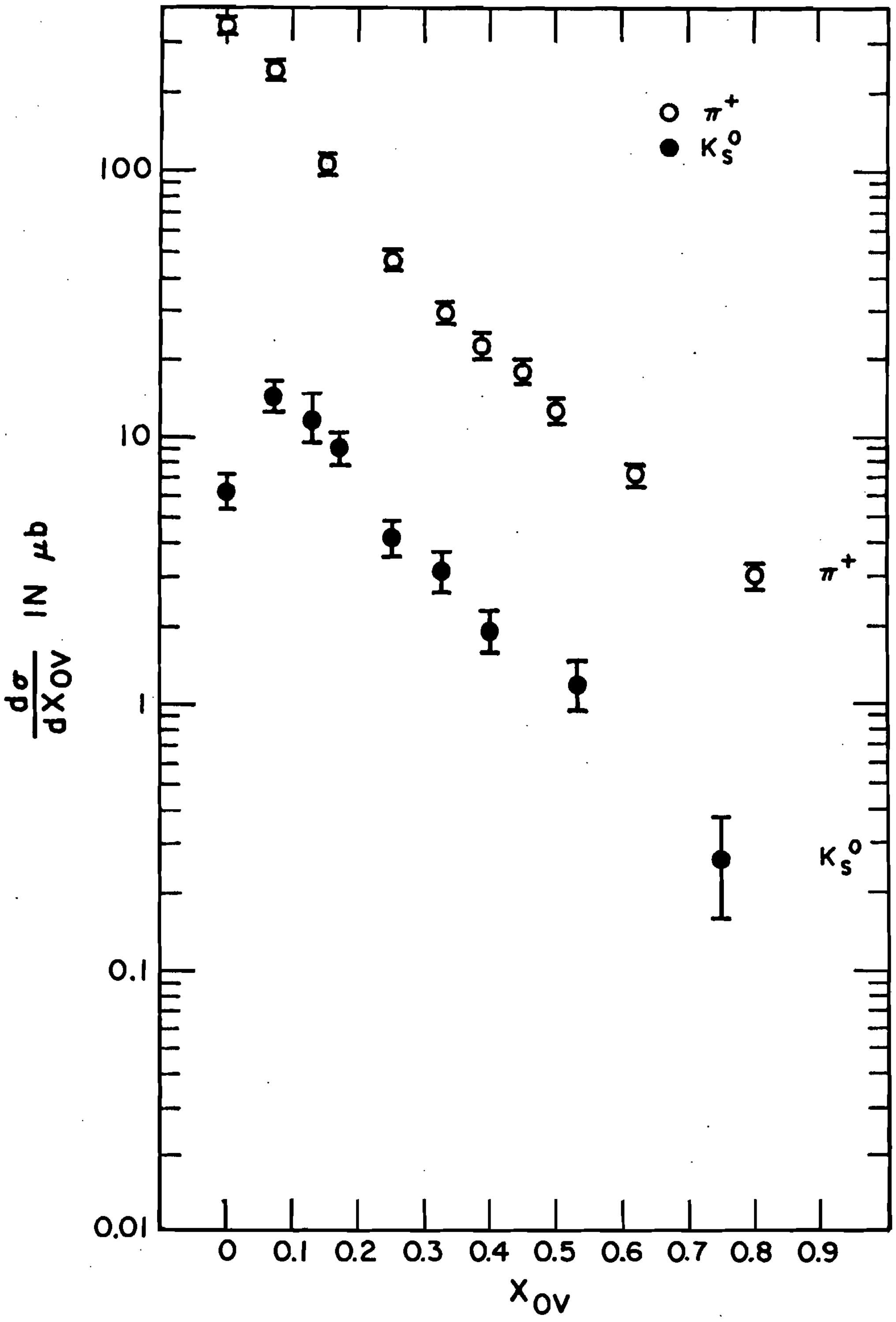

Figure 8.8 The differential cross section of the neutral kaons and pions as a function of the Feynman X in the overall centre of mass.

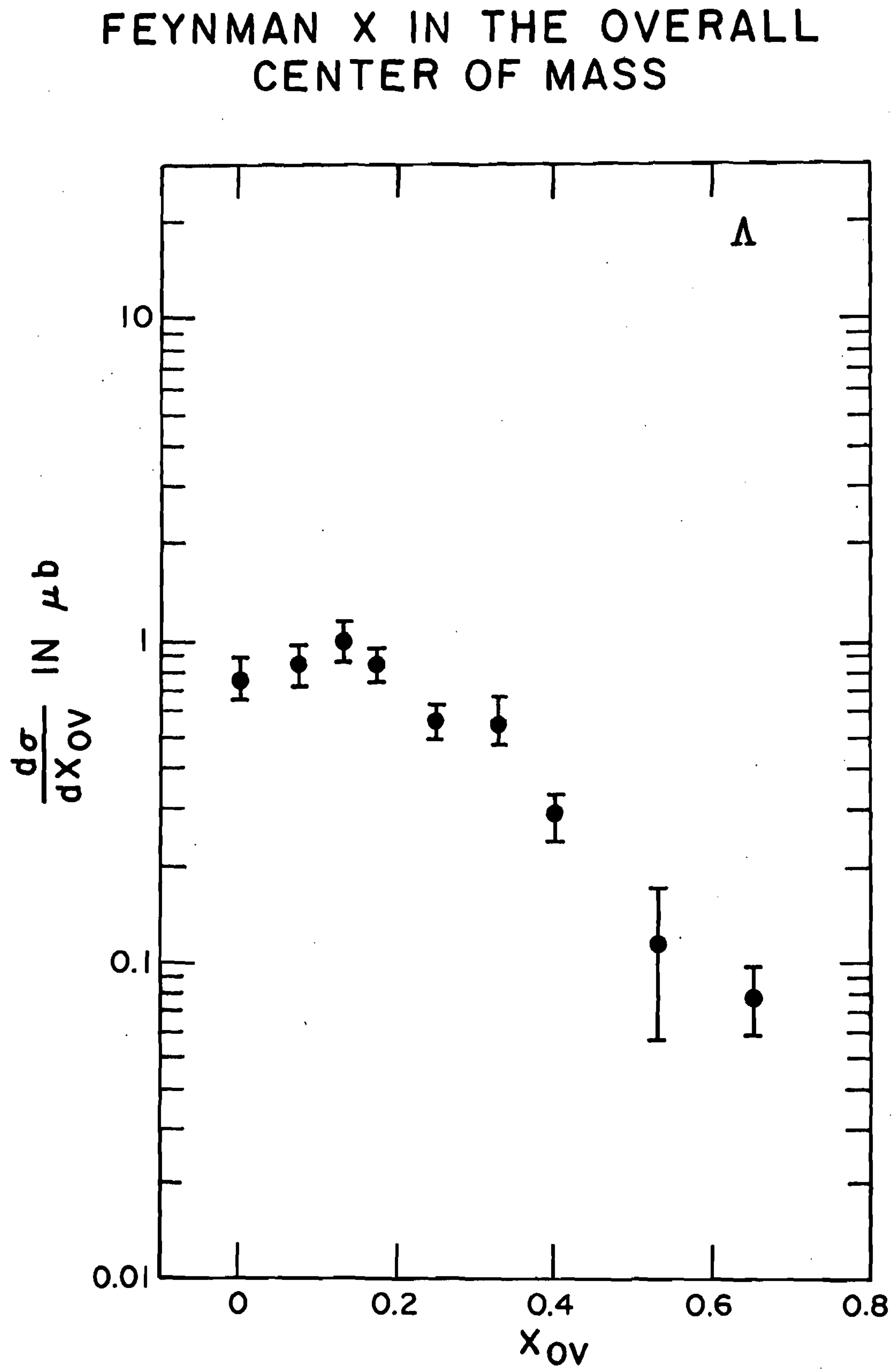
FEYNMAN X IN THE OVERALL CENTER OF MASS

Figure 8.9 The differential cross section of lambdas as a function of the Feynman X in the overall centre of mass.

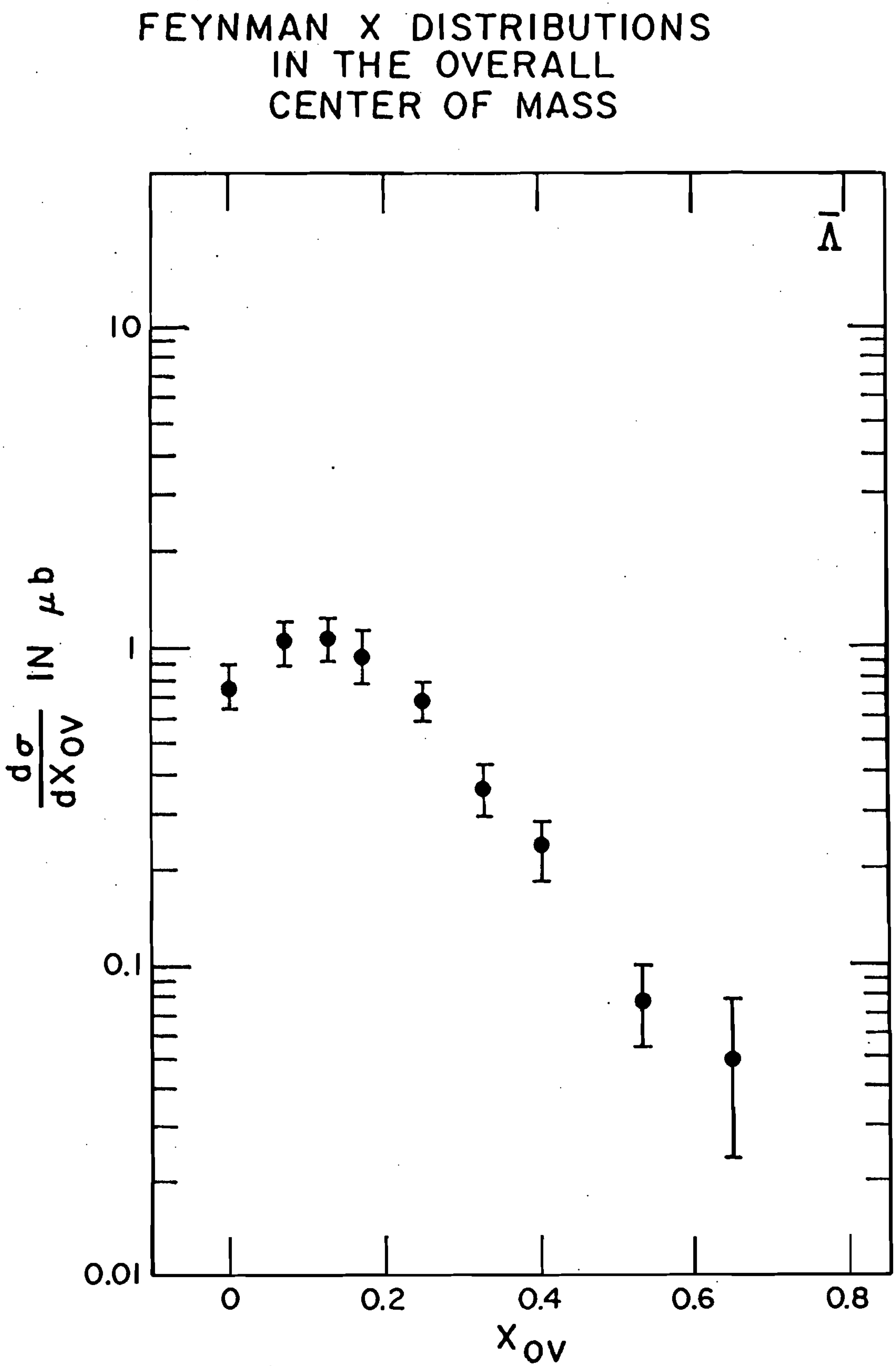

Figure 8.10 The differential cross section of antilambdas as a function of the Feynman X in the overall centre of mass

FEYNMAN X IN OVERALL CENTER OF MASS

$$X_{OV}\frac{d\sigma}{dX_{OV}} \propto A(1-X_{OV})^{D}$$

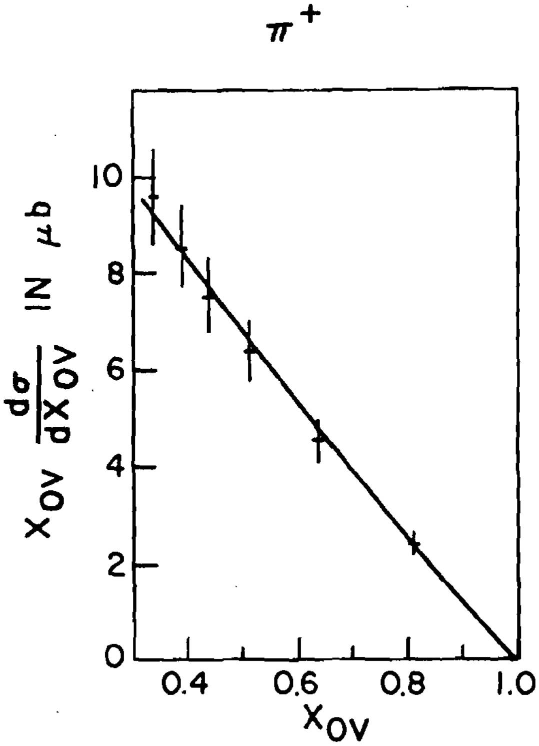

Figure 8.11

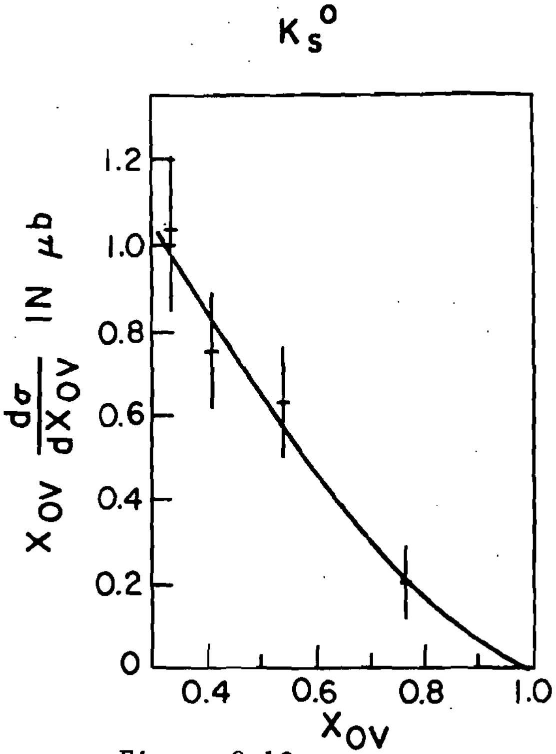

Figure 8.12

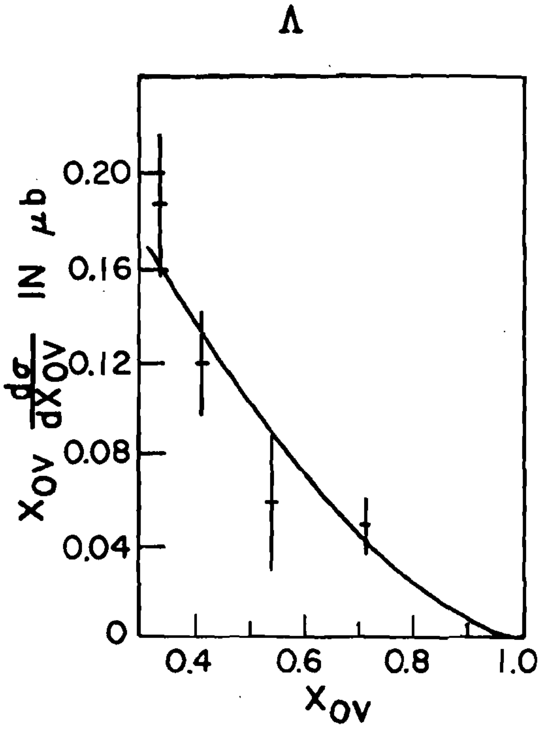

Figure 8.13

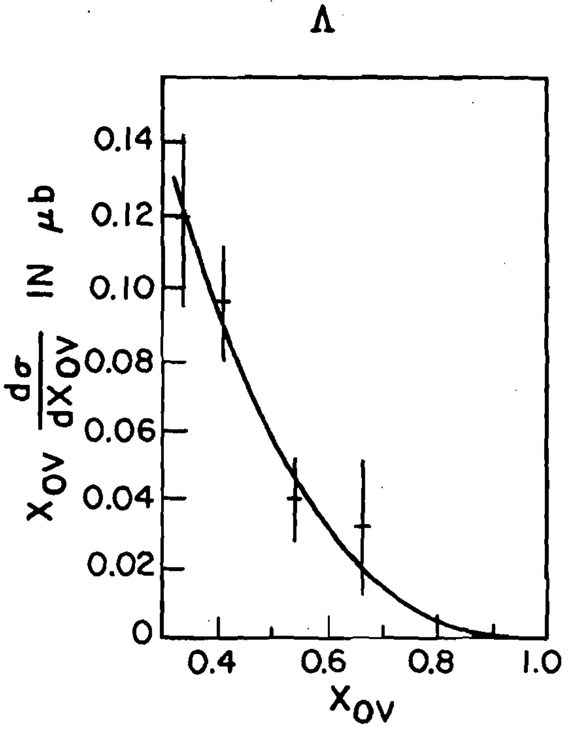

Figure 8.14

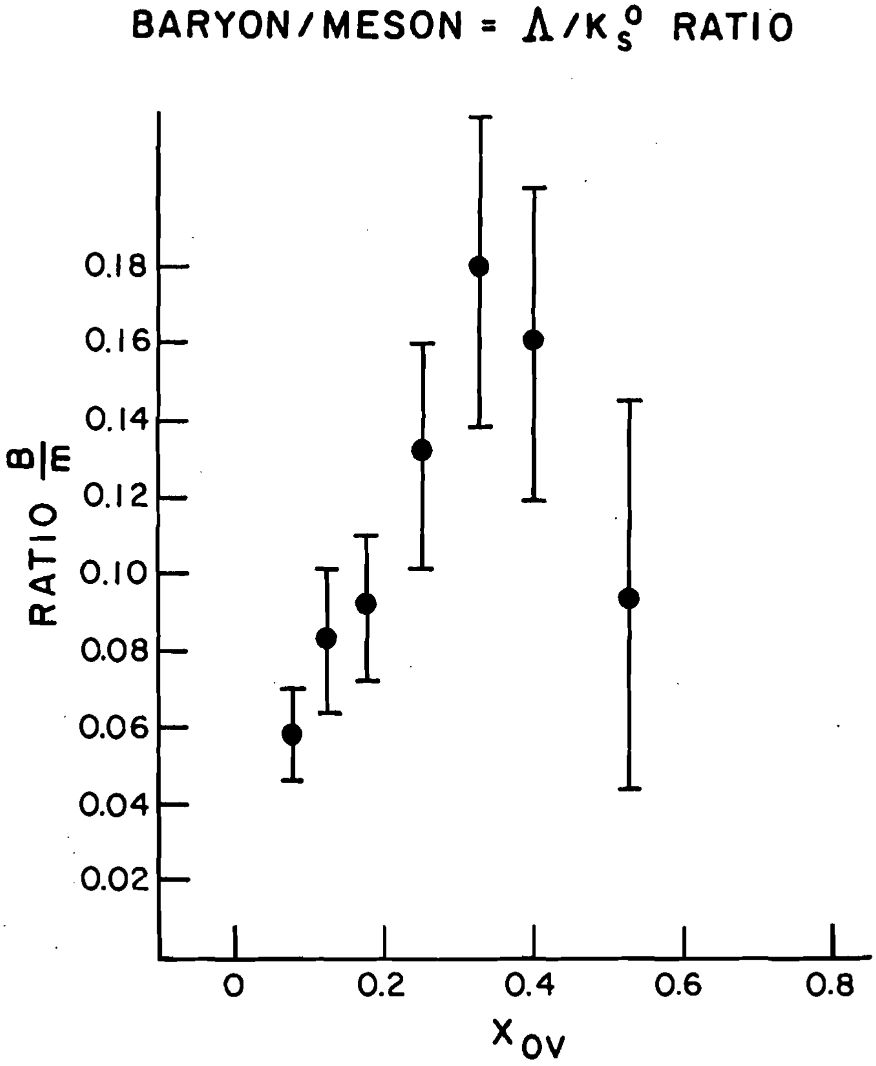

Figure 8.15 The baryon to meson ration as a function of the Feynman X in the overall centre of mass.

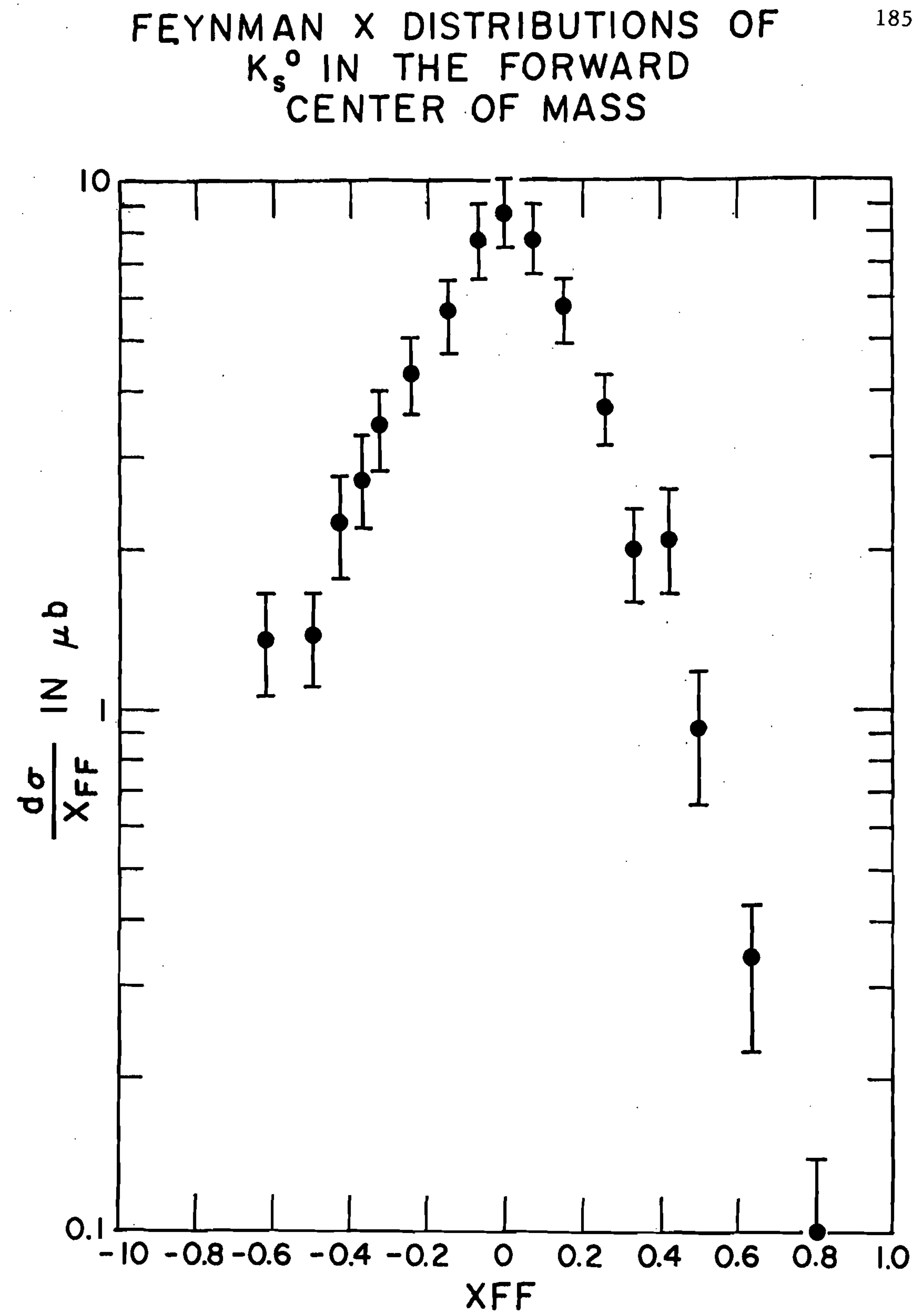

Figure 8.16 The differential cross section of neutral kaons as a function of the Feynman X in the forward centre of mass.

FEYNMAN X DISTRIBUTIONS OF Λ IN THE FORWARD CENTER OF MASS

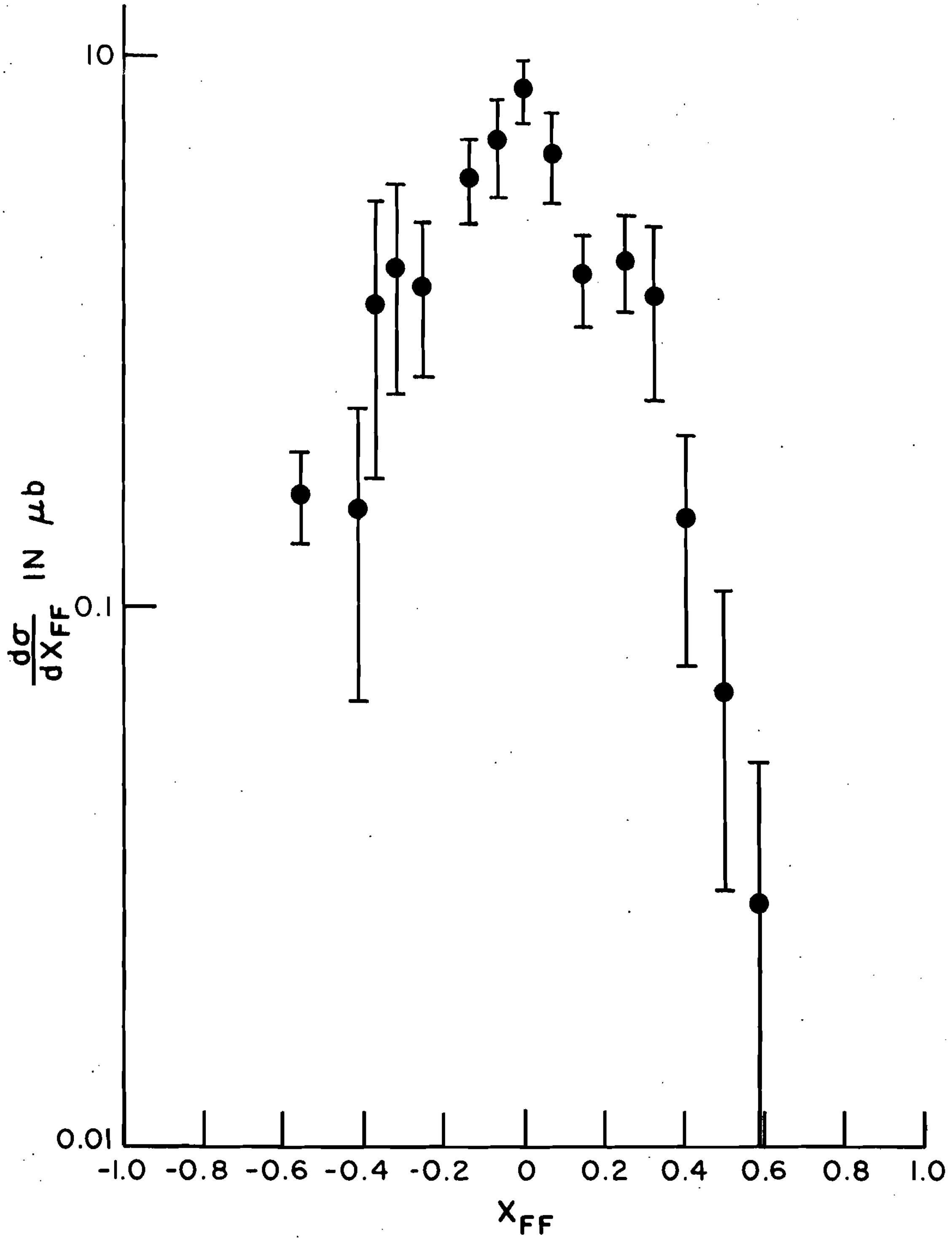

Figure 8.17 The differential cross section of lambdas as a function of the Feynman X in the forward centre of mass,

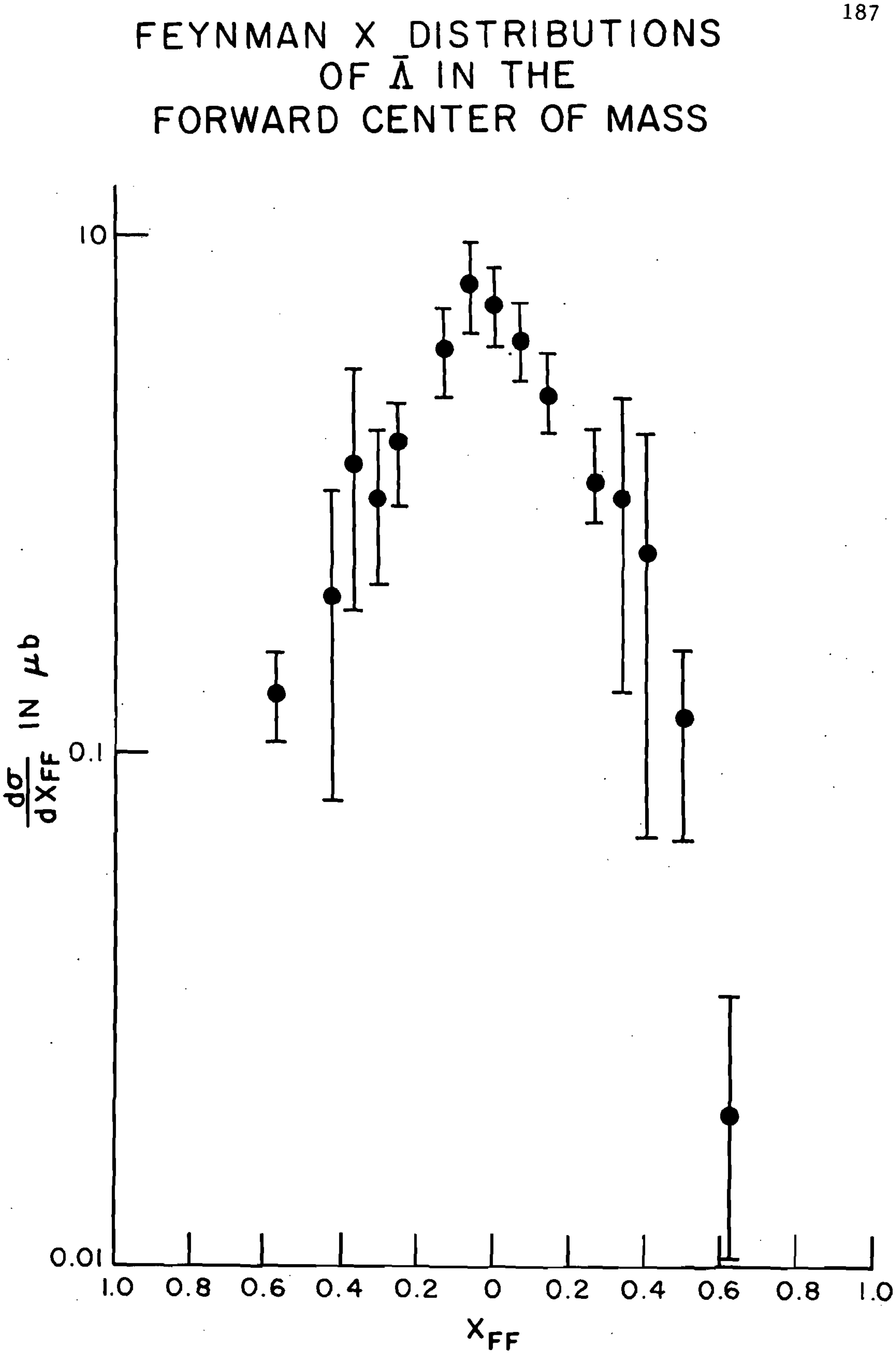

Figure 8.18 The differential cross section of antilambdas as a function of the Feynman X in the forward centre of mass.

FEYNMAN X IN THE FORWARD CENTER OF MASS

$$X_{FF}\frac{d\sigma}{dX_{FF}} \propto A(1-X_{FF})^{D}$$

K_s^0

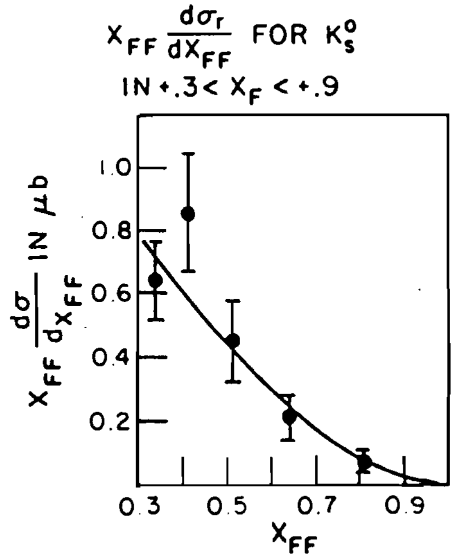

Figure 8.19

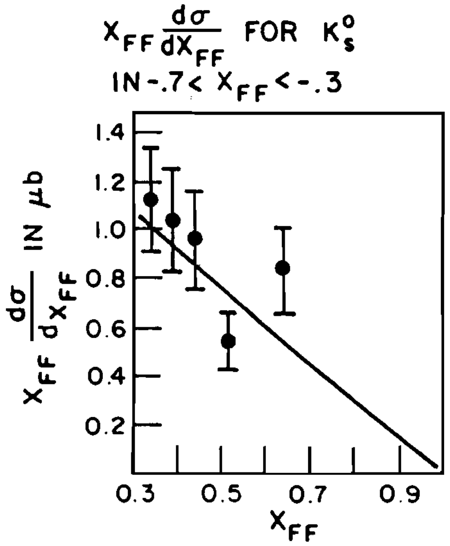

Figure 8.20

FEYNMAN X IN THE FORWARD CENTER OF MASS

$$X_{FF}\frac{d\sigma}{dX_{FF}} \propto A(1-X_{FF})^{D}$$

$\Lambda + \bar{\Lambda}$

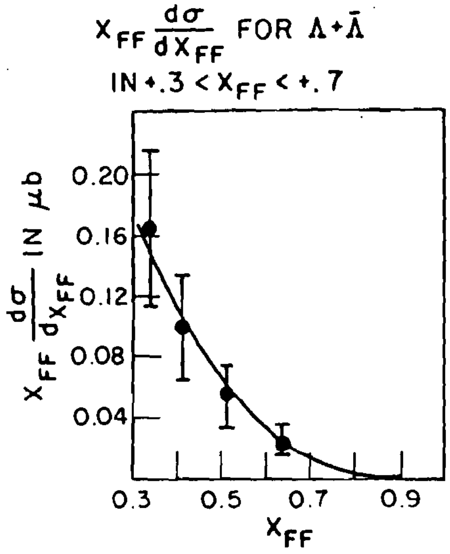

Figure 8.21

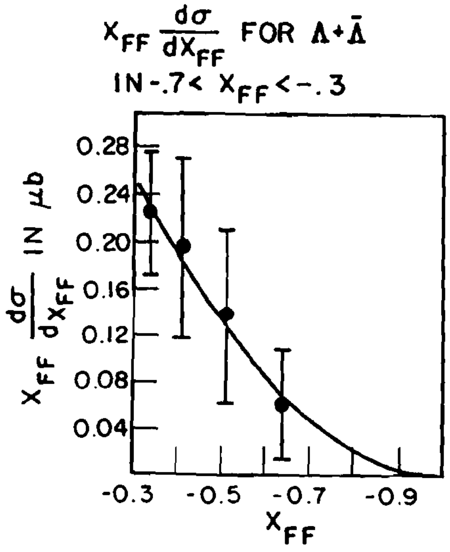

Figure 8.22

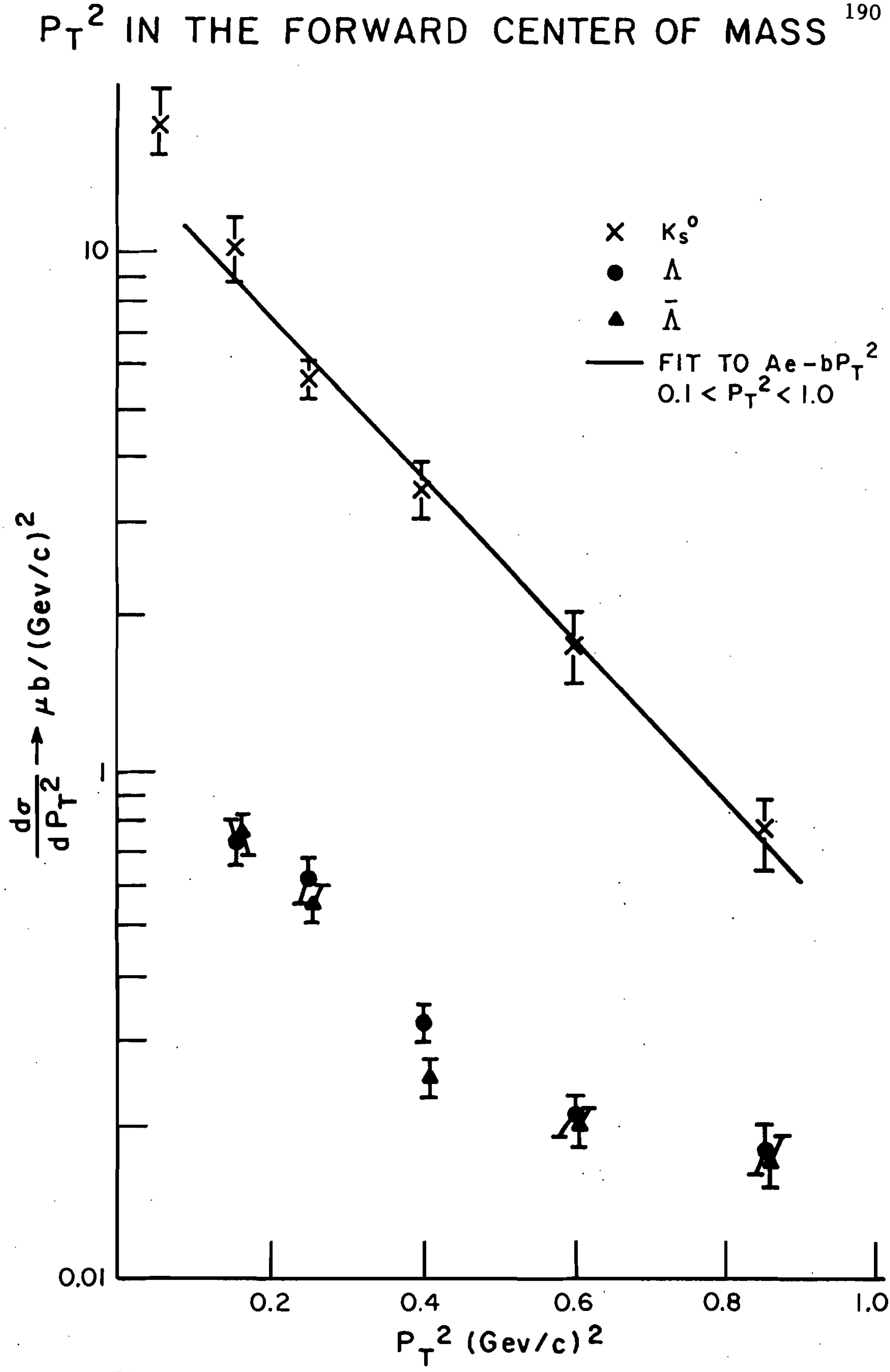

Figure 8.23 The differential cross section as a function of P_t^2.

SLOPE OF $Ae^{-bP_T^2}$ IN M_x BINS IN FORWARD CENTER OF MASS

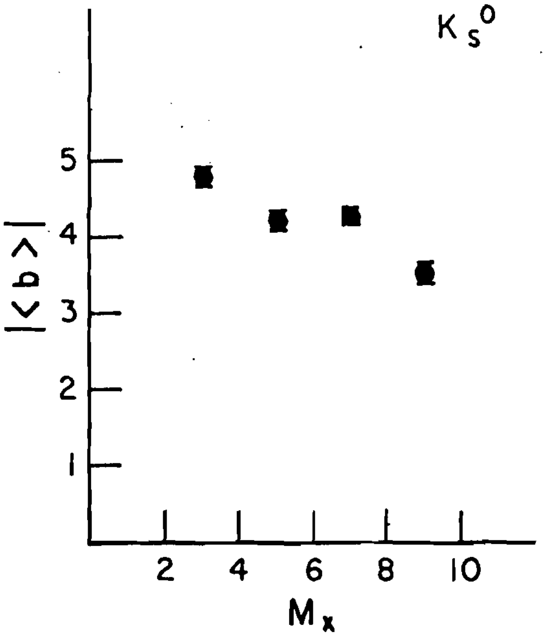

M_x	$b + \Delta b$
2 - 4	4.8 ± 0.2
8 - 6	4.3 ± 0.2
6 - 8	4.3 ± 0.2
8 - 10	3.5 ± 0.2

Figure 8.24 The slope of P_t^2 as a function of M_x for neutral kaons.

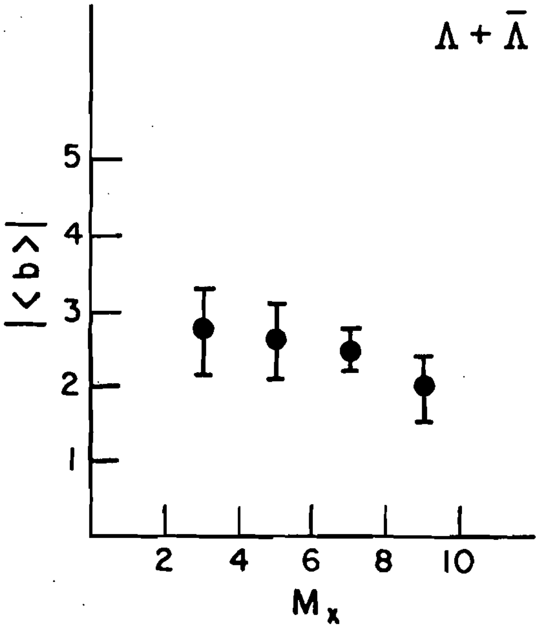

M_x	$b + \Delta b$
2 - 4	2.8 ± 0.5
8 - 6	2.7 ± 0.5
6 - 8	2.4 ± 0.3
8 - 10	2.0 ± 0.4

Figure 8.25 The slope of P_t^2 as a function of M_x for lambdas and antilambdas.

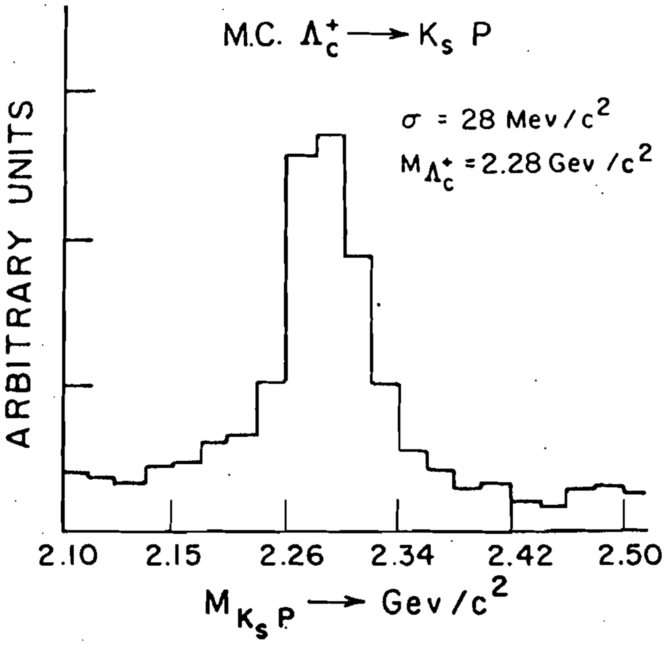

Figure 8.26 The invariant mass of $K_s{}^0$ and a proton for Monte Carlo events.

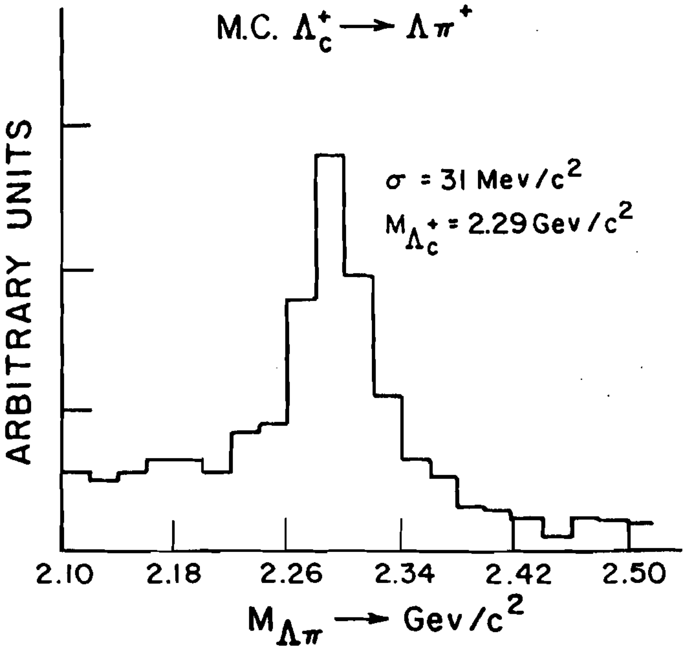

Figure 8.27 The invariant mass of lambdas and pions for Monte Carlo events.

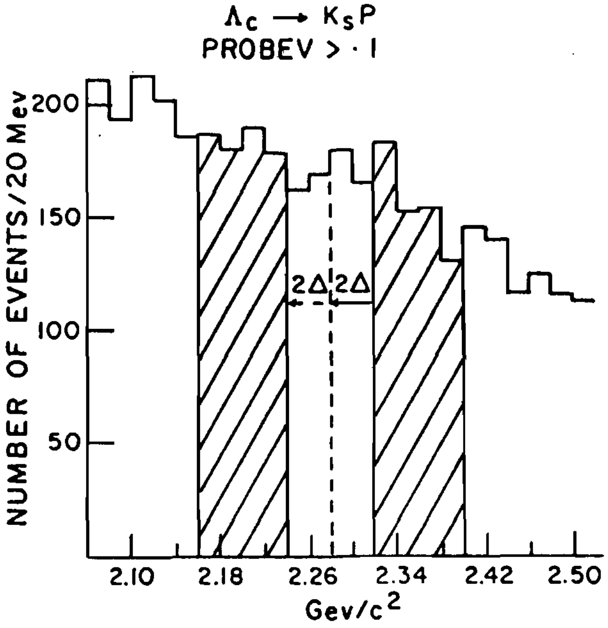

Figure 8.28 The invariant mass of K_s^0 and protons for data events.

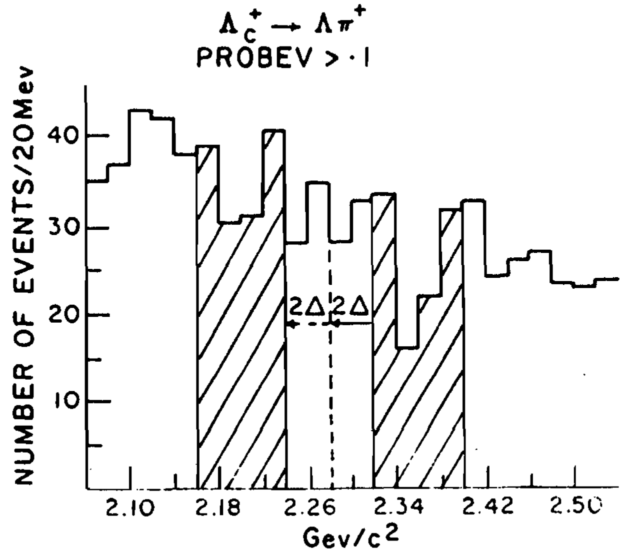

Figure 8.29 The invariant mass of lambdas and pions for data events.